High Precision Tools for Slepton Pair Production Processes at Hadron Colliders

Dissertation
zur Erlangung des Grades

"Doktor
der Naturwissenschaften"

am Fachbereich Physik, Mathematik und Informatik
der Johannes Gutenberg-Universität in Mainz

Stephan Christoph Thier

geb. in Bochum
Mainz, den 01.12.2014

Zusammenfassung

In dieser Doktorarbeit entwickeln wir Hochpräzisionswerkzeuge für die Simulation der Paarproduktion von Sleptonen in hadronischen Kollisionsprozessen an Teilchenbeschleunigern und verwenden sie für phänomenologische Untersuchungen am LHC. Unser Vorgehen basiert auf der POWHEG Methode für die konsistente Kombination von störungstheoretischen Resultaten in nächstführender Ordnung mit Partonschauern. Wir berechnen die Matrixelemente für die Paarproduktion von Sleptonen sowie für die Produktion eines Sleptonpaares in Assoziation mit einem Jet gemäß störungstheoretischer Methoden der supersymmetrischen Quantenchromodynamik in nächstführender Ordnung. Beide Prozesse implementieren wir anschließend in der POWHEG BOX, einem öffentlich verfügbaren Computerprogramm, das allgemeine Bestandteile des POWHEG Verfahrens enthält.

Wir untersuchen phänomenologische Konsequenzen unserer Berechnungen in mehreren supersymmetrischen Massenkonfigurationen unter Beachtung experimenteller Ausschlussgrenzen und treffen präzise Vorhersagen für Sleptonsignaturen am LHC. Eine genaue Beschreibung harter Jets erfolgt durch die Berücksichtigung von QCD-Emissionen in den partonischen Matrixelementen. Partonschauer und Sleptonzerfälle simulieren wir in vollständig exklusiven Kollisionsereignissen durch die Anbindung unserer Implementierungen an das Monte-Carlo-Programm PYTHIA. Auf Grundlage der kinematischen Information aller beobachtbaren Teilchen untersuchen wir die Leistungsfähigkeit speziell entwickelter Variablen in der Trennung des Signals von Untergrundprozessen und die Chancen spezifischer Suchstrategien für Sleptonen in experimentell schwer zugänglichen supersymmetrischen Massenkonfigurationen.

Abstract

In this thesis, we develop high precision tools for the simulation of slepton pair production processes at hadron colliders and apply them to phenomenological studies at the LHC. Our approach is based on the POWHEG method for the matching of next-to-leading order results in perturbation theory to parton showers. We calculate matrix elements for slepton pair production and for the production of a slepton pair in association with a jet perturbatively at next-to-leading order in supersymmetric quantum chromodynamics. Both processes are subsequently implemented in the POWHEG BOX, a publicly available software tool that contains general parts of the POWHEG matching scheme.

We investigate phenomenological consequences of our calculations in several setups that respect experimental exclusion limits for supersymmetric particles and provide precise predictions for slepton signatures at the LHC. The inclusion of QCD emissions in the partonic matrix elements allows for an accurate description of hard jets. Interfacing our codes to the multi-purpose Monte-Carlo event generator PYTHIA, we simulate parton showers and slepton decays in fully exclusive events. Advanced kinematical variables and specific search strategies are examined as means for slepton discovery in experimentally challenging setups.

Tag der mündlichen Doktorprüfung: 20.01.2015

Contents

Chapter 1

Introduction

Particle Physics explores the structures and building blocks of physical objects at length scales smaller than atomic nuclei. Based on common mathematical principles, a theory known as Standard Model was developed for the three fundamental interactions that govern subatomic processes. It has been repeatedly tested and confirmed by experiments at particle colliders. However, there are strong arguments, both theoretical and observational, for physics beyond the Standard Model. Theoretical extensions of the Standard Model are often based on specific symmetry principles like supersymmetry, which introduces partner particles for all particles that have been observed so far. The search for these partner particles has been and still is one of the major challenges for recent experiments.

The aim of this thesis is the development of precise tools for the simulated pair production of supersymmetric scalar leptons in particle collisions and their application to phenomenological analyses. Our approach combines two techniques of perturbative quantum chromodynamics. Fixed-order matrix elements for the hard interaction that produces the scalar leptons are matched to parton showers. We calculate the matrix elements for the pair production of scalar leptons and for the production of a scalar lepton pair in association with a jet in hadronic collisions at next-to-leading order (NLO) in supersymmetric quantum chromodynamics. For both of these processes, we perform a matching to parton showers, generate programs that use these theoretical results for the simulation of particle collisions, and apply these programs to obtain predictions for reactions at the Large Hadron Collider. We discuss the differences between both codes and highlight the advantages of the inclusion of additional jets in the fixed-order matrix element.

We begin the thesis with a description of the Standard Model and supersymmetry in this chapter. Methods and tools for the simulation of particle production in hadronic collisions are reviewed in chapter 2. Chapter 3 summarizes literature results for scalar lepton pair production and lists the subprocesses that need to be considered in our approach. Technical details of our calculations are discussed in chapter 4. The implementations of the two processes under consideration as computer codes are described in chapter 5. In chapter 6, we present results of our new tools for setups that take current experimental exclusion limits for supersymmetric particles into account and compare them to important background processes. The final chapter 7 summarizes the thesis. Details of our notation, definitions of kinematic variables, and lists of integral decompositions are given in the appendix.

1.1 Standard Model of Particle Physics

1.1.1 Fields and Interactions

The Standard Model of Particle Physics (SM) [47, 115, 199, 222, 198, 116, 157] is a consistent and self-contained theory that describes the most fundamental quantum fields in our universe which have been observed so far. It is based on the symmetry principles of Poincaré invariance for space-time transformations and of local gauge invariance, realized in the color symmetry group $\mathrm{SU}(3)_C$, the weak isospin group of left-handed particles $\mathrm{SU}(2)_L$, and the weak hypercharge group $\mathrm{U}(1)_Y$.

All SM particle fields transform according to representations of the gauge groups. Fields in the adjoint representation of $\mathrm{SU}(N)$ have N^2-1 components, fields in the fundamental or the antifundamental representation have N components, and fields in the trivial representation consist of a single component. The corresponding representations of the SM fields are listed in Tab. 1.1. Fermions are accompanied by antiparticles with opposite charges. In addition, fermions come in three generations which differ only in their masses.

symbol	spin	$\mathrm{SU}(3)_C$	$\mathrm{SU}(2)_L$
g	1	adjoint	trivial
W	1	trivial	adjoint
B	1	trivial	trivial
L_L	1/2	trivial	fundamental
e_R	1/2	trivial	trivial
Q_L	1/2	fundamental	fundamental
u_R	1/2	fundamental	trivial
d_R	1/2	fundamental	trivial
Φ	0	trivial	fundamental

Table 1.1: Interaction eigenstates of the SM, which consist of several components that transform according to representations of the SM gauge groups. Fermions of the second and third generation and antiparticles are not listed. L_L is the doublet (ν_L, e_L) and $Q_L = (u_L, d_L)$.

Propagation and interactions of particles are determined by the Lagrangian of the Standard Model,

$$\mathcal{L}_{\mathrm{SM}} = \mathcal{L}_{\mathrm{fermion}} + \mathcal{L}_{\mathrm{gauge}} + \mathcal{L}_{\mathrm{Higgs}} + \mathcal{L}_{\mathrm{Yukawa}}. \tag{1.1}$$

The propagation of fermionic fields and their interactions with gauge bosons are described by

$$\mathcal{L}_{\mathrm{fermion}} = i \sum_{f^C} \overline{f^C} \not{D} f^C, \tag{1.2}$$

where the sum runs over all fermionic fields f with chiralities C that are listed in Tab. 1.1. The covariant derivative

$$D_\mu = \partial_\mu + \frac{i}{2} \sum_{\mathcal{G}} g_{\mathcal{G}} \sum_{u=1}^{n_{\mathcal{G}}} (T_{\mathcal{G}})^u (K_{\mathcal{G}})^u{}_\mu \tag{1.3}$$

in the contracted form $\not{D} = \gamma_\mu D^\mu$ connects the $n_{\mathcal{G}}$ gauge fields $K_{\mathcal{G}}$ of all gauge groups $\mathcal{G}$ with couplings constants $g_{\mathcal{G}}$ and $n_{\mathcal{G}}$ generators $T_{\mathcal{G}}$ to the fermions of the Standard Model.

Coupling constants determine the strength of all gauge interactions. We denote them according to the gauge groups as g_C for $\mathrm{SU}(3)_C$, which is also referred to as strong coupling g_s, g_L for $\mathrm{SU}(2)_L$, and g_Y for $\mathrm{U}(1)_Y$. Gauge invariance requires the coupling constants to be identical in all interactions that are mediated by a specific gauge group. It is often convenient to express couplings in terms of $\alpha_\mathcal{G} = g_\mathcal{G}^2/(4\pi)$ in analogy to the fine-structure constant.

Kinetic terms and self-interaction terms of the three gauge fields g, W, B are summarized in $\mathcal{L}_\text{gauge}$. The non-abelian structure of $\mathrm{SU}(3)_C$ and $\mathrm{SU}(2)_L$ leads to self-interaction terms for the corresponding vector fields G and W, whereas there is no such interaction for the gauge field B. The vector field G in the adjoint representation of $\mathrm{SU}(3)_C$ has 8 components G^a, the vector field W in the adjoint representation of $\mathrm{SU}(2)_L$ consists of 3 components W^i. For each of the $n_\mathcal{G}$ components of these fields, a field strength tensor $(F_\mathcal{G})^u{}_{\mu\nu}$ is defined as

$$G^a{}_{\mu\nu} = \partial_\mu G^a{}_\nu - \partial_\nu G^a{}_\mu - g_C f^{abc} G^b{}_\mu G^c{}_\nu, \tag{1.4}$$

$$W^i{}_{\mu\nu} = \partial_\mu W^i{}_\nu - \partial_\nu W^i{}_\mu - g_L \varepsilon^{ijk} W^j{}_\mu W^k{}_\nu, \tag{1.5}$$

$$B_{\mu\nu} = \partial_\mu B_\nu - \partial_\nu B_\mu. \tag{1.6}$$

ε^{ijk} are the structure constants of $\mathrm{SU}(2)_L$ and f^{abc} the ones of $\mathrm{SU}(3)_C$. The sum over Lorentz-invariant contractions of these field strength tensors makes up the gauge part of the Standard Model Lagrangian

$$\mathcal{L}_\text{gauge} = -\frac{1}{4} \sum_\mathcal{G} \sum_{u=1}^{n_\mathcal{G}} (F_\mathcal{G})^{u\mu\nu} (F_\mathcal{G})^u{}_{\mu\nu}. \tag{1.7}$$

The Higgs part of the SM Lagrangian is given by

$$\mathcal{L}_\text{Higgs} = (D^\mu \Phi)^\dagger (D_\mu \Phi) - V(\Phi) \tag{1.8}$$

with the Higgs potential

$$V(\Phi) = -\mu^2 |\Phi|^2 + \lambda |\Phi|^4. \tag{1.9}$$

Positive values of μ^2 and λ lead to a non-vanishing vacuum expectation value (VEV) $|\langle\Phi\rangle| \neq 0$ of the complex Higgs doublet field Φ. The fixed non-zero vacuum expectation value spontaneously breaks the weak symmetry groups generating mass terms for the vector bosons via the Brout-Englert-Higgs mechanism [140, 139, 141, 94] without violating gauge invariance. Mass terms generated for the W and B fields from the coupling to $|\langle\Phi\rangle|$ through the covariant derivative in $\mathcal{L}_\text{Higgs}$ lead to three massive states

$$W^+ = \frac{1}{\sqrt{2}} \left(W^1 - iW^2\right), \quad W^- = \frac{1}{\sqrt{2}} \left(W^1 + iW^2\right), \tag{1.10}$$

$$Z = \cos\theta_W W^3 - \sin\theta_W B, \tag{1.11}$$

and one massless photon state

$$\gamma = \sin\theta_W W^3 + \cos\theta_W B \tag{1.12}$$

due to the protection by the remaining electromagnetic symmetry group $\mathrm{U}(1)_\mathrm{EM}$. The mixing of the electrically neutral fields is given by the Weinberg angle θ_W, which fulfills

$$\sin\theta_W = \frac{g_Y}{\sqrt{g_Y^2 + g_L^2}}. \tag{1.13}$$

The strength of electromagnetic interactions is determined by

$$e = \cos\theta_W g_Y, \tag{1.14}$$

the absolute value of the electron charge. We denote the associated coupling factor $\alpha_{\mathrm{EM}} = e^2/(4\pi)$ as α in the following.

During the generation of masses for the vector bosons W^+, W^-, and Z, three degrees of freedom of the complex scalar field Φ are absorbed. One remaining degree of freedom from Φ forms the real scalar Higgs field h and leads to the emergence of an associated boson.

In the Yukawa part of the SM Lagrangian, the complex scalar Higgs field $\Phi = (\phi^+, \phi^0)$ and its charge conjugate $\Phi^c = (\phi^{0*}, -\phi^-)$ couple to the fermions according to

$$\mathcal{L}_{\mathrm{Yukawa}} = -\overline{L}_L Y_e e_R \Phi - \overline{Q}_L Y_u u_R \Phi^c - \overline{Q}_L Y_d d_R \Phi \tag{1.15}$$

for one generation of fermions only. Since fermions come in three generations, the actual Yukawa couplings Y_e, Y_u, Y_d are unitary matrices that connect all members of the respective generations. Couplings to the vacuum expectation value of Φ generate mass terms for fermions. Mass values and corresponding eigenstates can be found by diagonalization of the Yukawa matrices. These states correspond to propagating particles, as long as these can be considered as free.

The discrete transformations charge conjugation (C), parity of spatial inversion (P), and time reversal (T) are not symmetries of the full Standard Model. While all Standard Model interactions respect the combination CPT of all three transformations due to fundamental properties of Poincaré invariant quantum field theories, weak interactions violate C, P, and the combination CP.

1.1.2 Success and Extensions

Many discoveries were predicted by the SM and many high-precision experiments agree with the SM to an incredible amount of accuracy. To mention only a few of these successes:

- A Higgs particle has been discovered [6, 69] by the ATLAS and CMS experiments at the Large Hadron Collider (LHC). It lies in the mass range that was deduced from electroweak precision measurements [1] and its properties agree very well with the expectations for the Standard Model Higgs boson [7, 70].

- Particle production rates in the previously unexplored energy range, which is accessible to LHC experiments, are in excellent agreement with theoretical predictions, as illustrated in Fig. 1.1.

- Lattice quantum chromodynamics (QCD) calculations [162] provide a very precise description of the hadron spectrum.

- Theoretical calculations [27] and experimental measurements [137] of the electron magnetic moment anomaly $a_e = (g_e - 2)/2$ agree with a relative deviation smaller than 10^{-8}.

Despite the success of the SM, it does not provide a complete description of our universe. Gravity is not part of the Standard Model and neutrinos occur in the SM only as massless left-handed particles. While right-handed neutrinos, that allow for the observed

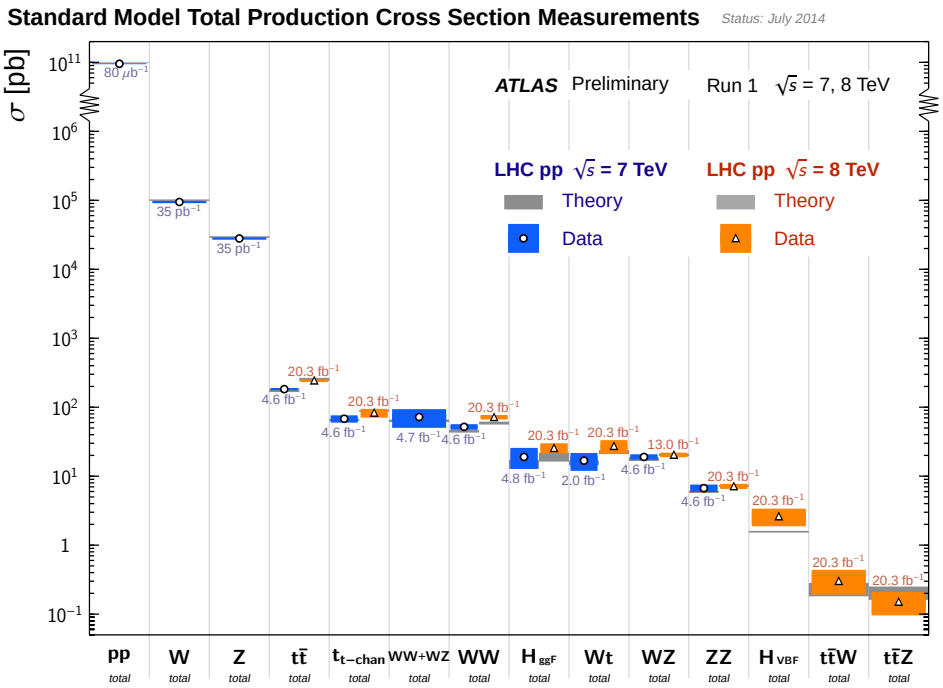

Figure 1.1: Comparison of Standard Model predictions for particle production cross sections and measurements by the ATLAS experiment. Figure taken from [3].

neutrino oscillations, can be added in a minimal extension of the Standard Model, gravity and other astrophysical clues like dark matter and dark energy emphasize the need for a profound extension. Assuming that the SM is only part of a more complete theory, we may regard the SM as an effective field theory (EFT) with a limited range of validity. Experimental tests of the SM reach several 10^3 giga electronvolts (GeV) at present colliders. No evidence for physics beyond the Standard Model (BSM) has been found in these collision experiments. Gravity effects are expected to become relevant at the Planck Scale (10^{18} GeV), but BSM physics may lie anywhere in the large unexplored region between this scale and the limits of current observations.

If a cutoff scale Λ is introduced that provides an upper limit for the applicability of the SM, the Higgs boson mass will receive radiative corrections which are proportional to Λ^2 [213]. ATLAS and CMS report mass values for the recently discovered Higgs boson of 126.0 GeV[6] and 125.3 GeV[69] respectively. To arrive at such a small value after the inclusion of large radiative corrections requires a high degree of cancelation between different terms, that is widely considered to be unnatural unless it is the consequence of a specific mechanism or symmetry. The Standard Model does not indicate such a mechanism for the solution of this electroweak hierarchy problem.

Extensions of the Standard Model use different mechanisms to stabilize the electroweak scale. Technicolor models [213, 223, 191] consider the Higgs boson to be composite so that there are no fundamental scalar particles with associated quadratic divergences. In Supersymmetry, the framework we will consider in this thesis, divergences in loop corrections of the Higgs boson propagator from Standard Model particles and their supersymmetric partners cancel.

1.2 Supersymmetry

Supersymmetry (SUSY) [119, 219, 224] relates fermions and bosons via fermionic symmetry generators Q. All considerations in this thesis are restricted to global supersymmetry with constant symmetry generators. Local supersymmetry with generators $Q(x)$ that depend on the position in space-time is used for theories which include gravity. For a comprehensive review of general concepts of supersymmetry and of specific supersymmetric models, we refer to [185].

Supersymmetry generators are in the simplest case two component Weyl spinors Q_α with $\alpha = 1, 2$, and the corresponding hermitian conjugate spinors $Q^\dagger_{\dot\alpha}$, that fulfill the following algebraic commutation and anticommutation relations:

$$\{Q_\alpha, Q^\dagger_{\dot\alpha}\} = -2\sigma^\mu_{\alpha\dot\alpha} P_\mu, \tag{1.16}$$

$$\{Q_\alpha, Q_\beta\} = 0, \tag{1.17}$$

$$\{Q^\dagger_{\dot\alpha}, Q^\dagger_{\dot\beta}\} = 0, \tag{1.18}$$

$$[Q_\alpha, P^\mu] = 0, \tag{1.19}$$

$$[Q^\dagger_{\dot\alpha}, P^\mu] = 0. \tag{1.20}$$

P^μ is the four-momentum operator that generates translations in space-time.

The number N of supersymmetry generating pairs of operators $Q, Q^\dagger$ can be larger than one. It was shown [169, 101] that theories with $N = 4$ have the remarkable property of being finite. However, theories with $N > 1$ do not allow for chiral fermions [172] in four dimensions, hence they are not directly applicable for the description of the experimentally observed particle spectrum.

Supersymmetry connects internal particle symmetries to the Poincaré symmetry of space-time in special relativity. Bosonic symmetry generators cannot extend Poincaré symmetry in a non-trivial way, as was shown by Coleman and Mandula [73]. They found that, under reasonable assumptions, internal symmetry groups can be combined with the Poincaré symmetry group only in the form of direct products. Haag, Lopuszanski, and Sohnius [128] showed that fermionic supersymmetry generators provide the only opportunity of a real extension of the Poincaré group.

Particles that are related by supersymmetry have the same quantum numbers (except for the spin difference of 1/2), the same masses and the same couplings. These predictions are not only distinctive, but also in conflict with observation. Since no partners of the SM particles with these properties have been found in experiments, SUSY cannot be an exact symmetry. If supersymmetry is present in nature, it must be broken. This breaking is called soft [112], if it preserves one of the key features of supersymmetric theories, namely the cancelation of quadratic divergences for scalar masses. SUSY particles are expected to receive large masses by such a breaking mechanism, so that they all lie above a characteristic supersymmetry scale.

The successful unified description of electroweak interactions makes the idea of one underlying symmetry group, which combines all known interactions, look very appealing. While they have very different strengths at energy scales that are currently accessible to experiments, gauge couplings evolve with the energy and they may meet at a high unification scale. For the Standard Model without additional particles, gauge coupling unification at a single scale has been excluded at the level of more than seven standard deviations already in 1991 [25] based on data of the DELPHI experiment at LEP. Additional particles in supersymmetry with masses near the supersymmetric scale modify the running

of the couplings above this threshold. In this way, supersymmetry makes the unification of all known gauge couplings around the scale of 10^{16} GeV possible [91, 113, 25, 163]. Conversely, the assumption of gauge coupling unification in a specific supersymmetric model allows to estimate the supersymmetric scale. Adding only the minimal amount of supersymmetric particles to the Standard Model, one can deduce from gauge coupling unification a supersymmetric scale of the order 1 TeV.

1.2.1 R-parity

R-parity [97] is a discrete symmetry, which is often assumed in supersymmetric models and has important phenomenological consequences. A particle with spin S, baryon number B, and lepton number L, has an R-parity given by

$$R = (-1)^{2S+3(B-L)} . \tag{1.21}$$

Quarks have the baryon number 1/3, leptons the lepton number 1, for all other SM particles these numbers vanish. In the Standard Model, B and L are conserved separately, but not as a consequence of a fundamental symmetry, rather accidentally due to a lack of renormalizable terms that would violate B or L. It is unlikely that B or L should be regarded as fundamental symmetries, since they are violated by non-perturbative effects [214], although the magnitude of this violation is tiny at currently available energies. A superpartner of an SM fermion carries the same baryon and lepton numbers as its SM counterpart [98, 100].

All Standard Model particles are assigned the value $R = +1$ by Eq. (1.21), their superpartners have $R = -1$. With conserved R-parity, collisions of Standard Model particles can only produce pairs of supersymmetric particles and the lightest supersymmetric particle (LSP) cannot decay, which makes it an excellent candidate for Dark Matter [187, 118] if it interacts only weakly. If R-parity violating interactions are included in supersymmetric models, protons should be able to decay with a lifetime of less than one second for squark masses around 1TeV and generic couplings of order unity [172]. However, proton decay has never been observed and dedicated experiments set lower bounds on the proton lifetime that exceed the age of the universe by many orders of magnitude.

Discrete R-parity can be derived as remnant of a continuous U(1) R-invariance that is broken by the gravitino mass when gravity is included [99]. Continuous U(1) R-invariance cannot be an exact symmetry, since it would lead to massless gluinos [97, 96], even after SUSY breaking, which is in conflict with experimental results.

1.2.2 MSSM

The Minimal Supersymmetric Standard Model (MSSM) is an extension of the Standard Model that introduces superpartners for all SM particles [130] and extends the Higgs sector to two complex doublets, (H_u^+, H_u^0) and (H_d^0, H_d^-), which generate mass for quarks of 'up'-type and 'down'-type respectively [142, 143, 125]. It is minimal in the sense that at least all the additional particles introduced by the MSSM are required in a supersymmetric theory that comprises the Standard Model. The MSSM includes all supersymmetric interactions that are renormalizable, consistent with SM gauge symmetries and conserve R-parity, as well as completely general soft SUSY breaking terms.

Supersymmetric particles are labeled by names which are slight modifications of the ones belonging to their Standard Model partners. The names of scalar supersymmetric

spin 0	spin $\frac{1}{2}$	spin 1	line style
	gluino $\tilde{g}$	gluon g	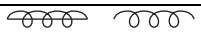
	wino $\tilde{W}^{-,0,+}$	$W^{-,0,+}$	
	bino $\tilde{B}$	B	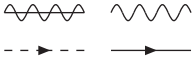
charged slepton $\tilde{\ell}_{L,R}$	charged lepton $\ell_{L,R}$		
sneutrino $\tilde{\nu}_L$	neutrino ν_L		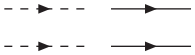
'up'-type squark $\tilde{u}_{L,R}$	'up'-type quark $u_{L,R}$		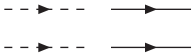
'down'-type squark $\tilde{d}_{L,R}$	'down'-type quark $d_{L,R}$		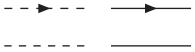
Higgs $H_u^+, H_u^0, H_d^0, H_d^-$	Higgsino $\tilde{H}_u^+, \tilde{H}_u^0, \tilde{H}_d^0, \tilde{H}_d^-$		

Table 1.2: Interaction eigenstates of the MSSM and corresponding line styles.

particles start with an 's-' in front of the corresponding Standard Model particle name, supersymmetric fermions have '-ino' attached behind the name of their partner particle. Symbols for supersymmetric particles are discriminated by a tilde from the corresponding Standard Model particles. Table 1.2 contains all particles of the MSSM in the form of interaction eigenstates and the line styles that we use to depict these particles in Feynman diagrams.

Representations and charges of the MSSM fields under the common gauge groups of the SM and the MSSM are listed in Tab. 1.3. In this table, representations of SU(N) are labeled by their dimension. Particles in the antifundamental representation are highlighted by a bar. Only the left-handed part of chiral multiplets is included in this table.

Like in the Standard Model, three degrees of freedom are taken from the Higgs sector in electroweak symmetry breaking to generate masses for the three W^+, W^-, Z bosons. Since the two complex Higgs doublets of the MSSM have eight real degrees of freedom, five of them remain after symmetry breaking to form physical Higgs fields. They generate two neutral CP-even scalars h^0, H^0, one neutral CP-odd scalar A^0 and two charged Higgs fields H^+, H^-. The ratio between the VEVs of both Higgs fields is usually denoted as $\tan\beta = v_u/v_d$.

spin 0	spin 1/2	spin 1	SU(3)$_C$	SU(2)$_L$	U(1)$_Y$
	$\tilde{g}$	g	**8**	**1**	0
	$\tilde{W}$	W	**1**	**3**	0
	$\tilde{B}$	B	**1**	**1**	0
$\tilde{L}_L$	L_L		**1**	**2**	-1/2
$\tilde{e}_R^*$	$e_R^\dagger$		**1**	**1**	1
$\tilde{Q}_L$	Q_L		**3**	**2**	1/6
$\tilde{u}_R^*$	$u_R^\dagger$		$\overline{\mathbf{3}}$	**1**	-2/3
$\tilde{d}_R^*$	$d_R^\dagger$		$\overline{\mathbf{3}}$	**1**	1/3
$H_u^{+,0}$	$\tilde{H}_u^{+,0}$		**1**	**2**	1/2
$H_d^{-,0}$	$\tilde{H}_d^{-,0}$		**1**	**2**	-1/2

Table 1.3: Fundamental fields of the MSSM, their representations and charges under the MSSM gauge groups. For chiral multiplets, left-handed components are listed. Adapted from [172].

Sparticles with the same quantum numbers mix into mass eigenstates that are numbered by increasing mass. Charged winos $\tilde{W}^{-,+}$ and Higgsinos $\tilde{H}_u^+, \tilde{H}_d^-$ form charginos $\tilde{\chi}_{1,2}^{+,-}$, the neutral wino $\tilde{W}^0$, bino $\tilde{B}$, and both neutral Higgsinos $\tilde{H}_u^0, \tilde{H}_d^0$ mix into the propagating neutralinos $\tilde{\chi}_{1,2,3,4}^0$. Small Yukawa couplings lead to negligible mixing in the first two generations of squarks and sleptons, only the third generation exhibits sizeable mixing.

The number of free parameters in the MSSM is significantly larger than in the Standard Model. While there are 19 physical parameters in the SM, this number grows to 124 physical parameters in the MSSM [129] (including the SM parameters). Most of these parameters originate from the completely general soft SUSY breaking terms. It is hardly possible to use all of the free parameters of the general MSSM in phenomenological studies, therefore several restricted versions of the MSSM have been developed.

The constrained MSSM (CMSSM) [151] is based on supergravity-inspired relations that demand one common value for all supersymmetric scalar masses (m_0), all supersymmetric gaugino masses ($m_{\frac{1}{2}}$), and all trilinear SUSY breaking terms (A_0) respectively at the gauge coupling unification scale. Additional free parameters in the Higgs sector are the ratio $\tan\beta = v_u/v_d$ of both Higgs vacuum expectation values and the sign of the parameter μ that couples both Higgs doublet fields. The magnitude of μ is fixed by radiative electroweak symmetry breaking. In the very restricted CMSSM, experimental results can be easily turned into limits for the free parameters. Recent experimental investigations at the LHC have led to high exclusion limits of several hundred GeV for $m_{\frac{1}{2}}$ and several TeV for m_0 [4].

Many parameters in the MSSM correspond to CP violation and flavor changing neutral currents (FCNC), let alone 40 CP-violating phases, which are severely restricted by experimental limits. It is thus possible to eliminate a large part of the MSSM parameters based on experimental observations without imposing strong ad-hoc conditions. This approach is the premise of the phenomenological MSSM (pMSSM) [86]. To avoid conflict with constraints on CP violation, all parameters of the model are assumed to be real. Flavor diagonal sfermion mass matrices and trilinear couplings do not contribute to FCNC. Experimental data from K-meson mixing indicate small splittings between sfermion masses in the first and in the second generation, hence they are set to a common mass value in the pMSSM. Trilinear couplings are proportional to the fermion masses, which makes it possible to take them out for the first and for the second generation in good approximation. In total, the pMSSM contains 19 additional parameters compared to the SM.

Chapter 2

Predictions for Hadron Collider Processes

Precise theoretical predictions for reactions at hadron colliders are indispensable both for the identification of desired signals and for the suppression of background processes. The theoretical description of hadron collisions can be split into a short-range part that can be treated perturbatively due to the asymptotic freedom of QCD [123, 124, 193, 194] at high collision energies, and a long-range part that requires modeling based on experience gained from previous experimental studies.

Factorization in QCD [76] allows the separate treatment of strong dynamics at different scales. Interactions of quarks and gluons, commonly referred to as partons, can be described by perturbation theory at high energies, whereas the composition of hadrons that enter or leave the collision lies in the range of non-perturbative QCD. The perturbative and non-perturbative regimes are separated by the factorization scale μ_F. Note that this scale is completely artificial and not related to a real physical scale. It is only required due to the limitations of current theoretical methods.

The differential cross section $\mathrm{d}\sigma/\mathrm{d}\mathcal{O}$ for an observable $\mathcal{O}$ in a hadronic collision process like inclusive dijet production $h_1 h_2 \to jj + X$ has the factorized form

$$\frac{\mathrm{d}\sigma}{\mathrm{d}\mathcal{O}} = \sum_{a,b} \int_0^1 \mathrm{d}x_a \mathrm{d}x_b \sum_{\mathcal{F}} \int \mathrm{d}\Phi_{\mathcal{F}} f_a^{h_1}(x_a, \mu_F) f_b^{h_2}(x_b, \mu_F) \frac{\mathrm{d}\hat{\sigma}_{ab\to\mathcal{F}}}{\mathrm{d}\hat{\mathcal{O}}} \mathcal{S}_{\mathcal{F}}(\hat{\mathcal{O}} \to \mathcal{O}, \mu_F). \quad (2.1)$$

Here, h_1 and h_2 are the hadrons that enter the collision. The sums run over the partonic constituents a, b of both incoming hadrons and over the partonic final state $\mathcal{F}$ with an associated phase space $\mathrm{d}\Phi_{\mathcal{F}}$. The variables $x_a, x_b \in [0, 1]$ denote the longitudinal momentum fraction of the hadron which is carried by the corresponding parton. Parton distribution functions $f_a^{h_1}(x_a, \mu_F), f_b^{h_2}(x_b, \mu_F)$ capture the compositions of the incoming hadrons in terms of partons with specific momentum fractions at the factorization scale μ_F. The differential cross section $\mathrm{d}\hat{\sigma}_{ab\to\mathcal{F}}/\mathrm{d}\hat{\mathcal{O}}$ of the hard partonic interaction $ab \to \mathcal{F}$ can be calculated in perturbation theory. Measurement functions $\mathcal{S}_{\mathcal{F}}(\hat{\mathcal{O}} \to \mathcal{O}, \mu_F)$ describe the transition from the partonic final state $\mathcal{F}$ to the measured signatures.

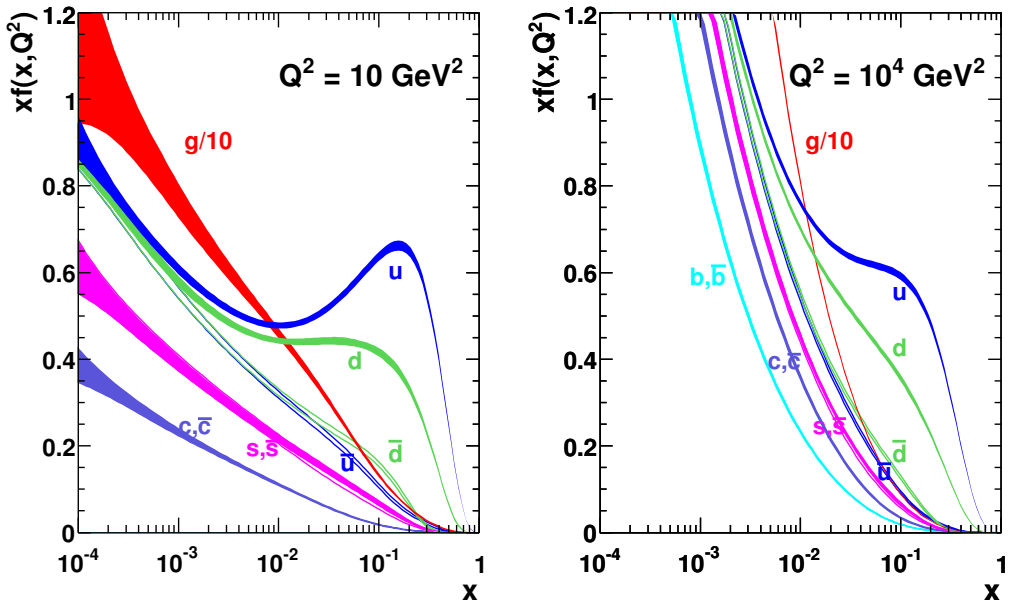

Figure 2.1: Partonic contributions to the proton p at different momentum fractions x according to the MSTW 2008 NLO PDFs with 68% CL uncertainty bands at the scales $Q^2 = 10$ GeV^2 (left) and $Q^2 = 10^4$ GeV^2 (right). For better visibility, the PDF $f_a^p(x, Q)$ of each parton a is scaled by multiplication with the momentum fraction x and the gluon PDF is divided by 10. Figure taken from [171].

2.1 Non-Perturbative QCD

2.1.1 Parton Distribution Functions

Parton distribution functions (PDFs) $f_a^h(x, Q)$ give a description of the density of parton a with longitudinal momentum fraction x inside a hadron h that is probed at the scale Q. Transverse momenta of the partons inside the hadron are integrated out up to the scale Q. Observables in processes with hard hadronic interactions can be expressed as a convolution of universal, i.e. process independent, parton distribution functions and process dependent coefficient functions that can be calculated for each specific case, e.g. for the structure functions of deep inelastic scattering (DIS) [45].

Non-perturbative theoretical methods have not yet succeeded in calculating PDFs purely from theory, hence they need to be determined via fits of experimental data. However, their evolution as function of the scale Q can be calculated in perturbative QCD. In this way, PDFs that were obtained from experimental results at a specific energy scale can be extrapolated to other energies, where they can serve as input for the description of hadron collisions. Evolution equations for parton distribution functions $f_a^h(x, Q)$ have the general form

$$\frac{\partial f_a^h(x,Q)}{\partial \log Q^2} \sim \frac{\alpha_s(Q^2)}{2\pi} \sum_b P_{ab}(x) \otimes f_b^h(x,Q), \tag{2.2}$$

where the convolution with splitting functions P_{ab} determines the mutual influence of PDFs for different partons. The splitting functions for all parton densities have been calculated up to next-to-next-to-leading order (NNLO) in QCD [178, 218].

We illustrate the proton composition at the scales $Q^2 = 10$ GeV^2 and $Q^2 = 10^4$ GeV^2 according to MSTW 2008 NLO PDFs in Fig. 2.1. Uncertainty bands for all partons correspond to 68% confidence level (CL) intervals that were calculated assuming linear propagation of errors from experimental input data according to the Hessian method. For large momentum fractions x, the valence quarks u and d are dominant. At lower momentum fractions, also other quarks and antiquarks provide a significant contribution. Gluons dominate at low x (note that the gluon contribution is divided by 10 in the figure). Contributions from heavy quarks are strongly suppressed.

2.1.2 Hadronization, Decays, and Jets

In the perturbative description of partonic interactions, quarks and gluons are treated as free objects. However, this picture of independent partons is only valid for reactions at energies significantly higher than 1 GeV. During the process of hadronization, color charged partons combine to form color neutral baryons and mesons. Specific hadronization models for the simulation of this non-perturbative dynamic are built into multi-purpose Monte-Carlo (MC) programs. These programs also simulate further effects, including interactions of remnants from the incoming hadrons and the decays of unstable particles, which are necessary for a realistic description of actual events seen in particle detectors.

After the emission of hard QCD radiation in different directions, associated particles form narrow streams in detectors, which are referred to as jets. There is not one single definition of a jet, instead several algorithms for the grouping of particles into jets exist [200, 201]. An important requirement for jet algorithms is infrared safety, which refers to stability under the emission of soft particles and under collinear splittings [208].

Sequential recombination algorithms use distance measures to determine the separation between particles, merge particles with separations below a chosen threshold into one object and identify all separate objects at the end of the combination procedure as jets. A prominent group of sequential recombination algorithms is based on the measures d_{ij} for the distance between particles i and j and d_{iB} for the distance of particle i to the beam. The latter is determined by the transverse momentum p_{T}^i of particle i as

$$d_{iB} = (p_{\mathrm{T}}^i)^{2p}, \tag{2.3}$$

where p is an integer parameter that has different values for different versions of the algorithm. Two particles i and j are assigned the distance

$$d_{ij} = \min\left[(p_{\mathrm{T}}^i)^{2p}, (p_{\mathrm{T}}^j)^{2p}\right] \frac{\Delta R_{ij}^2}{R^2}, \tag{2.4}$$

which uses the separation in rapidity y and azimuthal angle ϕ via

$$\Delta R_{ij}^2 = (y_i - y_j)^2 + (\phi_i - \phi_j)^2. \tag{2.5}$$

This separation is normalized to R, a free parameter of the algorithm that is typically set to a value between 0.4 and 1.

Step by step, the algorithm proceeds as:

- calculate the distances d_{ij} and d_{iB},
- determine the minimum of d_{ij} and d_{iB},
- if one of the d_{ij} is minimal, merge particles i and j and go back to the first step,

- if one of the d_{iB} is minimal, move particle i to the list of jets and go back to the first step,
- stop, if no more particles are left.

If the parameter p is set to one, this algorithm is known as k_T algorithm [64, 65, 93]. For $p = 0$, it goes under the name Cambridge/Aachen algorithm [88, 228] and for $p = -1$, it is called anti-k_T algorithm [60]. All of these three versions are infrared safe.

2.2 Perturbative QCD

The probability P for the transition from an incoming state, which is described by the quantum mechanical wavepacket $|\text{in}\rangle$, to a final state $|\text{out}\rangle$ is given by the modulus squared of the overlap between both states after the asymptotic evolution of the incoming state for long time as described by the unitary S-matrix:

$$P = |\langle \text{out}| \, S \, |\text{in}\rangle|^2 \,. \tag{2.6}$$

The part of the S-matrix that describes interactions is collected in the T-matrix according to

$$S = \mathbb{1} + iT. \tag{2.7}$$

In a collision process $ab \to \{f\}$, where two incoming particles a with four-momentum $p_a = (E_a, p_a^x, p_a^y, p_a^z)$ and b with four-momentum $p_b = (E_b, p_b^x, p_b^y, p_b^z)$ are converted into several final state particles f with four-momenta $p_f = (E_f, p_f^x, p_f^y, p_f^z)$, energy and momentum are conserved. From T the invariant matrix element $\mathcal{M}$ of the scattering process can be obtained via

$$\langle \{p_f\}| \, iT \, |p_a p_b\rangle = (2\pi)^4 \delta^{(4)} \left(p_a + p_b - \sum_f p_f \right) i\mathcal{M}. \tag{2.8}$$

When $\mathcal{M}$ is known, the partonic differential cross section $\mathrm{d}\hat{\sigma}$ can be calculated as

$$\mathrm{d}\hat{\sigma} = \frac{1}{(2E_a)(2E_b)\,|v_a - v_b|} \left(\prod_f \frac{\mathrm{d}^3 p_f}{(2\pi)^3} \frac{1}{2E_f} \right) (2\pi)^4 \delta^{(4)} \left(p_a + p_b - \sum_f p_f \right) |\mathcal{M}|^2 \,. \tag{2.9}$$

Here, v_a and v_b are the velocities of particles a and b in the laboratory frame.

Perturbation theory uses an expansion in powers of the couplings to determine the modulus squared of the invariant matrix element $|\mathcal{M}|^2$. This expansion is only valid if the couplings are much smaller than one. Couplings run as a function of the energy scale of the reaction. Their evolution is described by renormalization group equations. Current collision experiments at the LHC achieve partonic energies of several hundred GeV up to a few TeV in the hardest interactions. In this energy range, all Standard Model couplings are small enough to allow for the application of perturbation theory with high accuracy. As a rough estimate, the strong coupling ($\alpha_s \approx 0.1$) is one order of magnitude larger than electroweak couplings ($\alpha \approx 0.01$).

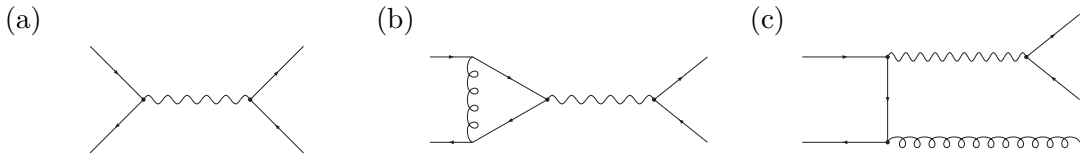

Figure 2.2: Representative Born (a), virtual (b), and real-emission (c) Feynman diagrams.

2.2.1 Fixed-Order Calculations

Feynman diagrams are an established tool for the perturbative evaluation of the invariant matrix element $\mathcal{M}$. They offer a convenient way to depict terms in the perturbative expansion of $\mathcal{M}$ as graphs where the incoming and outgoing particles of a scattering process are connected through interaction vertices with each other and with virtual internal particles. Via the interference of diagrams with the right number of couplings, $|\mathcal{M}|^2$ can be determined at a given order of perturbation theory.

The invariant matrix element $\mathcal{M}$ can be calculated by the evaluation of all connected amputated Feynman diagrams. A diagram is called connected if two arbitrary parts of the diagram are always linked by a chain of lines and vertices inside the diagram. The amputation procedure removes loops on external legs of the diagrams in the following way [192]: For each external leg, one proceeds from the end of this leg along the lines of the diagram until one reaches the last point where the leg can be disconnected from the rest of the diagram by cutting a single propagator. The diagram is cut at this position, all external structures of the leg are removed, and the corresponding wavefunction of the external particle is attached as ending of the leg.

Leading order (LO) perturbative predictions for $|\mathcal{M}|^2$ are obtained from the interference of all diagrams with the minimal number of couplings for a given set of external particles. Spin, color, and polarization degrees of freedom of final state particles are added up, whereas for incoming particles the average is calculated by division of the sum through appropriate normalization factors. The leading order result for $|\mathcal{M}|^2$ is also referred to as Born approximation B. External particle momenta span the corresponding Born phase space $\mathrm{d}\Phi_B$.

Higher order corrections involve additional loops inside the diagrams and additional external particles in the final state. Both internal loop corrections and corrections with more external particles separately exhibit infrared (IR) divergences. According to the Kinoshita-Lee-Nauenberg (KLN) theorem [156, 165], IR divergences cancel for inclusive quantities at any fixed order of perturbation theory.

At next-to-leading order, the Born result B is supplemented by virtual corrections V and real-emission corrections R. The virtual NLO contribution V to $|\mathcal{M}|^2$ consists of the interference of Born diagrams with one-loop corrections that have the same external particles but one additional internal loop. In the real-emission contribution R, diagrams with one additional final state particle are interfered with themselves. We illustrate Born, virtual, and real-emission diagrams for the Drell-Yan process in Fig. 2.2.

When the prefactors in Eq. (2.9) are suppressed, the differential cross section at NLO can be written in the form

$$\mathrm{d}\hat{\sigma} = \mathrm{d}\Phi_B \left(B\left(\Phi_B\right) + \hat{V}\left(\Phi_B\right) \right) + \mathrm{d}\Phi_R \, R\left(\Phi_R\right). \tag{2.10}$$

Here, $\hat{V}$ stands for the renormalized virtual contribution, i.e. the sum of the bare virtual contribution V and counterterms for ultraviolet (UV) divergences. Both virtual and real-emission terms include an appropriate infrared regulator. The treatment of associated divergences is discussed in Sec. 2.4. Compared to the Born phase space $\mathrm{d}\Phi_B$, the real-emission phase space $\mathrm{d}\Phi_R$ contains the additional degrees of freedom of the radiated parton in $\mathrm{d}\Phi_{\mathrm{rad}}$ and can be written as product $\mathrm{d}\Phi_R = \mathrm{d}\Phi_B \mathrm{d}\Phi_{\mathrm{rad}}$. Analogous to Eq. (2.10), the NLO prediction for an observable $\mathcal{O}$ can be written as

$$\langle \mathcal{O} \rangle_{\mathrm{NLO}} = \int \mathrm{d}\Phi_B \; \mathcal{O}\left(\Phi_B\right) \Big(B\left(\Phi_B\right) + \hat{V}\left(\Phi_B\right) \Big) + \int \mathrm{d}\Phi_R \; \mathcal{O}\left(\Phi_R\right) R\left(\Phi_R\right). \tag{2.11}$$

Fixed-order calculations can only be used for inclusive predictions, i.e. the production of all objects under consideration plus "anything else" that is not further specified, because of the necessary cancelation of IR divergences between virtual and real-emission corrections. Exclusive predictions for an exactly specified group of final state objects can be obtained in the combination with parton showers, as described below.

2.2.2 Parton Shower

Parton showers are a tool for the recursive generation of a multitude of color charged particles which are produced by the strong interaction in hadron collisions. They allow to make predictions which lie beyond the reach of fixed-order calculations, not only due to high particle multiplicities, but also by the generation of completely exclusive events.

The parton shower approach is based on the approximate factorization of processes with $n+1$ particles in the limit where one parton becomes soft or collinear to another one into an n-particle process and the emission of this parton. For soft gluon emission, coherence effects must be taken into account at the amplitude level. Collinear parton emissions can be described by the factorization of an $(n+1)$-particle cross section $\mathrm{d}\hat{\sigma}_{n+1}$ into an n-particle cross section $\mathrm{d}\hat{\sigma}_n$ and one emission according to

$$\mathrm{d}\hat{\sigma}_{n+1}\left(\Phi_{n+1}\right) = \mathcal{P}\left(\Phi_{\mathrm{rad}}\right) \mathrm{d}\hat{\sigma}_n\left(\Phi_n\right) \mathrm{d}\Phi_{\mathrm{rad}}. \tag{2.12}$$

The $(n+1)$-particle phase space $\mathrm{d}\Phi_{n+1}$ is split into the product of an n-particle phase space space $\mathrm{d}\Phi_n$ and the radiation phase space $\mathrm{d}\Phi_{\mathrm{rad}}$. The function $\mathcal{P}$ is usually averaged over the azimuthal angle in the splitting. Two remaining degrees of freedom in the radiation phase space can be expressed as a hardness scale q, like the transverse momentum of the emitted particle, and the longitudinal momentum fraction z of the emitter after the emission. In this parameterization, the n-particle cross section $\mathrm{d}\hat{\sigma}_n$ is multiplied by the emission factor

$$\frac{\alpha_s(q)}{\pi} \frac{1}{q} P(z) \mathrm{d}z \mathrm{d}q. \tag{2.13}$$

P is known as DGLAP splitting function [121, 122, 167, 22, 87]. Cut-offs q_0 and z_0 for the hardness scale and the longitudinal momentum fraction, respectively, implement thresholds below which emissions are considered to be unresolvable. For emission processes that are described according to Eq. (2.13), the probability of no emission between two hardness scales q_1 and q_2 is given by the Sudakov form factor [212]

$$\Delta_{\mathrm{S}}\left(q_1, q_2\right) = \exp\left[- \int_{q_2}^{q_1} \mathrm{d}q \; \frac{\alpha_s(q)}{\pi} \frac{1}{q} \int_{z_0}^{1} \mathrm{d}z \; P(z) \right]. \tag{2.14}$$

Parton showers start at a given n-particle configuration and add partons repeatedly based on the approximate factorization in the soft and collinear limits. When the evolution of the emissions reaches energy scales where the strong coupling becomes large and perturbation theory is no longer applicable, the parton shower stops and hadronization takes over.

At each order of perturbation theory, the diagrams with extended tree structure due to the multiple parton emissions are connected to the loop corrections via unitarity. This relation can be used to extract leading logarithmic (LL) approximations of the loop corrections. By the inclusion of these terms, the recursive evolution of the parton shower resums the complete leading logarithmic contributions to all orders in the strong coupling constant.

The practical implementation of parton showers for the simulation of collider reactions is provided by multi-purpose Monte-Carlo generators. They use pseudo-random numbers to determine iteratively the emission scales in parton showers, which are simulated by specific parton shower models. Several of these programs are available to the public at the time of writing. Prominent examples are `HERWIG 6.5` [170, 78, 79], `HERWIG++ 2.7` [32, 40], `PYTHIA 6.4` [205], `PYTHIA 8.1` [206], and `SHERPA 2.1` [117]. For an examination of the specific features of these programs and a general discussion of MC event generators, we refer to [57]. We elaborate on the parton shower implementations in `PYTHIA 6.4`, since we use these showers in our slepton studies.

2.2.2.1 Parton Showers in PYTHIA

Each step of the parton shower evolution, where a mother parton a splits into two daughter partons b and c, is described in `PYTHIA` by two variables, the squared energy scale q^2 of the splitting and the momentum fraction $z \in [0, 1]$ of daughter b after the splitting. Initial-state showers before the hard interaction and final-state showers after it are described by two separate algorithms. In chronological order, the initial-state shower evolves from a minimal cut-off scale q_0^2 with the default value 1 GeV^2 up to the maximal scale $q_{\max}^2$ in the shower, which has to be chosen according to the energy scale of the hard interaction. Subsequently, the final-state shower performs the evolution from the high scale $q_{\max}^2$ down to the low scale q_0^2, where the shower stops. Energy and momentum are conserved in all steps of the shower evolution.

The original implementations of initial-state showers [204, 43, 177] via the `PYSSPA` algorithm and of final-state showers [42, 41, 186] via the `PYSHOW` algorithm use the invariant mass squared of the mother parton as evolution scale q^2 which defines the order of the shower. A chronological evolution of the initial state shower would require knowledge of the whole tree of emissions to determine the parton that enters the hard interaction. Instead, the connection of the initial-state parton shower to the hard interaction is established via backwards evolution [204, 43], starting at the high scale of the hard interaction and evolving step by step to the incoming hadron. The routines `PYPTIS` for initial-state showers and `PYPTFS` for final-state showers, that were added subsequently [207], generate parton showers which are ordered according to the transverse momentum in each splitting. In all of these shower routines, the running strong coupling α_s is evaluated at the squared transverse momentum p_{T}^2 for each splitting, since higher order calculations [26, 80] showed that this scale choice resums corrections to the leading logarithmic terms, which can become large in certain regions of phase space.

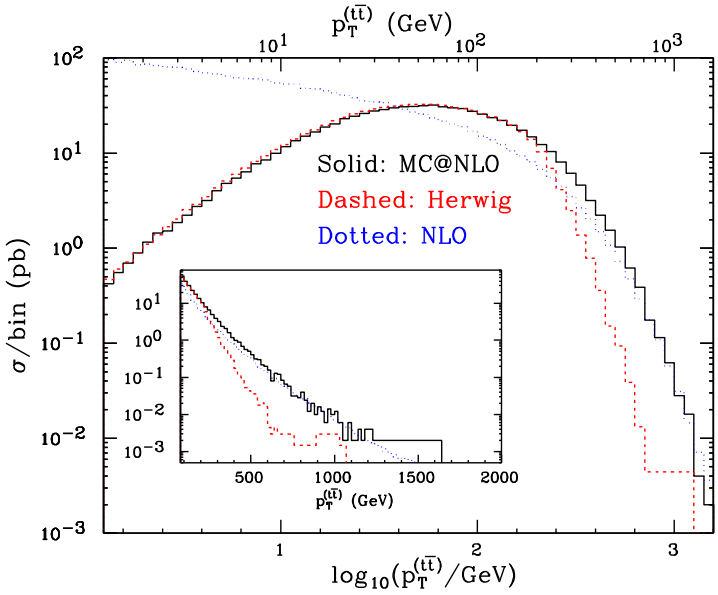

Figure 2.3: Distribution of $p_{\mathrm{T}}^{(t\bar{t})}$ at the LHC with 14 TeV center-of-mass energy in proton collisions generated with parton showers matched to NLO matrix elements in `MC@NLO` (black, solid), LO matrix elements supplemented by parton showers in `Herwig` (red, dashed), and pure matrix elements at NLO (blue, dotted). Figure taken from [106].

2.3 Matching with POWHEG

Calculations in perturbation theory beyond leading order and LO matrix elements that are supplemented by parton showers produce reliable results in complementary regions of phase space. Since parton showers are based on the approximate factorization of soft and collinear configurations, they should not be used for the generation of hard emissions. On the contrary, matrix elements from higher-order calculations provide accurate descriptions of all included hard emissions, but they contain logarithms of scale ratios that can become large in soft or collinear limits. For reliable predictions in these regions of phase space, the large logarithmic terms need to be resummed to all orders in the strong coupling constant, either by an analytic calculation or in a parton shower. We illustrate the differences between LO matrix elements in combination with parton showers and pure NLO matrix elements in Fig. 2.3 using the results of Ref. [106] for top quark pair production in the process $pp \to t\bar{t} + X$ at the LHC. The distribution of $p_{\mathrm{T}}^{(t\bar{t})}$, the magnitude of the vectorial sum of $t\bar{t}$ transverse momenta, demonstrates the characteristic features of both methods when the recoil of QCD radiation against the $t\bar{t}$ pair is either small or large.

To obtain a description that is valid both in soft or collinear limits and for hard emissions, it is desirable to combine the advantages of higher-order matrix elements and parton showers. When parton showers are added to a Born matrix element, they dress a part of the events with additional radiation based on a probabilistic method. Consequently, the total number of events is not changed and parton showers preserve the LO accuracy for inclusive observables. In the combination of NLO matrix elements with parton showers, special matching schemes are required. Since the parton shower includes leading logarith-

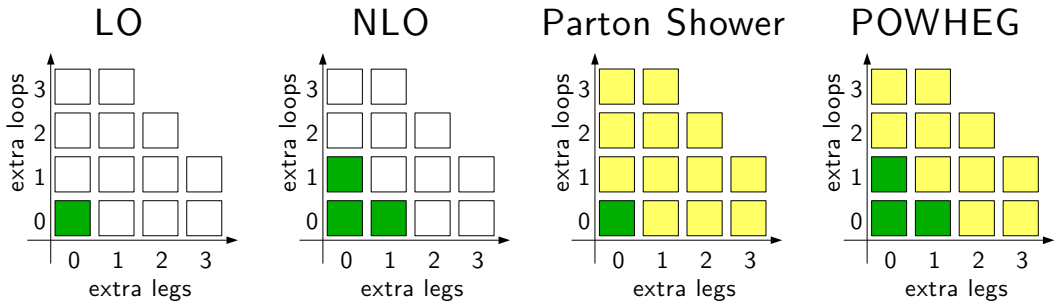

Figure 2.4: Illustration in the style of Ref. [208] of the perturbative accuracy in fixed-order LO and NLO calculations, in conventional parton showers as implemented in multi-purpose MC programs, and in parton showers matched to NLO calculations as achieved by POWHEG. Contributions with a specific number of additional loops and legs compared to the Born diagrams are either included exactly (green), included in leading logarithmic approximation (yellow), or not included (white).

mic approximations of the exact $\mathcal{O}(\alpha_s)$ corrections to the Born matrix element which are part of the NLO result, a careful combination is necessary to avoid double counting.

We compare the perturbative accuracy of parton showers that are consistently matched to NLO matrix elements to the respective accuracies of fixed-order LO and NLO results and of standard parton showers in Fig. 2.4. Each additional loop and each additional leg in the Feynman diagrams increases the power of the strong coupling constant α_s in the squared matrix element by one. The sum of extra loops and legs compared to the Born diagrams is a constant at fixed perturbative order. Note that multiple loops can be distributed is several ways to both parts of the diagrammatic interference.

Two methods for the matching of NLO matrix elements to parton showers have been proposed in the literature and used in numerous applications: MC@NLO [107] and POWHEG [180, 104]. They provide a smooth interpolation between the parton-shower result in soft or collinear regions and the NLO result in hard regions, as illustrated in Fig. 2.3. Both MC@NLO and POWHEG achieve the perturbative accuracy which is depicted in the right-most panel of Fig. 2.4, but they deviate by terms of higher order than NLO in the strong coupling. A comparison of both methods is given in [183].

Our calculations are based on the POWHEG approach, which is described in the next subsection. The POWHEG method has been applied to a broad variety of processes. Standard Model processes form the majority among POWHEG applications. Massive vector bosons have been studied both in single [14, 46, 36, 202] and in pair production [175, 184], as well as in combination with up to two jets [17, 176, 149, 195, 146, 150, 63, 145]. Pure QCD processes extend up to the production of three jets [152]. Several Higgs production mechanisms that were examined in the POWHEG approach [15, 182, 31, 62], assisted in the discovery of a Higgs boson at the LHC [6, 69] in 2012.

Applications of the POWHEG method to supersymmetric theories include the production of supersymmetric Higgs bosons in gluon fusion [31] and a recent examination of squark pair production [110, 111]. Large parts of the work for this thesis were presented in publications describing the POWHEG implementations of slepton pair production [147] and the production of a slepton pair in association with a jet [148].

2.3.1 Details of the POWHEG Method

POWHEG (an acronym for POsitive Weight Hardest Emission Generator) is a method for the consistent matching of a fixed-order NLO QCD calculation to parton showers. It was proposed in [180] and described in detail in [104]. The POWHEG method uses the real-emission contribution of an NLO result to generate the parton emission with the largest transverse momentum first. Subsequent radiation in the parton shower is required to be softer than the first emission. This is fulfilled in the case of transverse-momentum ordered parton showers when the starting scale is set to the p_{T} value of the previous emission, otherwise a p_{T} veto must be included in the shower. POWHEG is not restricted to a specific parton shower program, no modifications are necessary to combine it with any of these programs that satisfies the requirements on transverse momentum ordering in the shower as outlined above.

We illustrate the POWHEG method in the case of only one singular region in the real-emission contribution based on the discussion of Higgs boson production in gluon fusion that was presented in Ref. [183]. Infrared singular behavior in this example is found when the Higgs boson transverse momentum p_{T} and conversely also the transverse momentum of the additional final-state parton approaches zero. When several singular regions are present, they can be split into a sum of terms with specific flavor structure that are each singular in one collinear region only, as explained in detail in the original publication [104].

By defining

$$R^{\mathrm{S}} = R\frac{c^2}{c^2 + p_{\mathrm{T}}^2}, \qquad R^{\mathrm{F}} = R\frac{p_{\mathrm{T}}^2}{c^2 + p_{\mathrm{T}}^2}, \tag{2.15}$$

with a non-zero constant c, we can decompose the real-emission contribution $R = R^{\mathrm{S}} + R^{\mathrm{F}}$ into a part R^{S} which contains the infrared singularities and a finite part R^{F} that can be integrated over the whole real-emission phase space $\mathrm{d}\Phi_R$. The real-emission phase space $\mathrm{d}\Phi_R$ is the product of the Born part $\mathrm{d}\Phi_B$ and the radiation part $\mathrm{d}\Phi_{\mathrm{rad}}$ that contains the additional degrees of freedom for the real-emission contribution.

POWHEG uses the combination of the Born contribution B, the renormalized virtual contribution $\hat{V}$, and the singular part R^{S} of the real-emission contribution in

$$\overline{B}^{\mathrm{S}} = B + \hat{V} + \int \mathrm{d}\Phi_{\mathrm{rad}} R^{\mathrm{S}} \tag{2.16}$$

for its prediction of the differential cross section $\mathrm{d}\hat{\sigma}$ according to

$$\mathrm{d}\hat{\sigma} = \mathrm{d}\Phi_B \overline{B}^{\mathrm{S}} \left[\Delta_{\mathrm{S}}\left(q_0\right) + \Delta_{\mathrm{S}}\left(p_{\mathrm{T}}\right) \frac{R^{\mathrm{S}}}{B} \mathrm{d}\Phi_{\mathrm{rad}}\right] + R^{\mathrm{F}} \mathrm{d}\Phi_R. \tag{2.17}$$

Here, Δ_{S} is the POWHEG Sudakov form factor

$$\Delta_{\mathrm{S}}\left(k_{\mathrm{T}}\right) = \exp\left[-\int \mathrm{d}\Phi_{\mathrm{rad}} \frac{R^{\mathrm{S}}}{B} \theta\left(p_{\mathrm{T}}\left(\Phi_{\mathrm{rad}}\right) - k_{\mathrm{T}}\right)\right] \tag{2.18}$$

which includes a Heaviside function θ that limits the integration region to those parts of the radiation phase space $\mathrm{d}\Phi_{\mathrm{rad}}$ where the transverse momentum $p_{\mathrm{T}}\left(\Phi_{\mathrm{rad}}\right)$ is larger than the fixed value k_{T}.

For an infrared-safe observable $\mathcal{O}$, the corresponding POWHEG prediction is

$$\langle\mathcal{O}\rangle_{\mathrm{PWG}} = \int \mathrm{d}\Phi_B\, \overline{B}^{\mathrm{S}} \left[\mathcal{O}\left(\Phi_B\right)\Delta_{\mathrm{S}}\left(q_0\right) + \int \mathrm{d}\Phi_{\mathrm{rad}}\, \mathcal{O}\left(\Phi_R\right)\Delta_{\mathrm{S}}\left(p_{\mathrm{T}}\right)\frac{R^{\mathrm{S}}}{B}\right] + \int \mathrm{d}\Phi_R\, \mathcal{O}\left(\Phi_R\right) R^{\mathrm{F}}. \tag{2.19}$$

To demonstrate the NLO accuracy of Eq. (2.19), we transform it into Eq. (2.11) neglecting all terms beyond $\mathcal{O}\left(\alpha_s\right)$. We start by adding $0 = \mathcal{O}\left(\Phi_B\right) - \mathcal{O}\left(\Phi_B\right)$ to $\mathcal{O}\left(\Phi_R\right)$ in the integral over $\mathrm{d}\Phi_{\mathrm{rad}}$ and rearranging the terms in the following way:

$$\begin{aligned}
\langle\mathcal{O}\rangle_{\mathrm{PWG}} &= \int \mathrm{d}\Phi_B\, \overline{B}^{\mathrm{S}}\mathcal{O}\left(\Phi_B\right)\Delta_{\mathrm{S}}\left(q_0\right) \\
&\quad + \int \mathrm{d}\Phi_B \int \mathrm{d}\Phi_{\mathrm{rad}}\, \overline{B}^{\mathrm{S}}\left[\mathcal{O}\left(\Phi_R\right) + \mathcal{O}\left(\Phi_B\right) - \mathcal{O}\left(\Phi_B\right)\right]\Delta_{\mathrm{S}}\left(p_{\mathrm{T}}\right)\frac{R^{\mathrm{S}}}{B} \\
&\quad + \int \mathrm{d}\Phi_R\, \mathcal{O}\left(\Phi_R\right) R^{\mathrm{F}} \\
&= \int \mathrm{d}\Phi_B\, \overline{B}^{\mathrm{S}}\mathcal{O}\left(\Phi_B\right)\left[\Delta_{\mathrm{S}}\left(q_0\right) + \int \mathrm{d}\Phi_{\mathrm{rad}}\, \Delta_{\mathrm{S}}\left(p_{\mathrm{T}}\right)\frac{R^{\mathrm{S}}}{B}\right] \\
&\quad + \int \mathrm{d}\Phi_R\, \left[\mathcal{O}\left(\Phi_R\right) - \mathcal{O}\left(\Phi_B\right)\right]\Delta_{\mathrm{S}}\left(p_{\mathrm{T}}\right) R^{\mathrm{S}}\frac{\overline{B}^{\mathrm{S}}}{B} \\
&\quad + \int \mathrm{d}\Phi_R\, \mathcal{O}\left(\Phi_R\right) R^{\mathrm{F}}.
\end{aligned} \tag{2.20}$$

The term in square brackets in the fourth line is one as a consequence of unitarity. Furthermore, since the real-emission term R^{S} in the fifth line contributes at the highest perturbative order which is considered, all terms in the expansions of $\Delta_{\mathrm{S}}\left(p_{\mathrm{T}}\right)$ and $\overline{B}^{\mathrm{S}}/B$ as $1+\mathcal{O}\left(\alpha_s\right)$ respectively apart from the leading one can be dropped in this line. Inserting the definition of $\overline{B}^{\mathrm{S}}$, we find

$$\begin{aligned}
\langle\mathcal{O}\rangle_{\mathrm{PWG}} &= \int \mathrm{d}\Phi_B\, \mathcal{O}\left(\Phi_B\right)\left[B + \hat{V} + \int \mathrm{d}\Phi_{\mathrm{rad}} R^{\mathrm{S}}\right] \\
&\quad + \int \mathrm{d}\Phi_R\, \left[\mathcal{O}\left(\Phi_R\right) - \mathcal{O}\left(\Phi_B\right)\right] R^{\mathrm{S}} \\
&\quad + \int \mathrm{d}\Phi_R\, \mathcal{O}\left(\Phi_R\right) R^{\mathrm{F}}. \\
&= \int \mathrm{d}\Phi_B\, \mathcal{O}\left(\Phi_B\right)\left[B + \hat{V}\right] + \int \mathrm{d}\Phi_R\, \mathcal{O}\left(\Phi_R\right)\left[R^{\mathrm{S}} + R^{\mathrm{F}}\right] \\
&= \langle\mathcal{O}\rangle_{\mathrm{NLO}}\,.
\end{aligned} \tag{2.21}$$

2.4 Regularization and Renormalization

The evaluation of Feynman diagrams frequently leads to expressions that exhibit both ultraviolet and infrared divergences. In this case, a regularization procedure for all divergences is required. Within well-defined regularized expressions, divergences assume a definite shape so that one gains control over them, and their cancelation in the complete result becomes evident before the regularization is removed.

A regularization procedure should respect the symmetries of the underlying theory, otherwise the symmetries need to be restored by the addition of appropriate terms. Dimensional regularization [215, 49, 74] is a very popular regularization scheme for Standard Model calculations since it respects both the gauge symmetries and the space-time symmetries of the SM. We introduce dimensional regularization and discuss its compatibility with SUSY in Sec. 2.4.1. It is the regularization method that we use for all of our fixed order perturbative calculations.

Divergences that appear in different parts of an NLO calculation cancel when these parts are combined in meaningful observables. Ultraviolet divergences are removed in an appropriate renormalization procedure as described in Sec. 2.4.2. Infrared divergences result from collinear or soft configurations. Collinear divergences in the initial state are absorbed into the parton distribution functions of the incoming hadrons. Soft and collinear final state divergences cancel between the real-emission contribution and the virtual contribution of an NLO calculation.

Infrared divergences in virtual corrections arise during the integration over virtual loop momenta, whereas infrared divergences in real-emission corrections arise during the integration over the external particle phase space. The infrared poles of virtual loop integrals can be extracted analytically. In the real-emission part, the final state phase space is in general too complex for a completely analytical integration. However, the infrared poles of the real-emission contribution can be extracted, if the phase space is split into regions which contain only single infrared limits or at most the combined soft and collinear limit of one specific parton. Several schemes for this splitting have been proposed in the literature. One prominent example is the dipole subtraction method [66, 67]. Our programs for slepton studies use the subtraction scheme that was proposed by Frixione, Kunszt and Signer [103, 102]. We summarize the central ideas of this scheme in Sec. 2.4.3.

2.4.1 Dimensional Regularization

Dimensional regularization uses the number D of space-time dimensions as a regulator for integrals that diverge in four dimensions. In perturbative calculations, dimensional regularization is an established tool that leads to well-defined results. After the cancelation of all regularized divergences, the limit $D \to 4$ is taken, which removes the regulator and gives the result for the familiar number of space-time dimensions.

We discuss integration in D dimensions for an Euclidean vector space. This space is related to the Minkowski space of a Poincaré invariant field theory with one time dimension and $D-1$ space dimensions via a Wick rotation [226]. For our calculations at next-to-leading order, it is sufficient to consider the D-dimensional integration over one loop momentum q.

Integration in D dimensions should be regarded [227, 74] as the operation of a functional that fulfills specific properties which are established for conventional integrals. The corresponding vector space of space-time momenta is infinitely dimensional. For integer values of D, the functional has to reproduce the known results for integrable functions via the projection onto an appropriate subspace. Apart from an overall normalization factor, integration in this framework is determined uniquely [227] by the axioms of

- linearity

$$\int \mathrm{d}^D q \;\; [a \; f(q) + b \; g(q)] = a \int \mathrm{d}^D q \; f(q) + b \int \mathrm{d}^D q \; g(q), \tag{2.22}$$

- scaling

$$\int \mathrm{d}^D q \; f(sq) = s^{-D} \int \mathrm{d}^D q \; f(q), \tag{2.23}$$

- translation invariance

$$\int \mathrm{d}^D q \; f(q+r) = \int \mathrm{d}^D q \; f(q). \tag{2.24}$$

The number D of space-time dimensions is implemented by the scaling property. To fix the overall normalization factor, the integral of the D-dimensional Gauß function is chosen as

$$\int \mathrm{d}^D q \; \exp\left(-q^2\right) = \pi^{D/2}. \tag{2.25}$$

We illustrate the evaluation of a D-dimensional momentum integral over a scalar function following the description given in [74], where also more general integrands are considered. A scalar function f depends only on the scalar products of the integration momentum q and a finite number of external momenta $p_1, \ldots, p_J$. Splitting the integration momentum

$$q = q_\parallel + q_\perp \tag{2.26}$$

into a vector $q_\parallel$ which lies inside the J-dimensional subspace spanned by $p_1, \ldots, p_J$ and a vector $q_\perp$ orthogonal to that subspace, the integration over q can be broken down to two subsequent integrations. The integral over the $(D-J)$-dimensional space orthogonal to $p_1, \ldots, p_J$ can be performed using spherical symmetry, which multiplies f by the factor $\frac{2\pi^{(D-J)/2}}{\Gamma((D-J)/2)} \, |q_\perp|^{D-J-1}$ corresponding to the surface of a $(D-J)$-dimensional hypersphere with radius $|q_\perp|$. One remaining integration over the magnitude $|q_\perp|$ of $q_\perp$ from this first step and the subsequent integration over $q_\parallel$ both take place in integer dimensions, hence they can be performed with conventional integrals. In summary, the D-dimensional integration over f has the result

$$\int \mathrm{d}^D q \; f\left(q\right) = \frac{2\pi^{(D-J)/2}}{\Gamma((D-J)/2)} \int \mathrm{d}^J q_\parallel \int_0^\infty \mathrm{d}\,|q_\perp| \;\; |q_\perp|^{D-J-1} \, f\left(q\right). \tag{2.27}$$

To keep the mass dimension of integrals over D dimensional momenta fixed, they are multiplied by the prefactor $(\mu_R)^{(4-D)}$. The artificial renormalization scale μ_R with the mass dimension one has no physical meaning, but it does not drop out of the results for scattering amplitudes in general. In numerical evaluations, it should be chosen close to the physical scales of the process under consideration to avoid the generation of large logarithms.

Several variants of dimensional regularization have been proposed that differ in the structures which are promoted to D dimensions. The original method by 't Hooft and Veltman (HV) [215] treats internal particles in D dimensions, whereas particles on the external legs of Feynman diagrams are kept in four dimensions. Conventional dimensional regularization (CDR) [49] treats all particles in D dimensions. Both of these methods are consistent regularization schemes that preserve unitarity. In contrast, some other suggested versions of dimensional regularization cannot be used at arbitrary order of perturbation theory, even if they are very successful at NLO, see the explicit example given in [155].

Dimensional regularization can be used to regularize UV and IR divergences by the same regulator. If dimensional regularization is applied as infrared regulator, it is necessary to treat the corresponding external particles in D dimensions. While these infrared

divergences must be inspected in detail in the HV scheme, CDR has the advantage that all external particles are treated in D dimensions, so that no special considerations are required for the regularization of IR divergences. In all of our calculations, we use CDR for the regularization of both UV and IR divergences.

The modified number of space-time dimensions in dimensional regularization is not limited to momentum vectors, but affects all objects with Lorentz structures, like the metric tensor $g_{\mu\nu}$ and Dirac matrices γ^μ. A contraction of the metric tensor $g_{\mu\nu}$ and its inverse $g^{\mu\nu}$ returns the number of space-time dimensions, i.e. $g^\mu_\mu = g_{\mu\nu}g^{\mu\nu} = D$. Dirac matrices γ^μ fulfill the D-dimensional anticommutation relation $\{\gamma^\mu, \gamma^\nu\} = 2g^{\mu\nu}$. The matrix γ_5 does not have a straightforward generalization to D dimensions (we discuss this issue in Sec. 4.2). Massless vector bosons in D dimensions exhibit $D-2$ degrees of freedom, as can be seen in the Lorentz contraction of the sum over polarizations λ via the formula

$$\sum_\lambda \varepsilon^*_\mu(k,\lambda)\varepsilon_\nu(k,\lambda) = -g_{\mu\nu} + \frac{n_\mu k_\nu + n_\nu k_\mu}{n\cdot k}. \tag{2.28}$$

Here, $\varepsilon_\mu(k,\lambda)$ denotes the polarization vector of a vector boson with four-momentum k and polarization state λ. n is a light-like auxiliary vector with $n\cdot k \neq 0$. Intermediate terms proportional to $(D-4)$ lead in combination with poles in $(D-4)$ to non-vanishing contributions in the limit $D \to 4$. Hence it is necessary to keep them in all steps of the calculation until the regulator is removed. It is often convenient to use a variable ϵ that denotes the difference between D and 4 dimensions and thus vanishes in the limit $D \to 4$. We use the normalization $D = 4 - 2\epsilon$.

Special attention is necessary when dimensional regularization is applied to supersymmetric theories. In dimensional regularization, four-dimensional bosonic structures, like the number of space-time dimensions, are promoted to D dimensions. Fermionic structures, however, remain in four dimensions. For example, the unit matrix in Dirac space retains the trace $\mathrm{Tr}\,(\mathbb{1}) = 4$. This is in conflict with the symmetry between bosons and fermions in SUSY and can make the addition of terms that restore supersymmetry necessary.

At next-to-leading order in supersymmetric quantum chromodynamics (SQCD), the mismatch between fermionic and bosonic degrees of freedom in dimensional regularization results in a deviation between the QCD coupling constant g_s, and the SUSY-related Yukawa coupling constant $\hat{g}_s$ proportional to the square of the coupling constant [173]. While it is necessary to take this deviation into account for general SQCD calculations, neither of the processes considered here contains the strong SUSY Yukawa interaction at Born level. Consequently, all effects of SUSY violation by dimensional regularization lie beyond the maximal power of the strong coupling in our calculation.

2.4.2 Renormalization Schemes

Experiments cannot measure the bare parameters of the Lagrangian $\mathcal{L}$ of a quantum field theory directly. Instead, they determine renormalized couplings and charges which are related to the bare parameters by the choice of a specific renormalization scheme. In the transition from bare parameters to renormalized parameters, UV divergences are removed by the inclusion of appropriate counterterms. While the UV poles in the counterterms are fixed by the requirement of overall UV finiteness, terms without UV divergences can be chosen freely in the renormalization conditions.

Common renormalization schemes often choose the finite terms in such a way that the number of terms in perturbative calculations is reduced or the relation between renormalized parameters and experimental observables is particularly simple. We use a combination of two schemes in our calculations: The on-shell scheme [197], which relates the renormalized parameters to free asymptotic states, and the $\overline{\text{MS}}$ scheme [34], where only UV divergences and universal constant terms are subtracted.

In the on-shell scheme, the renormalization conditions are chosen such that the theory is parametrized in terms of asymptotic long-distance values of the basic parameters, like the measured electron mass and coupling in quantum electrodynamics (QED). It can be convenient to use the on-shell renormalization conditions even in theories like QCD, where particles with color charges are not observed as free objects at long distances. In particular, self-energy corrections are canceled completely by the counterterms of on-shell renormalization. For a detailed discussion of on-shell renormalization conditions, we refer to [84].

Integrals in D dimensions produce UV poles in $(D-4)$ together with finite terms of the form

$$\Delta = \frac{2}{4-D} - \gamma_E + \log(4\pi)\,, \tag{2.29}$$

where $\gamma_E = 0.57721\ldots$ is the Euler-Mascheroni constant. In the $\overline{\text{MS}}$ scheme, both the UV pole and the finite terms in Eq. (2.29) are subtracted as part of the renormalization procedure. Numerical values of the strong coupling α_s are usually reported in the $\overline{\text{MS}}$ scheme. After renormalization, all UV poles are removed and only IR poles are still present.

2.4.3 FKS Subtraction Method

Subtraction methods add and subtract a term A which is tailored to the IR poles of an NLO calculation in such a way that the sum

$$\begin{aligned} &\int \mathrm{d}\Phi_B\ \hat{V} + \int \mathrm{d}\Phi_R\ R \\ &= \int \mathrm{d}\Phi_B\ \left[\hat{V} + \int \mathrm{d}\Phi_{\text{rad}}\ A\right] + \int \mathrm{d}\Phi_R\ (R - A) \end{aligned} \tag{2.30}$$

of virtual and real-emission contributions is split into two infrared finite integrals. For the construction of A, the infrared poles of the real-emission contribution need to be extracted, which is a highly non-trivial task due to the complexity of the real-emission phase space.

In the subtraction scheme of Frixione, Kunszt and Signer (FKS) [103, 102], the real-emission contribution is split into a sum of independent infrared singular regions which can be integrated separately. This splitting is based on a suitable decomposition of the measurement function $\mathcal{S}_{\text{R}}$ for the real-emission contribution that relates partonic final state configurations to observed signatures like jets. For infrared safe observables, the output of a measurement function in a soft or collinear limit of an $(n+1)$-parton configuration must be identical to the one in an n-parton configuration, where the soft parton is removed or two collinear partons are merged. The real-emission corrections of a Born process with n final state partons have $(n+1)$ final state partons. If more than one parton is removed from a real-emission configuration in multiple infrared limits, there is no contribution of this configuration to the process under consideration, which is realized by a vanishing measurement function. The only non-vanishing multiple infrared limit of the real-emission

contribution in an NLO calculation is the soft-collinear limit, where one parton becomes soft and collinear to another parton at the same time.

Due to this constraint on multiple infrared limits, it is possible to decompose the measurement function for the real-emission contribution into a sum of terms with at most one soft-collinear singularity each. For two incoming partons with four-momenta p_1, p_2 and $n+1$ outgoing partons in the real-emission contribution with four-momenta $p_3, \ldots, p_{n+3}$, this decomposition of the real-emission measurement function $\mathcal{S}_{\mathrm{R}}$ is given by

$$\mathcal{S}_{\mathrm{R}} = \sum_{i=3}^{n+3} \left(\mathcal{S}_i + \sum_{j=i+1}^{n+3} \mathcal{S}_{ij} \right) . \tag{2.31}$$

The functions $\mathcal{S}_i$ are non-zero in the soft and collinear limits $p_i^0 \to 0, \vec{p}_i \parallel \vec{p}_1, \vec{p}_i \parallel \vec{p}_2$ and vanish in all other infrared limits. Similarly, the functions $\mathcal{S}_{ij}$ vanish in all IR limits apart from $p_i^0 \to 0, p_j^0 \to 0, \vec{p}_i \parallel \vec{p}_j$. In the decomposition of Eq. (2.31), only the infrared limits of the functions $\mathcal{S}_i$ and $\mathcal{S}_{ij}$ are essential. It is therefore possible to redefine these functions by the addition of terms which vanish in the corresponding limits. The FKS subtraction method can be applied to processes with an arbitrary number of final state partons. The splitting of IR singular regions via the measurement functions can by accomplished in such a way that it does not depend on a specific jet algorithm.

Chapter 3

Slepton Pair Production at Hadron Colliders

In this chapter, we identify relevant production channels for sleptons in our setup using literature results for the production of sleptons at hadron colliders. Our calculations proceed in the MSSM with conserved R-parity, which implies that supersymmetric particles can only be produced in pairs. Consequently, we restrict the discussion of literature results to investigations of slepton pair production at hadron colliders. After an overview of known results, we describe in detail the various contributions to the NLO SQCD matrix elements for slepton pair production ($pp \to \tilde{\ell}^+\tilde{\ell}^- + X$) and the production of a slepton pair in association with a jet ($pp \to \tilde{\ell}^+\tilde{\ell}^- j + X$).

3.1 Known Results

Slepton pairs have several production channels in hadronic collisions. In a process with the minimal number of interaction vertices, an incoming quark and the corresponding antiquark annihilate into a vector boson which in turn produces the slepton pair as displayed in Fig. 3.1 (a). The structure of this diagram resembles the original Drell-Yan process [89] $q\overline{q} \to \gamma/Z \to e^+e^-$, hence we refer to it as Drell-Yan like. In vector boson fusion, the sleptons are the fusion product of two W bosons of opposite charge that are emitted from incoming quarks or antiquarks. There are different possibilities for the coupling between the W bosons and the sleptons, Fig. 3.1 (b) shows the Feynman diagram with a photon or Z boson as mediator. Gluon fusion proceeds via a fermionic loop that couples to two incoming gluons and a mediator that produces the sleptons, see Fig. 3.1 (c) for one

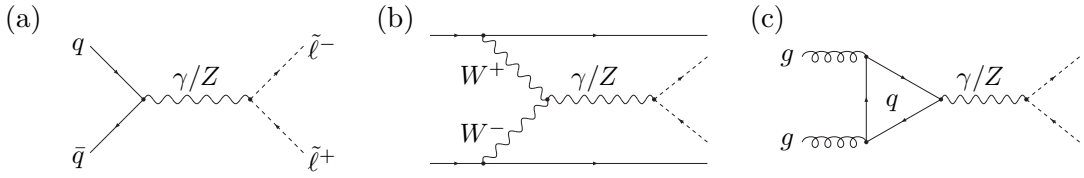

Figure 3.1: Representative Feynman diagrams for slepton pair production in a Drell-Yan like process (a), vector boson fusion (b), and gluon fusion (c).

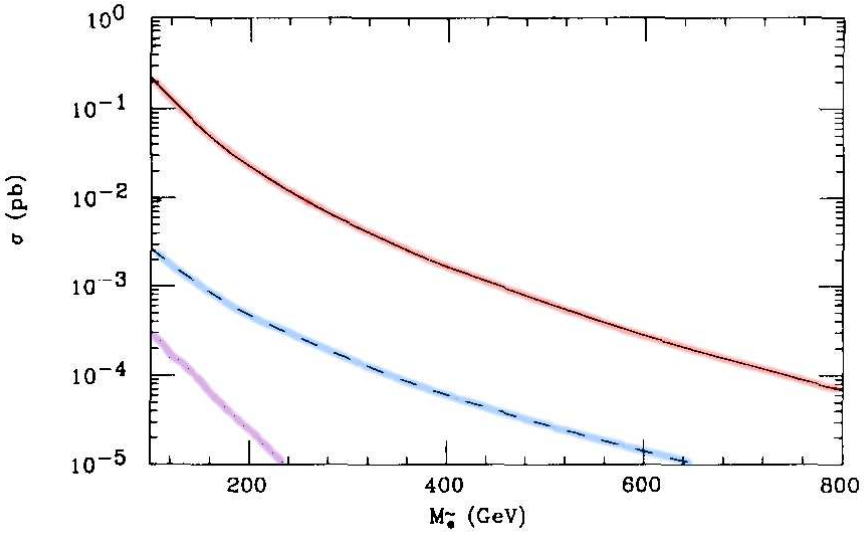

Figure 3.2: Total cross section for the pair production of left-handed selectrons at the LHC as function of the selectron mass for Drell-Yan like production (solid, red), WW fusion (dashed, blue) and gluon fusion (dotted, purple). Figure adapted from [83].

example with an intermediate photon or Z boson. These three production mechanisms for slepton pairs were compared in [83], we reproduce their results in Fig. 3.2. Drell-Yan production, which proceeds at lower orders of the coupling constants than the other two production mechanisms, is found to dominate at the LHC. While gluon fusion is completely negligible [83], vector boson fusion becomes relevant for large slepton masses [126, 83].

We only consider the dominant Drell-Yan production channel and variants thereof, both in the subsequent discussion of theory results from the literature and in our calculations as described in the next two sections. At the level of loop diagrams, additional production modes for the slepton pair need to be considered. Instead of a vector boson, a Higgs boson or a vertex of four supersymmetric particles can produce the sleptons. In this context, we refer to the production via a photon or a Z boson as Drell-Yan like.

Leading order results for slepton pair production with Drell-Yan structure have been calculated [82] and examined at colliders in the TeV energy range [90] already three decades ago. Total cross sections at the LHC lie in the fb range for current slepton mass limits and drop rapidly when the slepton mass grows. Perturbative results for this process were improved by the inclusion of NLO QCD [29] and NLO SQCD [37] corrections. The complete NLO SQCD corrections were implemented in the publicly available computer program `PROSPINO` [38]. At next-to-leading order, the cross section is enhanced up to 35% compared to the leading order result and the dependence on unphysical scales is reduced.

Resummations of enhanced contributions from multiple emissions of soft gluons allow to increase the precision of theoretical calculations in kinematic regions where pure fixed-order calculations become unreliable. Large logarithms of the ratio between the invariant masses of slepton pairs and small transverse momenta have been resummed at next-to-leading logarithmic (NLL) accuracy in [52]. A subsequent investigation [53] performed the NLL resummation of enhanced logarithms for slepton pairs near the production threshold. Both types of soft-gluon resummations were combined in [54] and implemented in the com-

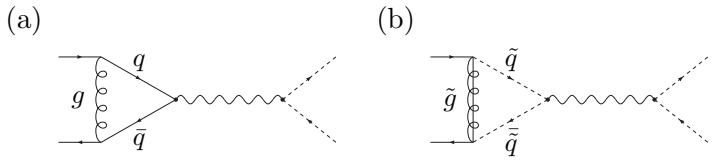

Figure 3.3: One-loop diagrams for slepton pair production.

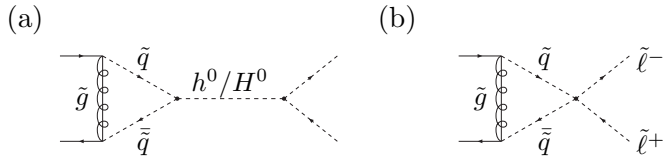

Figure 3.4: Diagrams that do not contribute to the virtual corrections for slepton pair production in a hadron collision at NLO SQCD.

puter program `RESUMMINO` [108], which has been used for a detailed study of resummation effects for slepton pair production in various LHC scenarios [109]. Threshold resummation for slepton pair production has been pushed up to next-to-next-to-next-to-leading logarithmic (NNNLL) accuracy [56] with methods of soft-collinear effective theory (SCET). All resummation calculations find significant reductions of scale uncertainties compared to fixed-order calculations. The total cross section receives only small corrections, but the transverse momentum resummation cures the singular behavior of the fixed order result for small transverse momenta.

Several multi-purpose Monte-Carlo event generators like `HERWIG++` [32], `ISAJET` [188], `PYTHIA` [206], or `SHERPA` [117] are able to simulate slepton pair production in hadron collisions, see [28] for an application to Tevatron and LHC scenarios. Simulated signal events from multi-purpose Monte-Carlo programs are frequently used in experimental slepton searches.

3.2 Slepton Pair Production

At leading order, slepton pair production in a hadronic collision with a Drell-Yan like structure proceeds via the annihilation of a quark and an antiquark into a photon or Z boson, that subsequently produces a slepton pair, see Fig. 3.1 (a). The squared matrix element of this purely electroweak process at order α^2 is suppressed by a smaller coupling factor compared to processes with strong interactions.

Virtual correction diagrams comprise the exchange of a gluon between the incoming quarks and the supersymmetric version of this diagram with squark and gluino superpartners, c.f. Fig. 3.3. These diagrams contribute after interference with the Born diagrams at order $\alpha^2\alpha_s$.

The Feynman rules of the MSSM also allow for virtual correction diagrams, where the vector boson that mediates the interaction between squarks and sleptons in Fig. 3.3 (b) is replaced by a Higgs boson or by a squark-squark-slepton-slepton vertex, see Fig. 3.4. These diagrams do, however, not contribute to the squared matrix element at NLO SQCD for

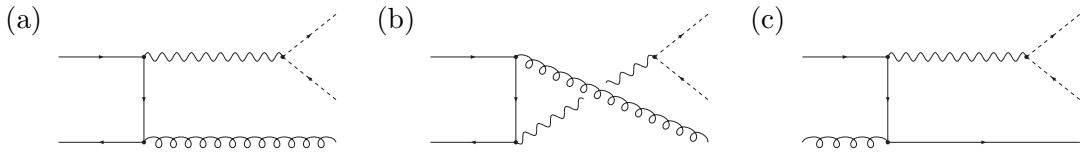

Figure 3.5: Representative real-emission diagrams for slepton pair production.

the following reasons: The loop integral contains two scalars and one fermion, namely the gluino. It is not coupled to vector bosons. Only the gluino momentum q in the propagator numerator $q^\mu \gamma_\mu + m_{\tilde{g}}$ contributes non-trivial Lorentz structure. Consequently, only the loop integrals C_0 and C_μ, that are defined in App. B, are present. Choosing the quark momentum p_1 and the antiquark momentum p_2 as the two independent momenta which enter the loop, we find that the Passarino-Veltman reduction produces terms proportional to p_1^μ or p_2^μ and terms without Lorentz structure. Looking at the resulting spinor chains between antiquark $\overline{v}_2$ and quark u_1, we get three possibilities:

$$(a)\ \overline{v}_2 u_1, \qquad (b)\ \overline{v}_2 \not{p}_1 u_1, \qquad (c)\ \overline{v}_2 \not{p}_2 u_1. \tag{3.1}$$

Spinor chain (a) leads to an odd number of Dirac matrices in the interference with the Born diagrams, so the corresponding trace is zero. Spinor chains (b) and (c) vanish due to the Dirac equation for massless quarks. In the case of slepton pair production in association with a jet, corresponding diagrams with an additional gluon lead to a non-vanishing contribution. The SUSY diagram with an intermediate vector boson in Fig. 3.3 (b) does not vanish, since the coupling of the loop to this vector boson allows for more structures in the Passarino-Veltman decomposition of the integral, including a metric tensor term.

Real-emission diagrams contain an additional parton in the final state. Diagrams where a gluon is emitted by the incoming quark or antiquark, need to be supplemented by crossing related diagrams with the gluon as incoming particle and the quark or the antiquark as outgoing particle. See Fig. 3.5 for representative diagrams. The interference of all real-emission diagrams contributes at order $\alpha^2 \alpha_s$ to the squared matrix element.

3.3 Slepton Pair Plus Jet Production

The real-emission diagrams of slepton pair production shown in Fig. 3.5 become Born diagrams if we look at the production of a slepton pair in association with a jet. Their interference provides the leading contribution to this process at order $\alpha^2 \alpha_s$.

We do not expect large contributions from squarks in this process due to the lower bounds on squark masses of several hundreds of GeV from LHC searches [4, 5] and since our examination of slepton pair production revealed only very small corrections due to diagrams that contain squarks. To test if the diagrams with squarks provide a relevant contribution, we use a simplified setup in which all squarks are assumed to be degenerate in mass. We also restrict ourselves to sleptons of the first two generations and do not consider slepton mixing for this process.

The virtual correction diagrams can be split into one group that exhibits a Drell-Yan like structure and a second group consisting of diagrams with different structures. In

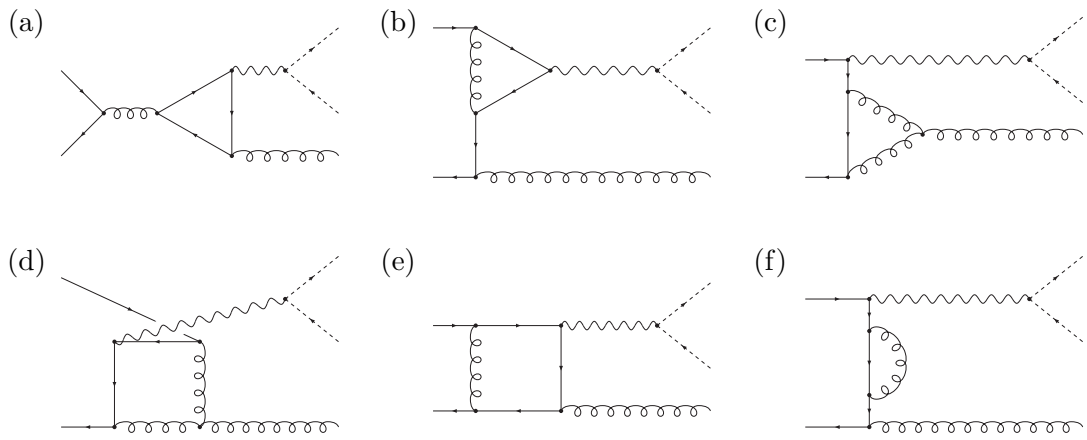

Figure 3.6: Representative virtual correction diagrams with SM Drell-Yan structure for the production of a slepton pair in association with a jet.

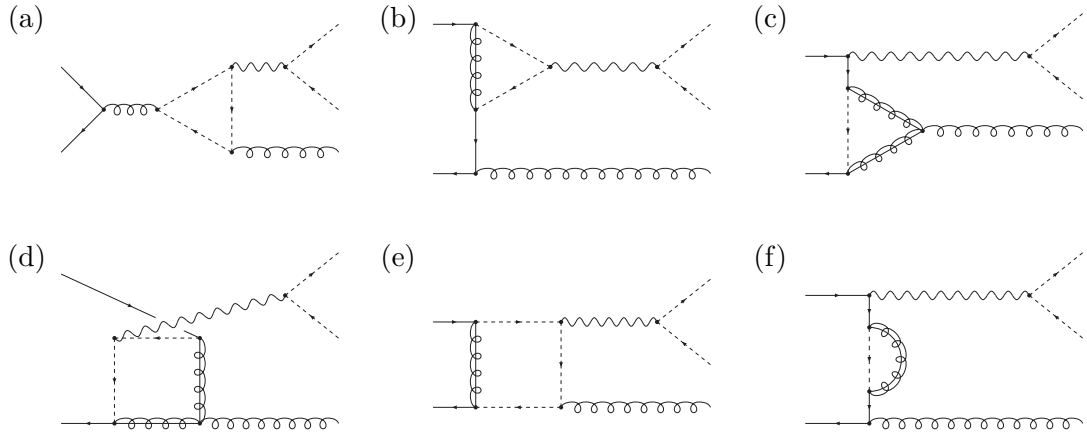

Figure 3.7: Representative virtual correction diagrams with SUSY Drell-Yan structure for the production of a slepton pair in association with a jet.

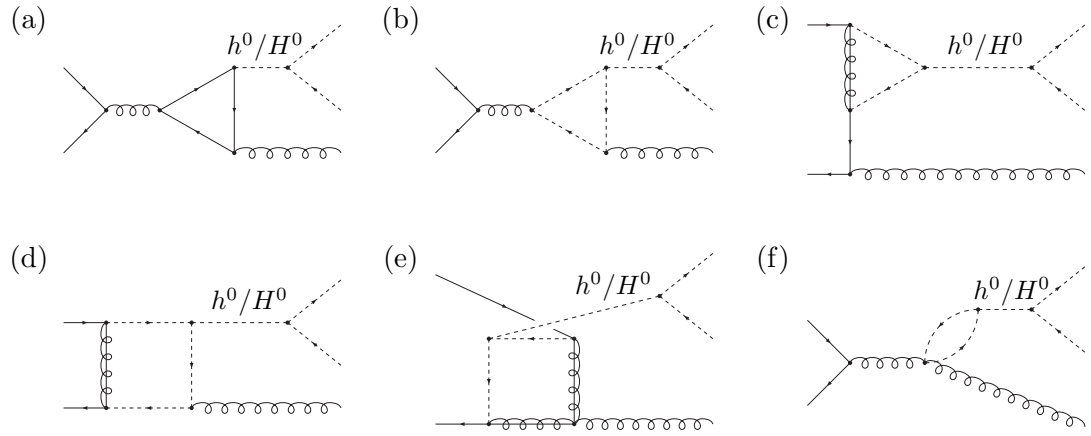

Figure 3.8: Representative virtual correction diagrams with Higgs bosons for the production of a slepton pair in association with a jet.

the first group, each of the diagrams with an intermediate photon or Z boson exists in a QCD version and an SQCD version. Diagrams containing only non-supersymmetric virtual particles are depicted in Fig. 3.6, the corresponding supersymmetric versions are shown in Fig. 3.7. We evaluate these diagrams based on a structural decomposition, which can be applied to any process that contains central structures of the Drell-Yan reaction with an additional jet, as explained in detail in Sec. 4.3.

The second group of virtual corrections features sleptons originating from Higgs or Goldstone bosons or a squark-squark-slepton-slepton vertex. While the corresponding diagrams without a final-state parton vanish, as was shown in the previous section, this is no longer the case when the emission of one parton is included in the loop diagrams. Since we neglect slepton mixing, only the diagrams with CP even neutral Higgs bosons h^0 and H^0, which are shown in Fig. 3.8, give rise to non-vanishing contributions among the diagrams with Higgs or Goldstone bosons. Diagrams in which the sleptons are produced in a squark-squark-slepton-slepton vertex (Fig. 3.9) have structures that correspond to the contraction of the intermediate boson propagator to a point for specific SUSY Drell-Yan (Fig. 3.7) or Higgs (Fig. 3.8) diagrams. All virtual diagrams and the corresponding crossing related diagrams contribute after interference with the Born diagrams at order $\alpha^2\alpha_s^2$.

Real-emission diagrams can be split into three groups. Diagrams with one fermionic line and two external gluons are shown in Fig. 3.10. These diagrams include contributions with purely gluonic initial states, see Fig. 3.10 (c), which can be important due to the high gluon luminosities at the LHC. The other diagrams contain two fermionic lines, which can belong to identical or different quark flavors, as displayed in Fig. 3.11. All of these diagrams and all crossing related diagrams contribute after squaring at order $\alpha^2\alpha_s^2$.

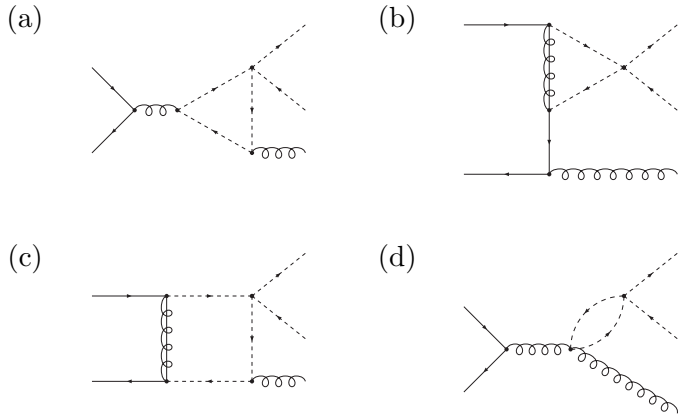

Figure 3.9: Representative virtual correction diagrams with a squark-squark-slepton-slepton vertex for the production of a slepton pair in association with a jet.

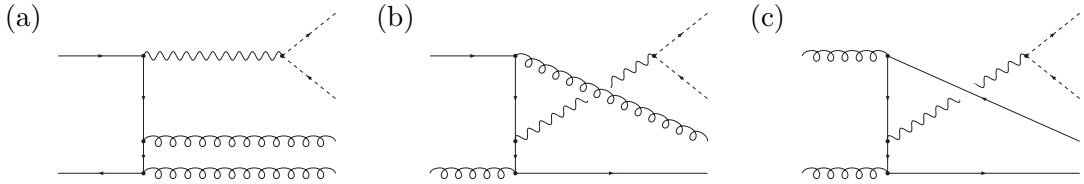

Figure 3.10: Representative real-emission diagrams for slepton pair production in association with a jet containing one fermionic line and two gluons.

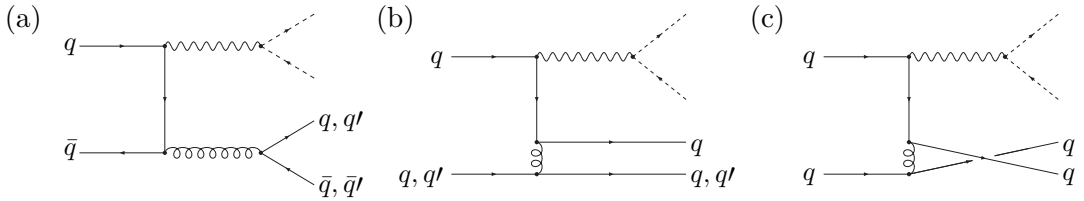

Figure 3.11: Representative real-emission diagrams for slepton pair production in association with a jet containing two fermionic lines, where the quarks can have the same flavor or different flavors on both lines (a), (b) and one additional diagram for quarks of the same flavor (c).

Chapter 4

Details of the NLO Calculations

Several aspects of our matrix element calculations at next-to-leading order in SQCD are discussed in this chapter. We begin with a description of the respective renormalization procedures for slepton pair production and for slepton pair production in association with a jet. Subsequently, we explain the method that we choose for a consistent evaluation of fermionic traces in D dimensions which include the matrix γ_5. In the last section, we derive a structural decomposition that is applied to the real-emission corrections of $pp \to \tilde{\ell}^+\tilde{\ell}^- + X$ and to the virtual corrections of $pp \to \tilde{\ell}^+\tilde{\ell}^- j + X$ for the generation of efficient code in both cases.

4.1 Renormalization

Slepton pair production at leading order is a purely electroweak process. The only component that requires a renormalization at next-to-leading order in SQCD is the quark wavefunction. When an additional gluon is included at Born level for the production of a slepton pair in association with a jet, also the gluon wavefunction and the strong coupling require renormalization. There is no need for quark mass renormalization, since we regard all quarks in the Born diagrams of both processes as massless.

We use multiplicative renormalization, i.e. we multiply each field or coupling in the Lagrangian that requires renormalization by a factor as specified in Tab. 4.1, expand the factor in powers of α_s and determine the coefficient of $(\alpha_s)^1$ from the cancelation of UV divergences and appropriate renormalization conditions for the finite part. For quark and gluon wavefunctions, we use on-shell renormalization, whereas the strong coupling is renormalized in a modified version of the $\overline{\text{MS}}$ scheme, that is described in detail below. Our evaluation of self-energy and vertex-correction diagrams for the determination of the renormalization constants is based on `FeynArts 3.6` [131] and `FormCalc 7.1` [134, 132].

name	symbol	renormalization factor
left-handed quark wavefunction	ψ_L	$\sqrt{Z_L} = 1 + \frac{1}{2}\delta Z_L + \mathcal{O}\left(\alpha_s^2\right)$
right-handed quark wavefunction	ψ_R	$\sqrt{Z_R} = 1 + \frac{1}{2}\delta Z_R + \mathcal{O}\left(\alpha_s^2\right)$
gluon wavefunction	G_μ^a	$\sqrt{Z_3} = 1 + \frac{1}{2}\delta Z_3 + \mathcal{O}\left(\alpha_s^2\right)$
strong coupling	g_s	$Z_g = 1 + \delta Z_g + \mathcal{O}\left(\alpha_s^2\right)$

Table 4.1: Fields, couplings and renormalization factors.

Figure 4.1: Counterterm diagram for slepton pair production.

4.1.1 Slepton Pair Production

UV divergences in the virtual correction diagrams for slepton pair production, that are shown in Fig. 3.3, cancel in the sum with the counterterm diagram of Fig. 4.1. This diagram depicts the product of the Born diagram with appropriate renormalization constants for left-handed and right-handed quarks respectively.

The quark wavefunction renormalization constants can be determined with the quark self-energy diagrams depicted in Fig. 4.2. We give results for the on-shell renormalization constants using the integral B_1 of the Passarino-Veltman decomposition as defined in App. B. Both left-handed and right-handed quarks have a common QCD part of the wavefunction renormalization constant. In the on-shell scheme, its value is

$$\delta Z_{L,R}^{\mathrm{SM}} = \frac{\alpha_s}{3\pi}(D-2)\; B_1\left(0,0,0\right). \tag{4.1}$$

This term vanishes unless UV and IR poles are distinguished. The supersymmetric QCD parts of the renormalization constants depend on the mixing between the squark interaction eigenstates $\tilde{q}_L, \tilde{q}_R$, partner states of quarks with chiralities $C = L, R$, and the mass eigenstates $\tilde{q}_1, \tilde{q}_2$. This mixing is described by a unitary mixing matrix M_{jC} according to:

$$\begin{pmatrix} \tilde{q}_1 \\ \tilde{q}_2 \end{pmatrix} = \begin{pmatrix} M_{1L} & M_{1R} \\ M_{2L} & M_{2R} \end{pmatrix} \begin{pmatrix} \tilde{q}_L \\ \tilde{q}_R \end{pmatrix}. \tag{4.2}$$

For a quark with chirality $C = L$ or $C = R$, the SQCD part of the quark wavefunction renormalization constant in the on-shell scheme is

$$\delta Z_C^{\mathrm{SUSY}} = \frac{2\alpha_s}{3\pi} \sum_{j=1,2} |M_{jC}|^2 \; B_1\left(0, m_{\tilde{g}}^2, m_{\tilde{q}_j}^2\right). \tag{4.3}$$

Our results for the quark wavefunction renormalization constants are in agreement with a second independent calculation [220].

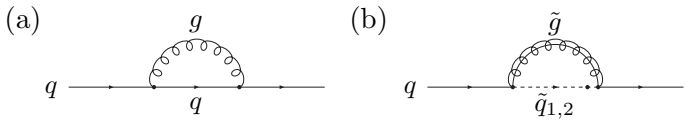

Figure 4.2: Quark self-energy diagram in QCD (a) and additional diagrams in supersymmetric QCD (b).

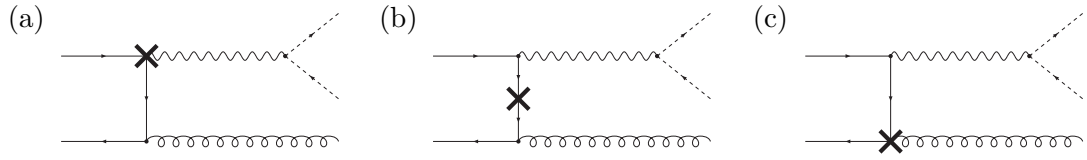

Figure 4.3: Representative counterterm diagrams for slepton pair production in association with a jet.

4.1.2 Slepton Pair Plus Jet Production

Three counterterm diagrams (and crossing related diagrams) need to be considered for slepton pair production in association with a jet, they are shown in Fig. 4.3. The sum of the counterterms which correspond to Fig. 4.3 (a) and (b) vanishes, hence only the third counterterm diagram in Fig. 4.3 (c) must be evaluated. This diagram for the renormalization of the quark-gluon vertex depends on the renormalization constants of both quark and gluon wavefunctions as well as on the renormalization constant for the strong coupling.

While quark and gluon wavefunctions are renormalized according to conventional on-shell conditions in our calculations, a specific renormalization condition is chosen for the strong coupling. In order to make our renormalization compatible with the running of the strong coupling in the five flavor scheme that is used in the `POWHEG BOX`, we decouple the top quark [77] and heavy SUSY particles [44] from the running of α_s. This decoupling is accomplished by modifying the $\overline{\text{MS}}$ renormalization condition for the strong coupling via the subtraction of all logarithms of heavy particle masses which are required to achieve a complete cancelation between the heavy particle contributions to δZ_g and δZ_3.

In principle, the gluon wavefunction renormalization constant δZ_3 can be determined from gluon self-energy diagrams in QCD and SQCD, as shown in Fig. 4.4. However, the contribution of massless virtual particles vanishes in the on-shell scheme due to the cancelation of UV and IR poles. The remaining contributions of massive particles cancel in the combination of δZ_3 and δZ_g as a consequence of our decoupling scheme. Hence, an explicit evaluation of the on-shell gluon wavefunction renormalization constant is not necessary.

Next, we look at the strong coupling renormalization constant δZ_g. With the cancelation of heavy particle contributions in mind, it is only necessary to evaluate the part of δZ_g which is generated by massless virtual particles. To determine this part of δZ_g in the $\overline{\text{MS}}$ scheme, we first evaluate the $\overline{\text{MS}}$ result for the corresponding part of the gluon wavefunction renormalization constant δZ_3 based on the gluon self-energy diagrams with massless virtual particles in Fig. 4.4. Since we use the Feynman-'t Hooft gauge in our calculations, we need to consider Faddeev-Popov ghosts gh [95] as virtual particles in these self-energy diagrams.

Subsequently, we use the result for δZ_3 in $\overline{\text{MS}}$ renormalization and the one-loop corrections of the three-gluon vertex from massless particles in QCD, c.f. Fig. 4.5, to extract δZ_g. The contribution of light SM particles, among them $n_f = 5$ massless quark flavors,

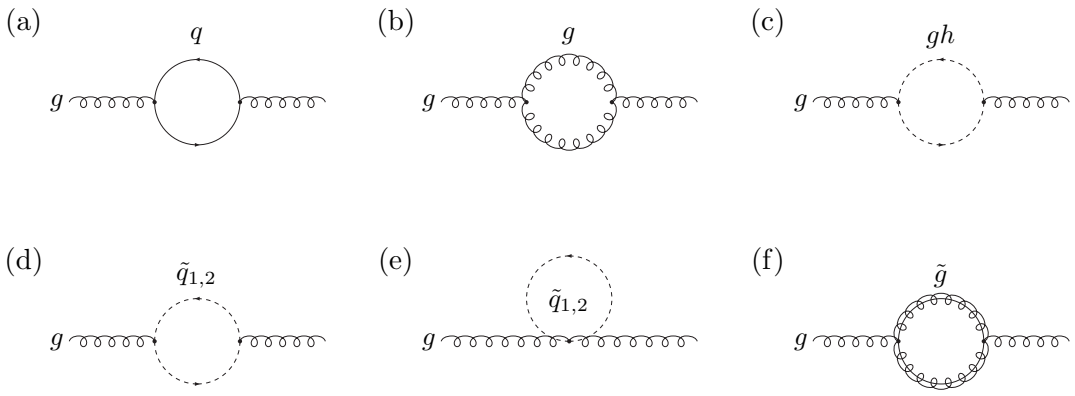

Figure 4.4: Gluon self-energy diagrams in QCD (a)-(c) and additional diagrams in SQCD (d)-(f).

to δZ_g is given by

$$\delta Z_g^{\text{SM,light}} = -\frac{\alpha_s}{8\pi}\left(11 - \frac{2}{3}n_f\right)\Delta, \tag{4.4}$$

which is in agreement with a second independent calculation [220] and with the results for δZ_g of Refs. [110] and [189]. Here, Δ denotes the sum of a UV divergence and associated finite terms, which is subtracted in the $\overline{\text{MS}}$ scheme, as specified in Eq. (2.29).

It should also be noted that there are no counterterm diagrams for the virtual correction diagrams with an intermediate Higgs boson in Fig. 3.8 and for those with a squark-squark-slepton-slepton vertex in Fig. 3.9. Such counterterm diagrams cannot exist since there are no corresponding Born diagrams, where the sleptons are produced in the same vertex as in the loop diagrams, in our setup. Consequently, the sum of all UV divergences in these diagrams has to vanish, which we confirm in an explicit calculation.

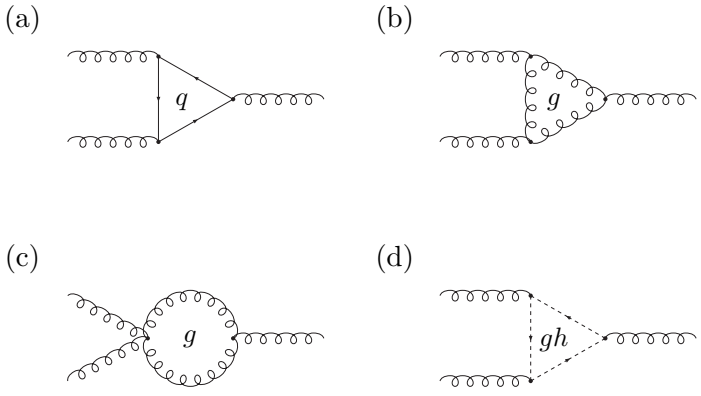

Figure 4.5: Representative one-loop corrections of the three-gluon vertex in QCD.

4.2 Traces with γ_5

Closed fermionic lines in single Feynman diagrams or in the interference of Feynman diagrams yield traces over Dirac matrices γ^μ and, in the presence of axial couplings, the matrix γ_5. In our calculations, axial couplings arise in the interaction of fermions with the Z boson.

Traces involving γ_5 need to be handled with great care in D dimensions, since there is no straightforward generalization of the four-dimensional object

$$\gamma_5 = -\frac{i}{4!}\varepsilon_{\mu\nu\rho\sigma}\gamma^\mu\gamma^\nu\gamma^\rho\gamma^\sigma \tag{4.5}$$

to an arbitrary number of dimensions. We illustrate the conflict between different properties of the four-dimensional matrix γ_5 in an extension to D dimensions by the example of a trace with four Dirac matrices and one γ_5. In four dimensions, this trace can be evaluated with formula (4.5) for γ_5 as

$$\mathrm{Tr}\left[\gamma^\mu\gamma^\nu\gamma^\rho\gamma^\sigma\gamma_5\right] = -4i\varepsilon^{\mu\nu\rho\sigma}. \tag{4.6}$$

A convenient property of γ_5 in four dimensions is the anticommutativity with respect to all Dirac matrices, i.e.

$$\{\gamma^\mu,\gamma_5\} = 0, \qquad \mu = 0,1,2,3. \tag{4.7}$$

Assuming this property to hold also in an arbitrary number D of dimensions together with the usual anticommutation relation $\{\gamma^\mu,\gamma^\nu\} = 2g^{\mu\nu}$ and the invariance of traces over gamma matrices under cyclic permutations, it is possible to derive

$$(D-4)\,\mathrm{Tr}\left[\gamma^\mu\gamma^\nu\gamma^\rho\gamma^\sigma\gamma_5\right] = 0. \tag{4.8}$$

This result implies that the trace $\mathrm{Tr}\left[\gamma^\mu\gamma^\nu\gamma^\rho\gamma^\sigma\gamma_5\right]$ must vanish for $D \neq 4$, which does not allow for a continuous extrapolation to the four-dimensional result of Eq. (4.6).

There are several schemes in the literature that suggest different ways to deal with this issue. We use the scheme of Dirk Kreimer [160, 158, 161], which has the following basic features:

- γ_5 anticommutes with all Dirac matrices γ^μ, i.e. $\{\gamma_5,\gamma^\mu\} = 0$.
- Traces involving γ_5 are not cyclical.
- The product of two γ_5 matrices is the identity matrix in four-spinor space, i.e. $\gamma_5\gamma_5 = \mathbb{1}$.

This scheme has several advantages. For example, it is not necessary to split Dirac matrices into 4-dimensional and $(D-4)$-dimensional parts, the anticommutativity of γ_5 allows simple manipulations of spinor chains, and there is no need to add symmetry-restoring terms.

To evaluate traces without γ_5 matrices, all standard anticommutation, contraction, and cyclicality rules of Dirac matrices and fermionic traces in dimensional regularization can be used. In traces with an even number of γ_5 matrices, the anticommutativity of γ_5 and $\gamma_5\gamma_5 = \mathbb{1}$ can be used to eliminate all γ_5 matrices. Subsequently, the evaluation proceeds via the transformations for traces without γ_5, as outlined above. The evaluation of traces involving an odd number of γ_5 matrices proceeds as follows:

- $\gamma_5\gamma_5 = \mathbb{1}$ eliminates all but one of the γ_5 matrices.
- The vanishing anticommutator of γ_5 with all Dirac matrices is used to transport the only remaining γ_5 matrix to the left end of the trace.
- γ_5 is replaced by $-\frac{i}{4!}\varepsilon_{\mu\nu\rho\sigma}\gamma^\mu\gamma^\nu\gamma^\rho\gamma^\sigma$, where the Levi-Civita tensor is treated as purely four-dimensional object.
- The trace of Dirac matrices is evaluated according to standard methods.

Special attention is necessary for the starting point of non-cyclical traces. In our case, we choose for example the spinor of the incoming quark as starting point of the associated trace throughout all diagrams. In general, processes with several axial vertices at the same fermionic line require a symmetrized choice of starting points, see Ref. [161] for details. The lack of invariance under cyclic permutations is relevant for traces of at least six Dirac matrices and one γ_5. In explicit form, the non-vanishing difference for a minimal example is given by

$$\begin{aligned}
&\mathrm{Tr}\left[\gamma_5\gamma^{\mu_1}\gamma^{\mu_2}\gamma^{\mu_3}\gamma^{\mu_4}\gamma^{\mu_5}\gamma^{\mu_6}\right] - \mathrm{Tr}\left[\gamma^{\mu_6}\gamma_5\gamma^{\mu_1}\gamma^{\mu_2}\gamma^{\mu_3}\gamma^{\mu_4}\gamma^{\mu_5}\right] \\
&= 8i\left(g^{\mu_1\mu_6}\varepsilon^{\mu_2\mu_3\mu_4\mu_5} - g^{\mu_2\mu_6}\varepsilon^{\mu_1\mu_3\mu_4\mu_5} + g^{\mu_3\mu_6}\varepsilon^{\mu_1\mu_2\mu_4\mu_5}\right. \\
&\quad \left. - g^{\mu_4\mu_6}\varepsilon^{\mu_1\mu_2\mu_3\mu_5} + g^{\mu_5\mu_6}\varepsilon^{\mu_1\mu_2\mu_3\mu_4}\right). \qquad (4.9)
\end{aligned}$$

The contraction of this difference with e.g. $g_{\mu_1\mu_6}$ is

$$8i(D-4)\varepsilon^{\mu_2\mu_3\mu_4\mu_5}, \qquad (4.10)$$

which would generate, in combination with poles in $(D-4)$, non-vanishing terms in the limit $D \to 4$.

We compare our results obtained in the non-cyclical scheme with two independent calculations [220]. One of these uses the same scheme for γ_5 as our calculation, the other one is based on the scheme suggested by Larin [164]. In this scheme, definition (4.5) for γ_5 is also used in D dimensions. The Dirac matrices in this definition are treated as D-dimensional objects, whereas the Levi-Civita tensor is kept in four dimensions. Symmetry relations need to be restored in this scheme explicitly by adding finite terms. Both independent calculations are in complete agreement with our matrix elements.

4.3 Structural Decomposition

The complexity of algebraic expressions for the amplitudes of Feynman diagrams grows rapidly with the number of loops and external legs in the diagrams. However, many terms are found to cancel in the combination of diagrams when they are arranged in a suitable way. Compact expressions for the squared matrix elements are crucial for numerical phase space integration, where the matrix elements are evaluated thousands or millions of times.

When very complex terms are combined, subsequent simplifications by algebraic manipulations based on trial and error become prohibitive. Instead, specific methods are necessary to extract the essential information out of the Feynman diagrams. One of these methods, which we choose for our implementations of the real-emission corrections to $pp \to \tilde{\ell}^+\tilde{\ell}^- + X$ and the virtual corrections to $pp \to \tilde{\ell}^+\tilde{\ell}^- j + X$, is the projection onto independent structures in the amplitudes. After a decomposition of color, Lorentz, and Dirac structures for a given process, relations that are based e.g. on gauge invariance can

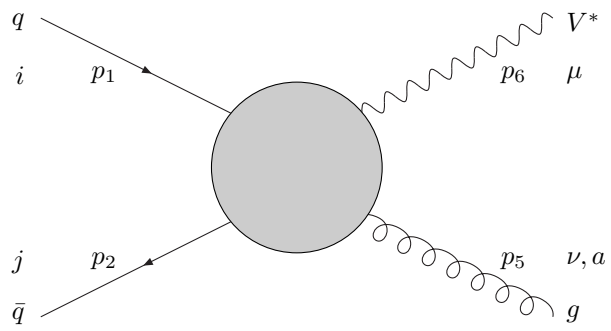

Figure 4.6: Setup of our structural decomposition.

be used to express dependent structures in terms of independent ones. By a projection onto the independent structures, redundant parts of the amplitude are removed.

To capture the relevant structures for this procedure, we look at all color, Lorentz, and Dirac structures that can relate a given set of external particles without reference to a certain order of perturbation theory. Specifically, we use a decomposition of the process

$$q\overline{q} \to V^* g, \tag{4.11}$$

where V^* can be an off-shell photon or Z-boson, to obtain compact results for contributions of Drell-Yan like structures both in the real-emission corrections for slepton pair production and in the virtual corrections for the production of a slepton pair in association with a jet. The setup for this decomposition is displayed in Fig. 4.6. An incoming quark q with momentum p_1, fundamental color index i, and an incoming antiquark $\overline{q}$ with momentum p_2, antifundamental color index j, are connected by an arbitrary diagrammatic structure to an outgoing vector boson V^* with off-shell momentum p_6, Lorentz index μ, and an outgoing gluon g with momentum p_5, Lorentz index ν, adjoint color index a. Spinor indices are not explicitly shown, they are determined and automatically summed according to the order in which spinorial objects are arranged.

The general tensorial structure, which connects the external particles, is called $\Omega^{\mu\nu a}{}_{ij}$. We determine all structures that can appear inside this tensor, restrict them by known identities and obtain projectors that allow to reduce the expressions obtained from Feynman diagrams to few basic structures.

4.3.1 Color Decomposition

First, we consider the color structure of $\Omega^{\mu\nu a}{}_{ij}$. Structures associated with the color symmetry group $\mathrm{SU}(3)_C$ enter the Feynman rules in terms of $\mathrm{SU}(3)_C$ generator matrices T^b_{kl} and structure constants f^{bcd}. Generators and structure constants are related by the defining equation

$$\left[T^b, T^c\right] = i f^{bcd} T^d \tag{4.12}$$

of the generator Lie algebra. Equation (4.12) and the identity $\mathrm{Tr}\left[T^c T^d\right] = \frac{1}{2}\delta^{cd}$ can be used to express the structure constants in terms of generators according to

$$f^{bcd} = 2i\,\mathrm{Tr}\left[T^c T^b T^d - T^b T^c T^d\right]. \tag{4.13}$$

Hence, it is possible to express the complete color structure in terms of generator matrices.

There is only one free adjoint index in $\Omega^{\mu\nu a}{}_{ij}$. Consequently all but one of the generator matrices in each term of the color structure must be contracted over their adjoint index. Contractions of two generators over adjoint indices can be replaced by Kronecker deltas according to [81],

$$T^b_{kl} T^b_{mn} = 2\delta_{kn}\delta_{lm} - \frac{2}{3}\delta_{kl}\delta_{mn}. \tag{4.14}$$

When these Kronecker deltas are used to eliminate contracted fundamental and antifundamental indices, a non-vanishing result can only be found if both the free fundamental index i and the free antifundamental index j belong to the generator with the free adjoint index a, since the generators are traceless. All in all, there is only one possibility for the color structure of $\Omega^{\mu\nu a}{}_{ij}$. It is given by a single T^a_{ij}, which can be factored out according to

$$\Omega^{\mu\nu a}{}_{ij} = \Gamma^{\mu\nu} T^a_{ij}. \tag{4.15}$$

4.3.2 Lorentz and Dirac Decomposition

The next step in our structural analysis comprises the decomposition of $\Gamma^{\mu\nu}$ into possible Lorentz and Dirac structures, i.e. into all objects that carry bosonic or fermionic degrees of freedom. While the Lorentz indices are shown explicitly, we suppress the spinor indices of $\Gamma^{\mu\nu}$. The Dirac structure is encoded in the order of matrices with spinor indices inside the fermionic line between quark and antiquark spinors. This fermionic line can contain γ_5, but, since we work with anticommuting γ_5, it is possible to anticommute it to one end of the spinor chain and absorb it into the external spinor. Consequently, it is not necessary to consider γ_5 as possible building block of $\Gamma^{\mu\nu}$. All structures involving γ_5 can be obtained when chiral spinors are attached to $\Gamma^{\mu\nu}$.

Let us begin by listing all possible objects that can be part of $\Gamma^{\mu\nu}$. The external particles in Fig. 4.6 have the four-momenta $p_1^\rho, p_2^\rho, p_5^\rho, p_6^\rho$. Four-momentum conservation allows to replace the vector boson four-momentum p_6^ρ in terms of the other external momenta. Dirac matrices γ^ρ can be part of the spinor chain, and, since there are two free Lorentz indices, the metric tensor $g^{\rho\sigma}$ can be part of $\Gamma^{\mu\nu}$. In summary, all building blocks for the Lorentz and Dirac structure of $\Gamma^{\mu\nu}$ are

$$p_1^\rho,\ p_2^\rho,\ p_5^\rho,\ \gamma^\rho,\ g^{\rho\sigma}. \tag{4.16}$$

We determine all structures inside $\Gamma^{\mu\nu}$ that can be composed using these objects. In general, the order of Dirac matrices is relevant, but since two structures that differ only in the order of Dirac matrices are related by the anticommutator of Dirac matrices up to terms with less Dirac matrices, it is sufficient to consider only one order of Dirac matrices in the following cases to find all independent structures. We group the combined Lorentz and Dirac structures according to the number of Dirac matrices that occur. Subgroups are formed on the basis of the free Lorentz indices of the Dirac matrices.

0 (no Dirac matrices)
In this case, the Dirac structure is trivial and we need to look for all possible Lorentz structures. Due to the transversality of the external gluon, $p_5^\nu \varepsilon_\nu(p_5) = 0$, terms with p_5^ν vanish and we obtain the composite structures

$$p_1^\mu p_1^\nu,\ p_1^\mu p_2^\nu,\ p_2^\mu p_1^\nu,\ p_2^\mu p_2^\nu,\ p_5^\mu p_1^\nu,\ p_5^\mu p_2^\nu,\ g^{\mu\nu}. \tag{4.17}$$

1a (one Dirac matrix with free Lorentz index)
One of the two free Lorentz indices of $\Gamma^{\mu\nu}$ resides at the Dirac matrix. This allows the following combinations

$$p_1^\mu \gamma^\nu,\ p_2^\mu \gamma^\nu,\ p_5^\mu \gamma^\nu,\ \gamma^\mu p_1^\nu,\ \gamma^\mu p_2^\nu, \tag{4.18}$$

where we did not include $\gamma^\mu p_5^\nu$ because of gluon transversality.

1b (one Dirac matrix with contracted Lorentz index)
The Lorentz index of the Dirac matrix can be contracted with any external momentum, but we already exclude $\not{p}_1$ and $\not{p}_2$, since they vanish in combination with the spinors of massless quarks and antiquarks according to the Dirac equation. This leaves $\not{p}_5$ as only contraction, which needs to be combined with factors containing the complete Lorentz structure, i.e. the allowed structures are

$$\not{p}_5 \text{combined with all terms in (4.17).} \tag{4.19}$$

2a (two Dirac matrices with two free Lorentz indices)
With two free Lorentz indices, the Dirac matrices carry not only the Dirac structure, but also the complete Lorentz structure. The only structure for this case is

$$\gamma^\mu \gamma^\nu. \tag{4.20}$$

2b (two Dirac matrices with one free Lorentz index)
Based on the same arguments that were used for the structures of group 1b, only $\not{p}_5$ can be the result of the contraction. The Lorentz structure is supplemented by the terms of group 1a, so we obtain

$$\not{p}_5 \text{combined with all terms in (4.18).} \tag{4.21}$$

There is no contribution by terms with contracted Lorentz indices at both Dirac matrices for the following reasons: If one Dirac matrix is contracted with the quark or antiquark momentum, the combination with the quark or antiquark spinor vanishes according to the Dirac equation. If no Dirac matrix is contracted with the quark or antiquark momentum, both of them must be contracted with the gluon momentum and the resulting term is $\not{p}_5 \not{p}_5 = (p_5)^2 = 0$.

3 (three Dirac matrices with two free Lorentz indices)
Only if two out of three Dirac Matrices have free Lorentz indices, there is a non-vanishing structure. If at least two Dirac Matrices are contracted (which is always the case for 4 or more Dirac matrices in total), the corresponding terms vanish due to the reasons described above. The only non-vanishing contraction $\not{p}_5$ combined with γ^μ and γ^ν forms the last structure

$$\gamma^\mu \gamma^\nu \not{p}_5. \tag{4.22}$$

4.3.3 Combination with External Particles

We define H^μ as the combination of $\Gamma^{\mu\nu}$ with the quark and antiquark spinors and the gluon polarization vector according to

$$H^\mu = \overline{v}\left(p_2\right)\Gamma^{\mu\nu}u\left(p_1\right)\varepsilon_\nu\left(p_5\right). \tag{4.23}$$

Based on the structures allowed in $\Gamma^{\mu\nu}$, that are listed in Sec. 4.3.2, we can write down the general form of H^μ as a linear combination of 26 structures with arbitrary coefficients:

$$\begin{aligned}
H^\mu = \overline{v}u\,&\left[e_{11}p_1^\mu\left(p_1\cdot\varepsilon_5\right) + e_{12}p_2^\mu\left(p_1\cdot\varepsilon_5\right) + e_{15}p_5^\mu\left(p_1\cdot\varepsilon_5\right)\right.\\
&\quad\left. + e_{21}p_1^\mu\left(p_2\cdot\varepsilon_5\right) + e_{22}p_2^\mu\left(p_2\cdot\varepsilon_5\right) + e_{25}p_5^\mu\left(p_2\cdot\varepsilon_5\right) + e_{00}\varepsilon^\mu\left(p_5\right)\right]\\
&+ \overline{v}\gamma^\mu u\left[b_1\left(p_1\cdot\varepsilon_5\right) + b_2\left(p_2\cdot\varepsilon_5\right)\right]\\
&+ \overline{v}\not{\varepsilon}_5 u\left[c_1p_1^\mu + c_2p_2^\mu + c_5p_5^\mu\right]\\
&+ \overline{v}\not{p}_5 u\left[a_{11}p_1^\mu\left(p_1\cdot\varepsilon_5\right) + a_{12}p_2^\mu\left(p_1\cdot\varepsilon_5\right) + a_{15}p_5^\mu\left(p_1\cdot\varepsilon_5\right)\right.\\
&\quad\left. + a_{21}p_1^\mu\left(p_2\cdot\varepsilon_5\right) + a_{22}p_2^\mu\left(p_2\cdot\varepsilon_5\right) + a_{25}p_5^\mu\left(p_2\cdot\varepsilon_5\right) + a_{00}\varepsilon^\mu\left(p_5\right)\right]\\
&+ \overline{v}\gamma^\mu\not{\varepsilon}_5 u\left[f\right]\\
&+ \overline{v}\gamma^\mu\not{p}_5 u\left[g_1\left(p_1\cdot\varepsilon_5\right) + g_2\left(p_2\cdot\varepsilon_5\right)\right]\\
&+ \overline{v}\not{\varepsilon}_5\not{p}_5 u\left[h_1p_1^\mu + h_2p_2^\mu + h_5p_5^\mu\right]\\
&+ \overline{v}\gamma^\mu\not{\varepsilon}_5\not{p}_5 u\left[d\right].
\end{aligned} \tag{4.24}$$

Not all of the coefficients $a_{00},\ldots,h_5$ are independent, they are restricted by relations based on the QCD Ward identity and conservation of the hadronic current. As a consequence of the Ward identity, H^μ must vanish when the gluon polarization vector ε_5 is replaced by the gluon momentum p_5. Hadron current conservation tells us that the contraction of H^μ with the vector boson momentum p_6 vanishes. Both identities result in systems of linear equations for the coefficients in H^μ. All in all, 12 out of the 26 coefficients can be eliminated in terms of other coefficients and scalar products of external momenta.

Based on this decomposition, projectors on the independent structures can be constructed. They eliminate redundancies from amplitudes that were generated with Feynman diagrams. Both for the real-emission contribution of slepton pair production and for the virtual corrections of slepton pair production in association with a jet that match the structure of Fig. 4.6, the respective projectors are constructed and applied [220]. We use the resulting compact code for the implementation of the corresponding matrix elements in the `POWHEG BOX`.

Chapter 5

Software Implementations

5.1 POWHEG BOX

The `POWHEG BOX` [16] is a framework for parton shower matching according to the `POWHEG` method that provides the foundation of our codes for $pp \to \tilde{\ell}^+\tilde{\ell}^- + X$ and $pp \to \tilde{\ell}^+\tilde{\ell}^- j + X$. It is available as source code from the project web page

`http://powhegbox.mib.infn.it/`

The original `POWHEG BOX` includes

- routines for the separation of singular regions in the real-emission contribution, as required by the `POWHEG` approach, based on the FKS [103, 102] method with corresponding subtraction terms,
- Monte-Carlo tools [181] for the integration of functions on multi-dimensional unit cubes,
- the creation of event files complying with the Les Houches Interface for User Processes (LHIUP) [50], a standard for input to multi-purpose Monte-Carlo programs,
- templates for an interface to the multi-purpose Monte-Carlo programs `HERWIG` and `PYTHIA` as well as the corresponding source files,
- basic analysis routines that can be easily customized.

Users who want to add new processes need to implement

- lists of all particle flavors for Born and real-emission configurations,
- a mapping of the unit cube with the appropriate number of dimensions to the Born phase space,
- the modulus squared of the Born amplitude together with corresponding spin and color correlations,
- the finite part of the interference between Born and virtual diagrams,
- the modulus squared of the real-emission amplitude,
- the color structure at Born level in the leading color approximation.

One feature which is of special relevance for our implementation of $pp \to \tilde{\ell}^+\tilde{\ell}^- j + X$ is the interface to the program `MadGraph4` [210, 24] for the calculation of tree-level matrix elements that was published in [62]. This interface can be used to obtain in an automatized way the squared moduli of Born and real-emission amplitudes, as well as the corresponding Born spin and color correlations and the leading color approximation of the Born color structure. `MadGraph4` is equipped with model files for several models, e.g. the SM, the MSSM, and the two Higgs doublet model. While Standard Model calculations at tree level are fully automatized through the new interface, specific adjustments in the interplay of `MadGraph4` and `POWHEG BOX` routines can be necessary in extended models. The `MadGraph` interface reduces the main tasks for the implementation of new `POWHEG BOX` processes to the specification of the Born phase space and the calculation of the virtual corrections.

Over time, several extensions of the original `POWHEG BOX` brought new features and improvements that are collected in a new release, which is also available at the project web page. Where distinction between the original version and the updated version of the `POWHEG BOX` is necessary, we refer to the former as `POWHEG BOX V1` and to the latter as `POWHEG BOX V2`. Notable improvements [63] in the `POWHEG BOX V2` include parallelization in the generation of importance sampling grids, a better association of real-emission configurations with underlying Born structures, and the possibility to perform scale variations via reweighting. Our implementation of slepton pair production uses version 1 of the `POWHEG BOX`, whereas the production of a slepton pair in association with a jet is adapted to version 2.

5.1.1 NLO contributions

In this subsection, we describe the format in which the various parts of NLO matrix elements must be provided for new implementations in the `POWHEG BOX`. The Born contribution B, the virtual corrections V and the real-emission corrections R are implemented separately. They are supplemented by color correlated Born amplitudes B_{ij} and spin correlated Born amplitudes $B_j^{\mu\nu}$. All formulae presented here are valid in conventional dimensional regularization.

The Born contribution B for a set of given external particles and momenta should be assigned to the variable `born` by a user routine `setborn` in the format

$$\texttt{born} = N \sum_{\substack{\text{spin}\\ \text{color}}} \mathcal{M}^B \mathcal{M}^{B*}. \tag{5.1}$$

The amplitude $\mathcal{M}^B$ of all Born diagrams is multiplied with its complex conjugate $\mathcal{M}^{B*}$ and summed over spin, color, and polarization degrees of freedom of all external particles. In the normalization factor $N = (N_{\text{sym}} D_\oplus D_\ominus S_\oplus S_\ominus)^{-1}$, a division through the numbers of color degrees of freedom $D_\oplus, D_\ominus$ and spin degrees of freedom $S_\oplus, S_\ominus$ of the incoming particles takes the average over all possible color and spin states of these particles. If several identical particles are present in the final state, the correct normalization is provided by the symmetry factor N_{sym}. The `POWHEG BOX` multiplies the variable `born` by the flux factor $\frac{1}{2s}$ subsequently.

Color correlations for all pairs of external particles in the Born process must be stored by `setborn` in a two dimensional array `bornjk`. Only if both particles i and j carry color charge there is a non-vanishing color correlation. In this case, the color correlated Born B_{ij} is defined according to Eq. (2.97) of Ref. [104] as a modified interference of two Born

amplitudes:

$$\texttt{bornjk(i,j)} = -N \sum_{\substack{\text{spin}\\\text{color}}} \mathcal{M}^{B}_{\{c_k\}} \left(\mathcal{M}^{B*}_{\{c_k\}}\right)_{\substack{c_i\to c'_i\\ c_j\to c'_j}} \mathcal{T}^a_{c_i,c'_i}\mathcal{T}^a_{c_j,c'_j}. \tag{5.2}$$

In the complex conjugate Born amplitude $\mathcal{M}^{B*}_{\{c_k\}}$ with parton color indices $\{c_k\}$, the color indices c_i and c_j of particles i and j are replaced by c'_i and c'_j respectively. The closure of the color structure is achieved by the inclusion of $\mathcal{T}^a_{c_i,c'_i}$ and $\mathcal{T}^a_{c_j,c'_j}$ which stand for $\mathcal{T}^a_{c,b} = if^{cab}$ in the case of gluons, $\mathcal{T}^a_{\alpha,\beta} = T^a_{\alpha\beta}$ in the case of quarks, and $\mathcal{T}^a_{\alpha,\beta} = -T^a_{\beta\alpha}$ in the case of antiquarks. B_{ij} is symmetric under exchange of particles i and j.

Finally, setborn has to fill the array `bmunu` for all external gluons j with the spin correlated squared Born amplitude

$$\texttt{bmunu(mu,nu,j)} = N \sum_{\substack{\text{spin}\\\text{color}}} \mathcal{M}^{B}(\{i\},s_j)\mathcal{M}^{B*}(\{i\},s'_j)(\varepsilon^{\mu}_{s_j})^*\varepsilon^{\nu}_{s'_j} \tag{5.3}$$

as specified in Eq. (2.8) of Ref. [16]. Here, $(\varepsilon^{\mu}_{s_j})^*$ is the polarization vector of gluon j with polarization s_j from the Born amplitude $\mathcal{M}^{B}(\{i\},s_j)$ and $\varepsilon^{\nu}_{s'_j}$ is the corresponding polarization vector of gluon j with polarization s'_j from the complex conjugate Born amplitude $\mathcal{M}^{B*}(\{i\},s'_j)$. The Lorentz indices μ and ν of both polarization vectors are not contracted. Polarization vectors of other particles $\{i\}$ are not modified. If particle j is not a gluon, the spin correlated Born is set to zero.

Infrared divergences in the renormalized virtual contribution $\hat{V}$ are subtracted in the `POWHEG BOX` together with associated terms of order ϵ^0 leaving a finite term V_{fin} which has to be filled by a user routine `setvirtual` into the variable `virtual`. The relation between $\hat{V}$, which can be calculated as two times the real part of the interference of Born and one-loop diagrams plus appropriate counterterms, and V_{fin} is extracted from

$$\hat{V}(\epsilon) = \mathcal{N}(\epsilon)\frac{\alpha_s}{2\pi}\left[-\sum_i\left(\frac{1}{\epsilon^2}C(i)+\frac{1}{\epsilon}\gamma(i)\right)B(\epsilon)+\frac{1}{\epsilon}\sum_{i\neq j}\log\left(\frac{2p_i\cdot p_j}{\mu_R^2}\right)B_{ij}(\epsilon)+V_{\text{fin}}\right] \tag{5.4}$$

as specified in Eq. (2.92) of Ref. [104]. Terms that must be treated as a power series in ϵ are highlighted in this equation. Indices i and j in the sums run over all external particles with color charge in the Born process. For $i = g, q, \overline{q}$, the constants $C(i)$ and $\gamma(i)$ take the values

$$C(g) = C_{\text{A}}, \tag{5.5}$$
$$C(q) = C(\overline{q}) = C_{\text{F}}, \tag{5.6}$$
$$\gamma(g) = \frac{11}{6}C_{\text{A}} - \frac{2}{3}T_f n_f, \tag{5.7}$$
$$\gamma(q) = \gamma(\overline{q}) = \frac{3}{2}C_{\text{F}}, \tag{5.8}$$

in terms of the number n_f of light quark flavors, $C_{\text{A}} = 3$, $C_{\text{F}} = 4/3$, and $T_f = 1/2$. The factor

$$\begin{aligned}\mathcal{N} &= \frac{(4\pi)^\epsilon}{\Gamma(1-\epsilon)} \\ &= 1 + \left[\log(4\pi) - \gamma_E\right]\epsilon + \frac{1}{12}\left[6\gamma_E^2 - 12\gamma_E\log(4\pi) + 6\left(\log(4\pi)\right)^2 - \pi^2\right]\epsilon^2 + \mathcal{O}\left(\epsilon^3\right)\end{aligned} \tag{5.9}$$

extracts the universal constants of D-dimensional integrals following the lines of the $\overline{\text{MS}}$ scheme.

For $pp \to \tilde{\ell}^+\tilde{\ell}^- + X$ no terms of order ϵ^0 are generated in the products of IR poles with the Born B and the color correlated Born B_{ij} in Eq. (5.4) since the squared Born amplitude in D dimensions coincides exactly with the four-dimensional result. However, for the implementation of slepton pair production in association with a jet, such terms need to be subtracted to determine V_{fin} as described in Sec. 5.4 below.

The real-emission contribution R with one additional final state parton needs to be evaluated for a larger number of external particle configurations by a user routine `setreal` that stores the modulus squared of the real emission amplitude $\mathcal{M}^R$ according to the specifications of Ref. [16] in the variable

$$\texttt{amp2} = \left(\frac{\alpha_s}{2\pi}\right)^{-1} N \sum_{\substack{\text{spin}\\ \text{color}}} \mathcal{M}^R \mathcal{M}^{R*}. \tag{5.10}$$

While it is in general necessary to evaluate each configuration of external particle flavors individually, the `POWHEG BOX` checks if results for some of the flavor configurations are identical or proportional to other ones. If such relations are found, they are used to reduce the number of flavor configurations for which the user routines are called.

5.1.2 Usage of the POWHEG BOX

The `POWHEG BOX` consists of general routines in the main directory and process specific routines, which are put into individual subdirectories. For each process, specific executable files are generated by the `Makefile` in the corresponding subdirectory. The main program `pwhg_main` provides the matching of next-to-leading order matrix elements according to the `POWHEG` method. If requested by the user, it generates histograms for the fixed-order result. As final step of the main program, partonic events are written into a Les Houches Event File (LHEF) [23]. These events can subsequently be analyzed by the program `lhef_analysis`, which generates histograms analogously to the main program. To include parton showers and further effects like hadronization and decays, the events are handed over to one of the MC programs `PYTHIA` or `HERWIG` by the executables `main-PYTHIA-lhef` or `main-HERWIG-lhef` respectively.

The program `pwhg_main` requires a file `powheg.input` with technical and physical parameters in the working directory. Crucial parameters that need to be specified for each run in `powheg.input` include the beam energies, the types of the incoming hadrons, and their PDFs. For a list of mandatory parameters in `powheg.input`, we refer to the `POWHEG BOX` manuals in the subdirectory `Docs`. Our following discussion of input parameters is limited to those which are of special relevance for the applications of our codes. Parameters which determine the accuracy of the phase-space integration are discussed in Sec. 5.1.3. Optimized settings of these parameters for each specific process can be found in the respective `Docs` subdirectories or in prepared `powheg.input` files.

While the `POWHEG BOX` was designed for the combination of next-to-leading order matrix elements with parton showers, it can be restricted to LO matrix elements, which facilitates comparisons of different orders in perturbation theory in the same setup. If the option `bornonly` is chosen, only the Born part of the NLO matrix elements is used. Setting numerical values for the optional parameters `renscfact` and `facscfact`, one can easily modify the renormalization scale μ_R and the factorization scale μ_F, which are multiplied by these numbers respectively.

For processes like $pp \to \tilde{\ell}^+\tilde{\ell}^- j + X$ with divergences in infrared limits of the external particles in the Born configurations, it is necessary to avoid or suppress the corresponding regions in phase space. The variable `bornktmin` sets a lower limit for the transverse momentum of the final-state parton in the underlying Born configuration. When a Born suppression factor is used, the value of `bornsuppfact` determines the suppression scale.

Histogram data files at the chosen fixed order in perturbation theory are generated if the variable `testplots` is set to one. Based on general routines for the generation of histograms that are provided by the `POWHEG BOX`, each process is equipped with a file `pwhg_analysis.f` that defines histograms and fills them with data. These histogram routines, which can easily be adapted, are used for fixed-order results, in the analysis of the LHEF, and for the distributions after inclusion of the parton shower. All histogram data are written out in a format that is suitable for plots either in `topdrawer` or in `gnuplot`.

The variable `numevts` specifies the number of partonic events that are generated in the last step of the main program. They are stored in an LHEF, a standard format for event files that are supposed to be read by MC programs. Multi-purpose Monte-Carlo programs that comply with the Les Houches Interface for User Processes can process this file and append a parton shower to the hard interaction. This approach has the advantage that it is not limited to a specific program that provides the shower. However, the parton shower must not generate emissions at larger transverse momenta than those contained in the LHEF. Showers that are ordered in p_{T} fulfill this requirement if the starting scale is chosen appropriately, otherwise a p_{T} veto must be included.

Parallelization is supported in the `POWHEG BOX` as a means to increase the numerical accuracy or to reduce the execution time of the program when several CPUs are available. By default, the degree of parallelization in the `POWHEG BOX` is not supposed to exceed 200. In parallel `POWHEG BOX` calculations, the main program needs to be called repeatedly with different seeds and some parameters in `powheg.input` need to be updated after each step. When the variable `manyseeds` is set to one, parallelization is enabled and all calls of `pwhg_main` must be supplemented by a number that specifies a seed in the file `pwgseeds.dat` that has to be put into the working directory. Consecutive steps in the parallel calculation are numbered by `parallelstage` and optionally `xgriditeration`, which must be updated by the user before the next step.

The evaluation at fixed order in perturbation theory proceeds independently for each parallel process. Hence, all parameters that determine the numerical precision must be chosen so that the accuracy of each independent calculation is sufficient. A combination of parallel fixed-order results is possible at the histogram level. In all parallel calculations, a number `numevts` of events is generated in separate LHEFs that can easily be merged to one single file afterwards. It is thus possible to split the time consuming process of event generation at a high level of parallelization.

5.1.3 Integration Routines and Parameters

Phase space integrations in the `POWHEG BOX` are performed by routines of the program `MINT` [181], which was built specifically for `POWHEG` applications. `MINT` uses Monte-Carlo methods for the integration of functions on multi-dimensional unit cubes. During the implementation of a new `POWHEG BOX` process, a mapping of the Born phase space to a unit cube with the same number of dimensions has to be provided.

At the beginning of the integration, a grid is generated and iteratively refined to capture the main contributions of the function f which shall be integrated. For all coordinates x^k

parameter	value
foldcsi	2
foldy	2
foldphi	2

Table 5.1: Folding parameters in our phenomenological studies of $pp \to \tilde{\ell}^+\tilde{\ell}^- + X$ and $pp \to \tilde{\ell}^+\tilde{\ell}^- j + X$.

$(k = 1, \ldots, n)$, the interval $[0, 1]$ is divided into 50 bins. The n-dimensional unit cube is split into a grid of hyper-rectangles which are products of these bins. In `itmx1` iterations, the absolute value of f is evaluated at `ncalls1` random points in the grid. The bins in all coordinates are adjusted so that for each bin the integral of $|f|$ over this bin and all other $n-1$ dimensions converges more and more towards a common value with every iteration.

The integral of f is computed by the evaluation at `ncalls2` random points in the previously determined grid, which is repeated in `itmx2` iterations. For higher accuracy in the integration over the radiation phase space, the variables `foldcsi`, `foldy`, and `foldphi` can be used. Allowed values for these variables are all integer divisors of 50, the number of bins in each coordinate. The resolution in each radiation coordinate is multiplied by the corresponding degree of folding. Consequently, the complexity of the integration grows proportionally to the product of the three folding variables. It is thus necessary to find a suitable compromise between the benefits of the folding like a smaller contribution with negative weight and its costs in terms of computing time for each specific process.

For the generation of unweighted events (i.e. each generated configuration carries the same weight) these events need to be distributed with a density proportional to the differential cross section. `MINT` calculates in a number `nubound` of steps an upper bounding function that is composed of products of stepwise functions to approximate the actual differential cross section during the generation of events. Due to the special choice of the upper bounding function, the required storage space for intermediate data grows linearly with the dimension of the integration whereas more direct approaches like [153] exhibit an exponential growth of the storage space.

In our phenomenological studies of slepton pair production and the production of a slepton pair in association with a jet, we set the folding parameters `foldcsi`, `foldy`, and `foldphi` to the values that are given in Tab. 5.1. Respective values of the parameters `ncall1`, `itmx1`, `ncall2`, `itmx2`, `nubound`, `numevts` and for the degree of parallelization in $pp \to \tilde{\ell}^+\tilde{\ell}^- + X$ and $pp \to \tilde{\ell}^+\tilde{\ell}^- j + X$ are reported in Sec. 5.3 and Sec. 5.4.

5.2 Software Tools

We summarize in this section the software tools that we use for the implementation of slepton pair production and the production of a slepton pair in association with a jet in the `POWHEG BOX`. More details on the specific usages of these programs for our implementations of $pp \to \tilde{\ell}^+\tilde{\ell}^- + X$ and $pp \to \tilde{\ell}^+\tilde{\ell}^- j + X$ are given in the respective sections for both processes below.

In our calculations of NLO matrix elements, we use the `Mathematica` [229] packages `FeynArts 3.6` [131] for the generation of Feynman diagrams, `FormCalc 7.1` [134, 132] for the combination and simplification of the generated diagrams, and `LoopTools 2.7` [134] for the evaluation of integrals. `FeynArts` treats the general kinematic structure separately

from the actual couplings and particles of a concrete model, which need to be supplied in a specific file. We utilize the model file `MSSMQCD.mod` [135] that is provided as part of `FeynArts` and contains the Feynman rules of the complete MSSM, based to large parts on [159]. `FormCalc` offers the comfort of a `Mathematica` interface while the complicated algebraic manipulations, which are necessary for the evaluation of Feynman diagram interferences, are passed to the efficient specialized program `FORM` [217]. Integrals from the Passarino-Veltman reduction [190] in `FormCalc` can be evaluated with `LoopTools`, that builds upon the program FF [216] for scalar integrals. Some parts of the code for the virtual corrections, that are calculated independently [220] and checked against our results, rely on `Reduze 2` [211, 221] for the reduction to scalar master integrals. For the part of the virtual corrections, which is implemented based on our results, the reduction to scalar integrals is performed with formulae of [84, 85]. Only scalar integrals enter the codes of our `POWHEG BOX` implementations, these are evaluated by `QCDloop` [92, 216]. Matrix elements for tree diagrams in $pp \to \tilde{\ell}^+\tilde{\ell}^- j + X$ are calculated with `MadGraph4` [210, 24].

The input of physical parameters proceeds in both of our implementations via a SUSY Les Houches Accord (SLHA) [209, 19] interface. For $pp \to \tilde{\ell}^+\tilde{\ell}^- + X$, we use the program `SLHALib 2` [133] to read all MSSM parameters from an SLHA file. In the case of $pp \to \tilde{\ell}^+\tilde{\ell}^- j + X$, the physical parameters are read in and processed by the SLHA routines of `MadGraph4`. To provide appropriate phase space parameterizations for our implementations, we adapt the corresponding `POWHEG BOX` codes for heavy-quark pair production [105] in the case of $pp \to \tilde{\ell}^+\tilde{\ell}^- + X$ and $pp \to t\bar{t}j + X$ [18] for $pp \to \tilde{\ell}^+\tilde{\ell}^- j + X$. PDFs are taken from the MSTW 2008 NLO [171] set, that is part of the `LHAPDF` [225] library.

Parton showers are provided by `PYTHIA 6.4.25` [205]. Not only parton showers, but also many other physical effects relevant for collider processes can be simulated by `PYTHIA`. One of these effects is the decay of unstable particles, which transforms sleptons into those particles that are seen in detectors or escape from detection. Decays can be activated by the setting of `PYTHIA` switches only in conjunction with hadronization. We modify the `PYTHIA` code in a minimal way, so that decays can be enabled without hadronization.

Our analysis routines are based on the templates that are provided in the `POWHEG BOX`, but we also use additional programs for specific tasks. The combination of final state partons into jets is performed by `FastJet` [59, 61] via the anti-k_T algorithm [60]. For an efficient evaluation of the kinematical variable m_{T2} [166], we use the code of Ref. [72].

5.3 Slepton Pair Production

In this section, we describe all specific steps, which are performed to generate the code for our `POWHEG BOX V1` implementation of slepton pair production. Both the calculation of the NLO SQCD matrix elements with the help of several software tools and the treatment of physical parameters are described in detail.

We calculate the matrix elements for the partonic process $q\overline{q} \to \tilde{\ell}^+\tilde{\ell}^-$ at next-to-leading order in supersymmetric QCD with the help of the `Mathematica` packages `FeynArts`, `FormCalc`, and `LoopTools`. Our result for the fixed-order matrix elements is used to check a second independent calculation [220] that forms the basis of the code which is implemented in the `POWHEG BOX`. This calculation uses the structural decomposition which is described in Sec. 4.3 to obtain a compact result for the real-emission contribution. It also provides the color and spin correlated Born amplitudes and the leading color approximation of the Born contribution.

After the specification of a model with all particles and couplings, the number of loops inside the diagrams, and the external particles in the partonic process, `FeynArts` automatically generates all allowed topologies of Feynman diagrams and the corresponding particle insertions. For our calculations in the general MSSM, we utilize the model file `MSSMQCD.mod`, which is provided as part of `FeynArts`. It is in principle possible to group all particles of one generation during the diagram generation in `FeynArts`. However, we choose to generate all diagrams individually to have direct control over all associated parameters.

The order of perturbation theory determined by the overall powers of the coupling constants in each diagram cannot be chosen directly, but it is possible to exclude topologies or particles in the generation of the diagrams. This approach reduces the number of diagrams that need to be generated, which makes it more efficient than the selection of diagrams with the desired couplings once their amplitudes have been calculated. In the case of slepton pair production, the exclusion procedure is sufficient for the selection of all diagrams. `FeynArts` applies the Feynman rules for all generated diagrams as final step, creating algebraic expressions for the amplitudes without further modifications.

The evaluation of all diagrammatic amplitudes and interferences, i.e. steps like the calculation of fermionic traces, determination of color factors, or summation of polarizations, is performed in `FormCalc`. Throughout these calculations, we use conventional dimensional regularization to regularize both UV and IR divergences. For loop integrals, we apply the standard Passarino-Veltman reduction in `FormCalc`, that is described in App. B, to generate coefficient integrals which can be evaluated numerically in `LoopTools`.

In the real-emission corrections, a gluon is added to the external particles of the Born contribution. The sum over gluon polarizations is calculated in `FormCalc` via Eq. (2.28), which introduces a light-like auxiliary vector n. The squared matrix element must not depend on this vector, which is confirmed explicitly in our calculation of the real-emission contribution through the cancelation of all terms that include the auxiliary vector n after appropriate algebraic manipulations.

We report contributions to the NLO SQCD matrix element of the partonic process $u\overline{u} \to \tilde{\ell}_1^+ \tilde{\ell}_1^-$ with arbitrary slepton mixing. Since all quarks except the top quark are treated as being massless in our calculations, only the masses m_Z of the Z boson and $m_{\tilde{\ell}}$ of the slepton $\tilde{\ell}_1^\pm$ are present. Mixing between the slepton interaction eigenstates $\tilde{\ell}_L, \tilde{\ell}_R$ and the propagating mass eigenstates $\tilde{\ell}_1, \tilde{\ell}_2$ is given by a unitary matrix U according to

$$\begin{pmatrix} \tilde{\ell}_1 \\ \tilde{\ell}_2 \end{pmatrix} = \begin{pmatrix} U_{11} & U_{12} \\ U_{21} & U_{22} \end{pmatrix} \begin{pmatrix} \tilde{\ell}_L \\ \tilde{\ell}_R \end{pmatrix}. \tag{5.11}$$

The partonic Mandelstam kinematical invariants, which also occur in our results, are defined in App. A.

The Born matrix element is given by

$$\begin{aligned} B = \frac{1}{3^2}\frac{1}{2^2}\frac{2\alpha^2\pi^2(\hat{t}\hat{u} - m_{\tilde{\ell}}^4)}{3(\cos\theta_W)^4(\sin\theta_W)^4(m_Z^2 - \hat{s})^2} \\ \Big[9\left((2(\sin\theta_W)^2 - 1)|U_{11}|^2 + 2(\sin\theta_W)^2|U_{12}|^2\right)^2 \\ + \hat{s}^{-2}\left(-16(\cos\theta_W)^2(\sin\theta_W)^2(m_Z^2 - \hat{s})\right. \\ \left. +(8(\sin\theta_W)^2 - 3)\hat{s}\left((2(\sin\theta_W)^2 - 1)|U_{11}|^2 + 2(\sin\theta_W)^2|U_{12}|^2\right)\right)^2\Big], \end{aligned} \tag{5.12}$$

which includes appropriate average factors for the incoming quarks in the summation over spin and color. This result is exact in D dimensions, i.e. there are no terms proportional to $(D-4)$ or higher powers thereof.

Analogously, we obtain for the real-emission contribution to the NLO SQCD matrix element for the partonic channel $u\overline{u} \to \tilde{\ell}_1^+ \tilde{\ell}_1^- g$ with arbitrary slepton mixing in D dimensions

$$
\begin{aligned}
R = & \frac{64\alpha^2\alpha_s\pi^3}{9(\cos\theta_W)^4(\sin\theta_W)^4(m_Z^2-\hat{s}_{34})^2\hat{s}_{34}^2(\hat{s}+\hat{t}+\hat{t}_{14}-2m_{\tilde{\ell}}^2)(\hat{s}_{34}+\hat{t}+\hat{t}_{14}-2m_{\tilde{\ell}}^2)} \\
& \Big\{(8(\cos\theta_W)^2(\sin\theta_W)^2(m_Z^2-\hat{s}_{34}) \\
& \Big[\left((-1+2(\sin\theta_W)^2)|U_{11}|^2+2(\sin\theta_W)^2|U_{12}|^2\right)\hat{s}_{34}(3-8(\sin\theta_W)^2) \\
& \quad +16(\cos\theta_W)^2(\sin\theta_W)^2(m_Z^2-\hat{s}_{34})\Big] \\
& +\Big[-8(\cos\theta_W)^2(\sin\theta_W)^2(m_Z^2-\hat{s}_{34})(-3+8(\sin\theta_W)^2)+ \\
& \quad \left((-1+2(\sin\theta_W)^2)|U_{11}|^2+2(\sin\theta_W)^2|U_{12}|^2\right) \\
& \quad \hat{s}_{34}(9-24(\sin\theta_W)^2+32(\sin\theta_W)^4)\Big] \\
& \hat{s}_{34}\left((-1+2(\sin\theta_W)^2)|U_{11}|^2+2(\sin\theta_W)^2|U_{12}|^2\right)\Big\} \\
& \Big\{(D-4)\Big[\hat{s}_{34}((\hat{t}_{14}+\hat{t}_{24}-2m_{\tilde{\ell}}^2)^2+\hat{s}_{34}(\hat{t}_{14}+\hat{t}_{24}-m_{\tilde{\ell}}^2)) \\
& \quad +\hat{s}\hat{s}_{34}(\hat{s}_{34}+\hat{t}_{14}+\hat{t}_{24}-4m_{\tilde{\ell}}^2)+\hat{s}^2m_{\tilde{\ell}}^2\Big] \\
& +2\Big[\hat{s}_{34}^2\hat{t}_{24}+\Big(\hat{s}^2+2\hat{s}(\hat{t}+\hat{t}_{14}-2m_{\tilde{\ell}}^2)+2(\hat{t}+\hat{t}_{14}-2m_{\tilde{\ell}}^2)^2\Big)m_{\tilde{\ell}}^2 \\
& \quad +\hat{s}_{34}\Big(\hat{t}_{14}\hat{t}_{24}+\hat{t}_{24}^2+2\hat{t}_{14}m_{\tilde{\ell}}^2-4\hat{t}_{24}m_{\tilde{\ell}}^2-2m_{\tilde{\ell}}^4 \\
& \quad +\hat{s}(\hat{t}_{24}+m_{\tilde{\ell}}^2)+\hat{t}(-\hat{t}_{14}+\hat{t}_{24}+2m_{\tilde{\ell}}^2)\Big)\Big]\Big\}. \qquad (5.13)
\end{aligned}
$$

The unrenormalized virtual QCD correction V_{QCD} to $u\overline{u} \to \tilde{\ell}_1^+ \tilde{\ell}_1^-$ can be written as

$$
\begin{aligned}
V_{\mathrm{QCD}} = & -\frac{2\alpha_s}{3\pi}\frac{(4\pi)^\epsilon}{\Gamma(1-\epsilon)} \\
& \left[\frac{2}{\epsilon^2}+\frac{1}{\epsilon}\left(3+2\log\left(\frac{\mu_R^2}{\hat{s}}\right)\right)+8+3\log\left(\frac{\mu_R^2}{\hat{s}}\right)+\log\left(\frac{\mu_R^2}{\hat{s}}\right)^2-\pi^2\right]B \\
& +\mathcal{O}(\epsilon), \qquad (5.14)
\end{aligned}
$$

where all terms associated with the loop are factorized from the Born contribution B. For the virtual SQCD correction, a factorization is only possible at the level of helicity amplitudes due to split squark mass states in general scenarios.

The NLO SQCD partonic matrix elements are implemented in the `POWHEG BOX` and evaluated for the relevant combinations of external particles. We consider the quarks u, d, c, s, which are treated as being massless, their antiparticles, and gluons as incoming partons. Crossing relations allow to evaluate partonic configurations with permuted external particles based on the same matrix element when appropriate sign and normalization factors are included.

Physical parameters of the general MSSM are specified in one file that complies with the SUSY Les Houches Accord. This file is read by the program `SLHALib 2`, which we interface to our code that processes the data further. Supersymmetric spectrum generators create SLHA files based on specific assumptions like the SUSY breaking mechanism and

appropriate boundary conditions. These files can directly be used for the input of MSSM parameters to our program. While SLHA files allow the inclusion of decay tables, this feature is not used in our program. Instead, decays are handled by the multi-purpose MC program `PYTHIA` according to the mass spectrum.

We do not introduce additional constraints for the supersymmetric masses and mixing parameters in the SLHA file. In particular, the mixing of sleptons by a unitary matrix is allowed. While effectively no mixing should occur for selectrons and smuons, the superpartners of light electrons and muons, sizeable mixing effects are expected in the third generation of charged sleptons.

Our code offers the possibility to choose between a fixed electroweak coupling or a running electroweak coupling, that captures the leading effects of light fermion loops [21]. For the running coupling, the dynamical energy scale Q^2, where the coupling gets evaluated, is set to the invariant mass of the slepton pair in each event. Based on the value of the fine-structure constant $\alpha^{\mathrm{ONS}}(0) = 1/137.035999074$ [45] as well as the values specified in the SLHA input file for the W and Z boson masses m_W, m_Z, the electromagnetic coupling at the Z mass scale in $\overline{\mathrm{MS}}$ renormalization $\alpha^{\overline{\mathrm{MS}}}(m_Z)$, and the Fermi constant G_F, the running electroweak coupling $\alpha^{\mathrm{ONS}}\left(Q^2\right)$ in on-shell renormalization is calculated via

$$\alpha^{\mathrm{ONS}}\left(Q^2\right) = \alpha^{\mathrm{ONS}}(0)\left(1 - \delta\alpha - \frac{\alpha^{\mathrm{ONS}}(0)}{3\pi}\left(3 + 1 + \frac{8}{3}\right)\log\left(\frac{Q^2}{m_Z^2}\right)\right)^{-1}, \tag{5.15}$$

with

$$\delta\alpha = 1 - \frac{\alpha^{\mathrm{ONS}}(0)}{\alpha^{\overline{\mathrm{MS}}}(m_Z)} - \frac{\alpha^{\mathrm{ONS}}(0)}{\pi}\left(\frac{100}{27} - \frac{1}{6} - \frac{7}{4}\log\left(\frac{m_Z^2}{m_W^2}\right)\right). \tag{5.16}$$

The third term in Eq. (5.16) subtracts the difference $\alpha^{\overline{\mathrm{MS}}}(m_Z) - \alpha^{\mathrm{ONS}}(m_Z)$ evaluated at leading order [45]. From the same input parameters, also the Weinberg angle θ_W is determined according to

$$\sin\left(2\theta_W\right) = \left(2\sqrt{2}\pi\frac{\alpha^{\mathrm{ONS}}(0)}{1-\delta\alpha}\frac{1}{G_F m_Z^2}\right)^{\frac{1}{2}}. \tag{5.17}$$

To validate our implementation, we perform several comparisons against calculations in the literature. Our leading order squared matrix element for $u\overline{u} \to \tilde{\ell}_1^+\tilde{\ell}_1^-$ with arbitrary slepton mixing in Eq. (5.12) coincides with the analytical result for the differential cross section $\mathrm{d}\hat{\sigma}/\mathrm{d}\hat{t}$ in Ref. [51] after multiplication with the appropriate phase space integration factor $1/(16\pi\hat{s}^2)$ [192]. An independent calculation [220] agrees with our matrix elements and the evolution equation for the running electroweak coupling. Numerical comparisons of the total cross sections for slepton pair production at LO and at NLO show agreement both with numbers reported in [56] and with results obtained [220] by the publicly available computer program `PROSPINO` [38].

Specific parameters that we use for the phase space integration in our phenomenological studies of $pp \to \tilde{\ell}^+\tilde{\ell}^- + X$ are reported in Tab. 5.2. With these settings, the grid generation and the integration are completed within 20 minutes on an Intel Xeon E5-2670 CPU with 2.6 GHz and 32 GB RAM. Half an hour later, all events are generated. After 40 more minutes, the event analysis in `PYTHIA` without multiple interactions, hadronization, QED radiation, or underlying event is complete.

parameter	value
ncall1	100 000
itmx1	3
ncall2	100 000
itmx2	4
nubound	100 000
numevts	100 000

Table 5.2: Technical parameters for each of 40 parallel calculations in our phenomenological studies of $pp \to \tilde{\ell}^+\tilde{\ell}^- + X$.

5.4 Slepton Pair Plus Jet Production

Here, we describe the specific steps for the POWHEG BOX V2 implementation of slepton pair production in association with a jet. While several parts of this work proceed in analogy to the implementation of slepton pair production in the POWHEG BOX V1 with appropriate refinements and extensions, there are differences in some parts due to the application of new tools and limitations of the considered setup. In order to reduce the high complexity of the NLO SQCD corrections, this implementation as of now is restricted to left-handed sleptons and degenerate squarks. In this way, significant simplifications in the matrix element are achieved while the consequences for phenomenological studies are not severe. The production cross section for left-handed sleptons is larger than for right-handed sleptons and high mass bounds for sparticles with color charge from LHC searches do not allow for large corrections from virtual diagrams with squarks. An extension to more general setups within the same framework is feasible in the future.

All tree contributions to the NLO SQCD matrix element for the hard interaction are generated [144] via the interface of the POWHEG BOX to MadGraph. With the help of this tool, the Born and real-emission contributions, as well as the required color and spin correlations and the leading color approximation of the Born color structure can be obtained in a highly automated way. For a correct treatment of supersymmetric particles, we have to make slight modifications to the POWHEG BOX V2 particle numbering routines that are used in the interface to MadGraph.

Our calculation of the virtual corrections proceeds in general along the same lines, based on FeynArts and FormCalc, as in the case of slepton pair production. For the production of a slepton pair in association with a jet, the number of one-loop diagrams is significantly larger and their structure is more complicated than in the case of slepton pair production. It turns out not to be feasible to select the diagrams at a specific order of the coupling constants only by the efficient exclusion mechanisms for particles and topologies that are offered by FeynArts. Consequently, we use exclusions to the extent applicable and add a second step in the diagram selection that filters out all diagrams with inappropriate couplings after the application of the Feynman rules. One advantage of this selection method is the reduced risk of missing diagrams.

For a consistent evaluation of D-dimensional fermionic traces that include γ_5, we construct an implementation of Dirk Kreimer's scheme [160] in Mathematica that replaces default FormCalc routines in our one-loop calculations. The original algorithm of Ref. [160] evaluates the trace via sums over permutations of numerous subsets of the Lorentz indices in the trace. Since this procedure is rather slow, we develop a recursive algorithm that

evaluates traces with γ_5 more efficiently. To check this algorithm, we compare results for fermionic traces with γ_5 up to the maximal length that occurs in the process under consideration to the respective results that are obtained with the original algorithm and find agreement.

It should also be noted that a Lorentz contraction of the polarization sum, which is evaluated according to Eq. (2.28), yields a factor of $(2 - D)$ in D dimensions. Terms proportional to $D - 4$ generated in this way are irrelevant for slepton pair production at NLO, since external gluons appear only in the real-emission contribution of this process. However, in the case of slepton pair production in association with a jet, terms proportional to $D - 4$ from the polarization sum are multiplied by poles from loops in the virtual corrections and lead to contributions that do not vanish in the limit $D \to 4$.

Due to the high complexity of the virtual corrections, algebraic manipulations in our `FormCalc` calculation do not succeed in removing the auxiliary vector n that originates from the gluon polarization sum according to Eq. (2.28). For numerical evaluations, it is necessary to use suitable values for n, like the four-momentum of one of the incoming massless particles. We check that the overall virtual contribution is independent of n by substituting both four-momenta of the incoming quark and antiquark for n, which leads to identical results.

One of the major challenges in the calculation of the virtual corrections is the large size of intermediate expressions. `FormCalc` automatically introduces abbreviations for several suitable sub-expressions, but we find that the introduction of further abbreviations is crucial to shrink the term size to a manageable level, especially in the calculation of polarization sums. Thus, we replace the abbreviation scheme of `FormCalc` in these complicated cases by self-made `Mathematica` routines for the generation of abbreviations. The main idea of our abbreviation scheme is the identification of all sub-expressions which contain only terms that can be regarded as insensitive to the operation which is to be performed, e.g. all terms without polarization vectors in the case of polarization sums. Calculations with expressions that are abbreviated in this way are succeeded by several simplification steps, after the abbreviations are put back in. These simplification steps take several hours of computing time, but they are crucial for the generation of efficient code for the numerical phase space integration, since they reduce the size of the code by more than one order of magnitude.

To extract the part V_{fin} of the virtual contributions, which has to be implemented according to the `POWHEG BOX` conventions, we must subtract terms of order ϵ^0 that are generated in the products of infrared poles with plain and color correlated Born amplitudes according to Eq. (5.4). All color correlations can be traced back to the plain Born contribution B via the relations

$$B_{q\overline{q}} = \frac{1}{2}(2C_{\text{F}} - C_{\text{A}})B, \qquad B_{qg} = \frac{1}{2}C_{\text{A}}B \tag{5.18}$$

that were reported in Eq. (2.1) of Ref. [17], where the production of two leptons of opposite charge in association with a jet was implemented in the `POWHEG BOX`. The color structure in this process is exactly identical to the one of $pp \to \tilde{\ell}^+\tilde{\ell}^- j + X$. In this way, we arrive

at the expression

$$V_{\text{fin}} = \hat{V}(\epsilon)\left(\mathcal{N}(\epsilon)\frac{\alpha_s}{2\pi}\right)^{-1} + \frac{1}{\epsilon^2}\left[2C_{\text{F}} + C_{\text{A}}\right]B(\epsilon) + \frac{1}{\epsilon}\left[3C_{\text{F}} + \frac{11}{6}C_{\text{A}} - \frac{2}{3}T_f n_f - (2C_{\text{F}} - C_{\text{A}})\log\left(\frac{2p_q\cdot p_{\overline{q}}}{\mu_R^2}\right) - C_{\text{A}}\log\left(\frac{2p_q\cdot p_g}{\mu_R^2}\right) - C_{\text{A}}\log\left(\frac{2p_{\overline{q}}\cdot p_g}{\mu_R^2}\right)\right]B(\epsilon), \tag{5.19}$$

which can be evaluated at order ϵ^0 with the exact D-dimensional result for the Born contribution (see Eq. (5.13) for the Born contribution of the partonic channel $u\overline{u} \to \tilde{\ell}_1^+\tilde{\ell}_1^- g$ in D dimensions). We check that the infrared poles on the right-hand side of Eq. (5.19) cancel, so that V_{fin} is indeed finite. The number of light quark flavors in Eq. (5.19) is set to $n_f = 5$. However, due to small bottom quark PDFs, we consider only the quarks u, d, c, s, their antiparticles, and gluons as incoming massless partons, like in $pp \to \tilde{\ell}^+\tilde{\ell}^- + X$.

Our results for virtual corrections with Drell-Yan like structure are used as check for an independent calculation [220] that employs the structural decomposition of these amplitudes to generate efficient code for the `POWHEG BOX`. In the implementation of virtual corrections that involve Higgs bosons or a squark-squark-slepton-slepton vertex, we use code that is generated from the results of our calculations in `FeynArts` and `FormCalc`. Like for slepton pair production, `QCDloop` is used to evaluate the loop integrals in our code, which makes a further reduction of the coefficient integrals obtained in the standard Passarino-Veltman decomposition of `FormCalc` to scalar integrals necessary. These transformations are performed with the help of formulae that were reported in [84, 85].

Like for $pp \to \tilde{\ell}^+\tilde{\ell}^- + X$, the physical parameters are read from an SLHA file. However, we use different routines for the input of these parameters in the current implementation, which are provided as part of `MadGraph`. The Z boson mass m_Z, the electromagnetic coupling at the Z mass scale in $\overline{\text{MS}}$ renormalization $\alpha^{\overline{\text{MS}}}(m_Z)$, and the Fermi constant G_F are treated as free parameters of the electroweak sector. Based on their values, the Weinberg angle θ_W is calculated via

$$m_W = \left(\frac{1}{2}m_Z^2 + \left(\frac{1}{4}m_Z^4 - \frac{\pi\alpha}{\sqrt{2}G_F}m_Z^2\right)^{\frac{1}{2}}\right)^{\frac{1}{2}} \tag{5.20}$$

and

$$\sin\theta_W = \left(1 - \frac{m_W^2}{m_Z^2}\right)^{\frac{1}{2}}. \tag{5.21}$$

In the production of a slepton pair in association with a jet, a massless gluon is already emitted at the Born level, which leads to IR singularities in those phase space regions where the gluon becomes soft or collinear to the emitter. A special treatment of these IR singular regions in Born diagrams is required during phase space integration, otherwise a large fraction of the events would be generated in a plain integration near the singularities. There are two ways to avoid this problem in the `POWHEG BOX` [17]:

- The first possibility is the scaling of the cross section with a Born suppression factor F that becomes small when the underlying Born variables Φ_n approach singular regions. If this method is used, `POWHEG` generates weighted events with the reciprocal of the suppression factor as weight.

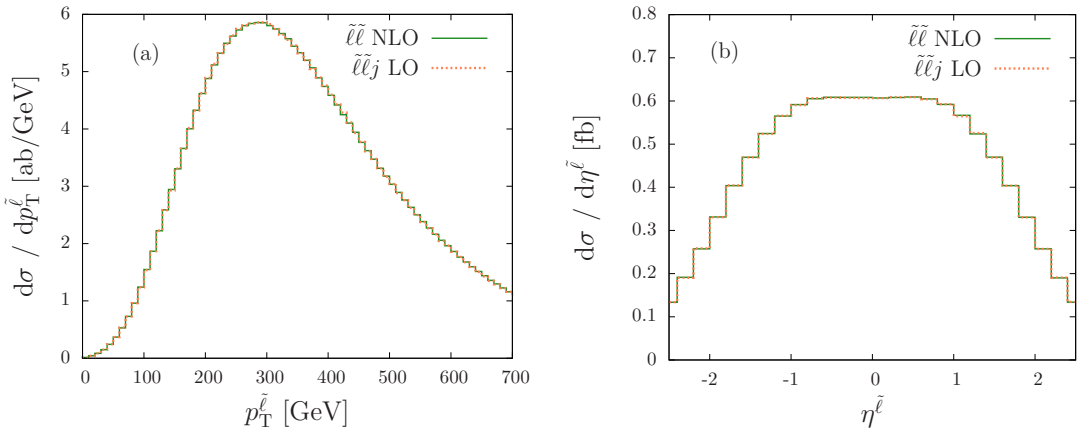

Figure 5.1: Transverse momentum distribution (a) and pseudorapidity distribution (b) of the negatively charged slepton with $m_{\tilde{\ell}} = 350$ GeV in proton collisions at the LHC with 14 TeV center-of-mass energy for $pp \to \tilde{\ell}^+\tilde{\ell}^- + X$ at NLO (green) and for $pp \to \tilde{\ell}^+\tilde{\ell}^- j + X$ at LO (orange) with a cut of 10 GeV on the transverse momentum of the hardest jet.

- The second possibility consists of the application of a generation cut that discards all underlying Born events where the transverse momentum lies below a chosen threshold.

In our implementation of $pp \to \tilde{\ell}^+\tilde{\ell}^- j + X$, we use a combination of both methods. A Born suppression factor F with a suppression scale $\Lambda = 10$ GeV is supplemented by a minimal generation cut of 1 GeV. The functional form of the suppression factor in our code is

$$F\left(\Phi_n\right) = \frac{p_{\mathrm{T},i}^2}{p_{\mathrm{T},i}^2 + \Lambda^2} \tag{5.22}$$

for final-state partons with transverse momenta $p_{\mathrm{T},i}$. We test that our code is stable for different choices of the generation cut and the suppression scale. Consistent results are found in various configurations both for the cross section and for differential distributions.

The real-emission contribution of $pp \to \tilde{\ell}^+\tilde{\ell}^- + X$ is identical to the Born contribution of $pp \to \tilde{\ell}^+\tilde{\ell}^- j + X$. A direct test of this relation forms an important cross-check for our calculations, since we use two different methods to implement these contributions in the respective codes. We simulate the production of left-handed selectrons with a mass of $m_{\tilde{\ell}} = 350$ GeV in proton collisions at the LHC with 14 TeV center-of-mass energy with both codes. In the case of $pp \to \tilde{\ell}^+\tilde{\ell}^- + X$, we use the full NLO matrix elements, while for $pp \to \tilde{\ell}^+\tilde{\ell}^- j + X$, only the Born contribution is selected. A cut of $p_{\mathrm{T}}^{\mathrm{jet1}} > 10$ GeV on the hardest jet, which is applied in both codes, extracts the real-emission part of $pp \to \tilde{\ell}^+\tilde{\ell}^- + X$. For identical electroweak parameters, we find precise agreement between both programs, as illustrated in Fig. 5.1.

We check the Drell-Yan like virtual corrections in our code by numerical comparison to a second independent calculation [220]. In addition, we compare an adapted version of our code to the virtual contribution of lepton pair production in association with a jet using the corresponding `POWHEG BOX` implementation [17]. Adapting the parameters of our code, selecting appropriate diagrams and replacing the sleptons by leptons, we find full agreement between both codes for representative phase-space points. This result provides

parameter	value
`ncall1`	200 000
`itmx1`	2
`ncall2`	300 000
`itmx2`	3
`nubound`	100 000
`numevts`	100 000

Table 5.3: Technical parameters for each of 100 parallel calculations in our phenomenological studies of $pp \to \tilde{\ell}^+\tilde{\ell}^- j + X$.

a strong check of our implementation of the virtual corrections according to the `POWHEG BOX` specifications.

Technical parameters in the phase space integration for our phenomenological studies of $pp \to \tilde{\ell}^+\tilde{\ell}^- j + X$ are listed in Tab. 5.3. Like for $pp \to \tilde{\ell}^+\tilde{\ell}^- + X$, we report the execution time of our code on an Intel Xeon E5-2670 CPU with 2.6 GHz and 32 GB RAM. The grids are generated in two iterations, which take one hour each. After eight hours more, the integration is completed. The longest step consists of the event generation, which requires one day. These events are analyzed by `PYTHIA` for the same settings as in $pp \to \tilde{\ell}^+\tilde{\ell}^- + X$ within two hours.

Chapter 6

Phenomenology

After the completion of our codes for slepton pair production and for the production of a slepton pair in association with a jet, we are in a position to make phenomenological predictions that illustrate possible applications of our new tools in the search for sleptons at hadron colliders.

The detector signatures of slepton pairs depend on the supersymmetric mass spectrum and need to be distinguished from corresponding Standard Model background processes with much larger total cross sections. Searches for supersymmetry are often based on simplified models that focus on the production and decay of specific supersymmetric particles for a given mass spectrum and corresponding decay channels. While this approach can be applied only to restricted scenarios, it has the advantage of clear experimental signatures. Many slepton searches assume that the slepton under consideration is the next-to-lightest supersymmetric particle (NLSP) that decays exclusively into the corresponding lepton and the lightest neutralino,

$$\tilde{\ell} \to \ell + \tilde{\chi}_1^0. \tag{6.1}$$

For a significant mass splitting between the slepton and the neutralino LSP, leptons from the slepton decays are hard and stand out against softer SM backgrounds. Thus, two hard leptons with opposite electric charge and missing transverse momentum due to the unobserved neutralinos are the default signature in searches for slepton pairs. If the mass splitting between slepton and neutralino gets smaller, it becomes more difficult to observe the leptons after the slepton decays and to distinguish them from background. These almost degenerate setups require specific tools and approaches.

We provide in this chapter predictions for the pair production of sleptons of the first and second generation at the LHC in fixed-order perturbation theory and matched to parton showers. Additional jets that are produced in association with the sleptons are examined in detail and the respective predictions of our codes for $pp \to \tilde{\ell}^+\tilde{\ell}^- + X$ and $pp \to \tilde{\ell}^+\tilde{\ell}^- j + X$ are compared. Slepton decays into the corresponding leptons and the lightest neutralino are considered for different sparticle masses respecting current experimental exclusion limits. Specific search strategies based on advanced kinematical variables are proposed for the separation of signal and background in experimentally challenging SUSY mass configurations. Before the application of our new tools, we present an overview of experimental searches for sleptons, followed by a summary of important background processes.

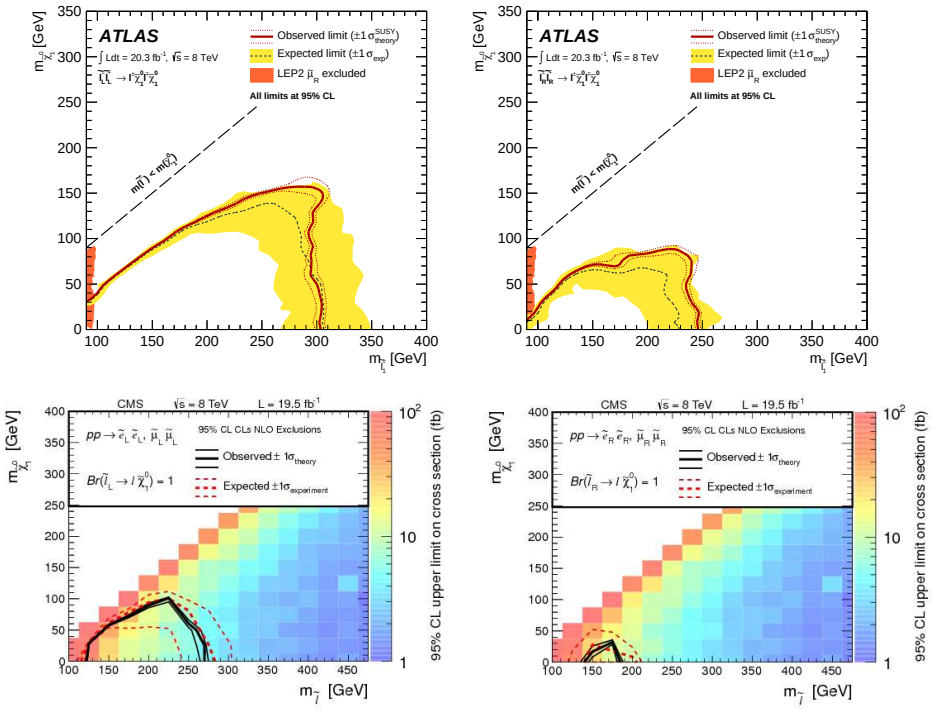

Figure 6.1: Exclusion limits for left-handed sleptons (left) and right-handed sleptons (right) of the first or second generation by ATLAS [9] (top) and CMS [154] (bottom).

6.1 Experimental Results

Supersymmetric particles have been one of the main targets of experimental searches at various collider and indirect detection experiments for many years. Until today, no positive evidence was found, only exclusion limits could be set for supersymmetric parameters in specific models. Unless stated otherwise, all slepton mass limits given below are at 95% confidence level and refer to sleptons of the first and second generation with decays $\tilde{\ell} \to \ell + \tilde{\chi}_1^0$ into the corresponding lepton and a massless neutralino.

Investigations at the e^+e^- collider PETRA more than 30 years ago provided early lower bounds for slepton masses. Smuon masses up to 15 GeV could be ruled out by the MARK-J detector [33]. The TASSO collaboration [55] found slightly higher exclusion limits for selectrons and smuons. Lower bounds in the same mass range were obtained by the CELLO collaboration [39] for all three slepton generations. The JADE collaboration [35] pushed the exclusion limit for smuons above 20 GeV, just as the Mark II detector [114] located at the PEP storage ring did for selectrons.

Important mass limits for sleptons were established by experiments at the Large Electron-Positron Collider (LEP) at the beginning of this millennium. A detailed study of the Z resonance [10] allowed to set a lower bound of 40 GeV on the masses of all sleptons independent of their decay channels [45]. Dedicated slepton searches at LEP by the ALEPH [138], DELPHI [12], L3 [13], and OPAL [11] collaborations set slepton exclusion limits at larger masses [2] under the assumption of gaugino mass unification. The branching fraction of $\tilde{\ell} \to \ell\tilde{\chi}_1^0$ was derived from the mass relations and turned out to lie above 95% in most cases. The neutralino mass is also relevant for the t-channel

production of selectron pairs in the e^+e^- collisions at LEP. In this setup, right-handed selectrons with masses $m_{\tilde{e}_R} \leq 100$ GeV were excluded for neutralino masses $m_{\tilde{\chi}_1^0} \leq 85$ GeV. Similarly, right-handed smuons were excluded up to $m_{\tilde{\mu}_R} \leq 95$ GeV for neutralino masses $m_{\tilde{\chi}_1^0} \leq 85$ GeV.

Since the start-up of the LHC, several slepton searches by the ATLAS and CMS collaborations have extended the tested parameter space to higher energies. With 4.7 fb^{-1} recorded in the year 2011, ATLAS [8] excluded in a flavor-blind analysis left-handed sleptons between 85 GeV and 195 GeV for a neutralino mass of 20 GeV. A more refined analysis with improved exclusion limits was presented in [120].

In the most recent analysis by ATLAS [9], based on 20.3 fb^{-1} integrated luminosity from the LHC with 8 TeV center-of-mass energy, left-handed sleptons between 90 GeV and 300 GeV were excluded. A similar search by CMS [154] based on 19.5 fb^{-1} at 8 TeV excluded left-handed sleptons with masses between 120 GeV and 260 GeV. We reproduce the plots of both experiments that show excluded regions in the plane of slepton and neutralino masses for left-handed and right-handed sleptons, c.f. Fig. 6.1. The plots by ATLAS include LEP limits in the lower left corner. Compared to these limits from a lepton collider, the gap next to the slepton neutralino degeneracy line, which is difficult to probe for hadron-collider experiments, becomes evident.

6.2 Background Processes

Standard Model backgrounds that resemble the default signature of $pp \to \tilde{\ell}^+\tilde{\ell}^- + X$ in particle detectors, which consists of two hard leptons of opposite electric charge and missing transverse momentum, are dominated by diboson production ($W^+W^-, W^\pm Z, ZZ$) and the production of top quarks in $t\overline{t}$ pairs or in association with a W boson. Total cross sections of these backgrounds lie in the range of several tens to hundreds picobarn, c.f. Fig. 1.1, and are thus much larger than slepton pair production cross sections with upper limits of a few femtobarn for current experimental bounds. Consequently, it is crucial to suppress backgrounds as much as possible to have a chance of seeing slepton signals. Top quarks predominantly decay via $t \to b + W^+$ to a bottom quark and a W boson, so their background contribution can be reduced by imposing a veto on b-jets. In $pp \to W^+W^- + X$ with leptonic decays $W^+W^- \to \ell^+\nu\ell^-\overline{\nu}$, the final state consists of two leptons of opposite electric charge and two unobserved particles (the neutrinos), just like for $pp \to \tilde{\ell}^+\tilde{\ell}^- + X$.

Advanced kinematical variables, that are specifically designed to improve the separation of signal and background processes, are key ingredients in the search for new particles. The recent slepton searches by ATLAS [9] and CMS [154] use the kinematical variables m_{T2} [166] and $m_{\mathrm{CT}\perp}$ [174], respectively. Both of these variables are sensitive to the mass differences of pair-produced particles and their decay products. For a large mass splitting between slepton and neutralino, they are efficient in separating $pp \to \tilde{\ell}^+\tilde{\ell}^- + X$ from SM background processes with smaller mass splittings. We reproduce the distributions of recorded data in comparison to simulated backgrounds and representative signals for m_{T2} by ATLAS and $m_{\mathrm{CT}\perp}$ by CMS in Fig. 6.2 to illustrate the shape differences between signal and background for these variables and to show the contributions of various background processes in the potential signal regions.

For very small splitting between $m_{\tilde{\ell}}$ and $m_{\tilde{\chi}_1^0}$, it can be challenging or impossible to identify the leptons from the slepton decays. Such configurations can be observed if additional objects, which are visible in the detectors, are emitted during the process of slepton pair production. Due to the high level of hadronic activity at the LHC, jets

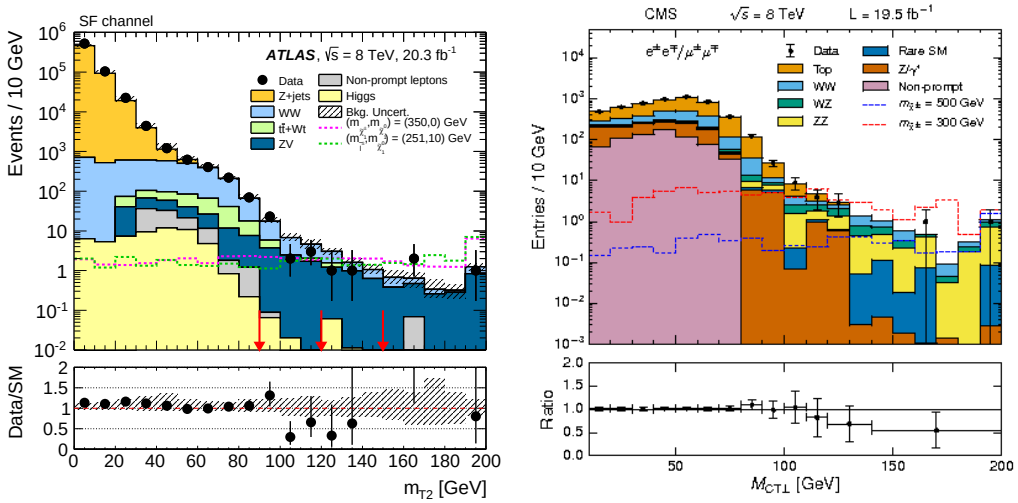

Figure 6.2: Comparison of recorded data to predictions for SM background processes in searches for slepton pairs by ATLAS [9] (left) and CMS [154] (right).

are generated frequently. A detector signature, where a single hard jet is observed, but no other objects that balance the sum of transverse momenta are seen, is referred to as monojet configuration. For this signature, other background processes than for the default slepton signature are important. The dominant backgrounds with one jet and missing transverse energy emerge from the production of a weak boson in association with a jet. Decays of the Z boson into two neutrinos in $pp \to Zj + X$ with $Z \to \nu\nu$ constitute a large irreducible background since the neutrinos leave detectors of collider experiments unobserved. A lepton from the leptonic decay of a W boson in $pp \to Wj+X$ with $W \to \ell\nu$ can escape detection if it is very soft or hidden inside a jet or outside the covered detector area. Sizeable backgrounds involving top quarks can be reduced efficiently via b-jet vetoes. QCD multijet production with inaccurate identification of the jets can be suppressed very much by the application of a large cut on the missing transverse energy [20].

6.3 Numerical Results

We provide predictions for $pp \to \tilde{\ell}^+\tilde{\ell}^- + X$ and $pp \to \tilde{\ell}^+\tilde{\ell}^- j + X$ at the LHC with 14 TeV center-of-mass energy in the proton collisions. All calculations presented here use MSTW 2008 NLO [171] PDFs as implemented in the `LHAPDF` [225] collection. For the renormalization scale μ_R and the factorization scale μ_F, we choose the values $\mu_R = \xi_R\mu_0$ and $\mu_F = \xi_F\mu_0$ with $\mu_0 = 2m_{\tilde{\ell}}$. Unless stated otherwise, both ξ_R and ξ_F are set to one. `PYTHIA 6.4.25` [205] provides parton showers and simulates slepton decays. We do not include QED radiation, underlying event, and hadronization effects in the processing of events by `PYTHIA`. Jets are constructed via the anti-k_T algorithm [60] with a radius parameter $R = 0.4$. Statistical uncertainties in our results due to numerical phase-space integration are very small, thus we do not show them explicitly in the following.

In the electroweak sector, we use as input parameters the current values of the Particle Data Group [45] for the Z boson mass, $m_Z = 91.1876$ GeV, the electroweak coupling at the Z mass scale in $\overline{\text{MS}}$ renormalization $\alpha^{\overline{\text{MS}}}(m_Z) = 1/127.944$, and the Fermi constant

setup	$m_{\tilde{\ell}}$ [GeV]	$m_{\tilde{\chi}_1^0}$ [GeV]
H1	350	305
H2	350	200
H3	350	100
L1	150	135
L2	150	120
L3	150	100

Table 6.1: Setups with different slepton and neutralino masses for our phenomenological analysis.

$G_F = 1.1663787 \times 10^{-5}$ GeV^{-2}. All results for $pp \to \tilde{\ell}^+\tilde{\ell}^- + X$ are obtained with the fixed value of $\alpha^{\overline{\rm MS}}(m_Z)$ specified above, unless stated otherwise, to allow for better comparability to the results of $pp \to \tilde{\ell}^+\tilde{\ell}^- j + X$, where the same fixed value of the electroweak coupling is used.

Based on the recent exclusion limits for sleptons and neutralinos shown in Fig 6.1, we choose six different mass setups, which are listed in Tab. 6.1. For heavy sleptons with $m_{\tilde{\ell}} = 350$ GeV, there are no experimental restrictions on the neutralino mass $m_{\tilde{\chi}_1^0}$. Consequently, we cover a wide range of neutralino masses from 100 GeV to 305 GeV in the heavy-slepton setups H1, H2, H3. Light sleptons are still not excluded for mass values as low as 100 GeV, if the difference to the lightest neutralino mass is small. These almost degenerate scenarios are represented by our light slepton setups L1, L2, L3, with small mass splittings between the sleptons at $m_{\tilde{\ell}} = 150$ GeV and neutralinos in the range from 100 GeV to 135 GeV. In the discussion of observables which do not depend on the neutralino mass, we refer to $m_{\tilde{\ell}} = 350$ GeV as heavy slepton setup and to $m_{\tilde{\ell}} = 150$ GeV as light slepton setup.

Quarks are treated as being massless, except for the top quark with $m_t = 173.07$ GeV. All charginos and all neutralinos, except for the lightest neutralino, are chosen to be heavier than the sleptons, so that they do not enter in the slepton decay chains. Squarks and gluinos have to satisfy strong experimental bounds on their masses. We choose the common mass $m_{\tilde{q}} = 500$ GeV for all squarks and set the gluino mass to $m_{\tilde{g}} = 700$ GeV. The light CP even Higgs boson is assumed to be the particle which was recently discovered by ATLAS and CMS at the mass value $m_{h^0} = 126$ GeV. For the heavy CP even Higgs boson, a mass value of $m_{H^0} = 400$ GeV is chosen.

We use suitable cuts for each observable to account for detector limitations and to improve the signal to background ratio. Leptons are considered to be observable if they fulfill

$$p_{\rm T}^{\ell} > 20 \text{ GeV}, \quad \left|\eta^{\ell}\right| < 2.5. \tag{6.2}$$

Whenever we require a hard jet, it must satisfy

$$p_{\rm T}^{\rm jet1} > 20 \text{ GeV}, \quad \left|\eta^{\rm jet1}\right| < 4.5. \tag{6.3}$$

To ensure that the objects which shall be observed can be resolved separately, we demand a separation in pseudorapidity η and azimuthal angle ϕ via

$$\Delta R_{\ell\ell} > 0.4, \quad \Delta R_{j\ell} > 0.4, \tag{6.4}$$

with $\Delta R = \sqrt{(\Delta\eta)^2 + (\Delta\phi)^2}$, between all visible leptons and hard jets.

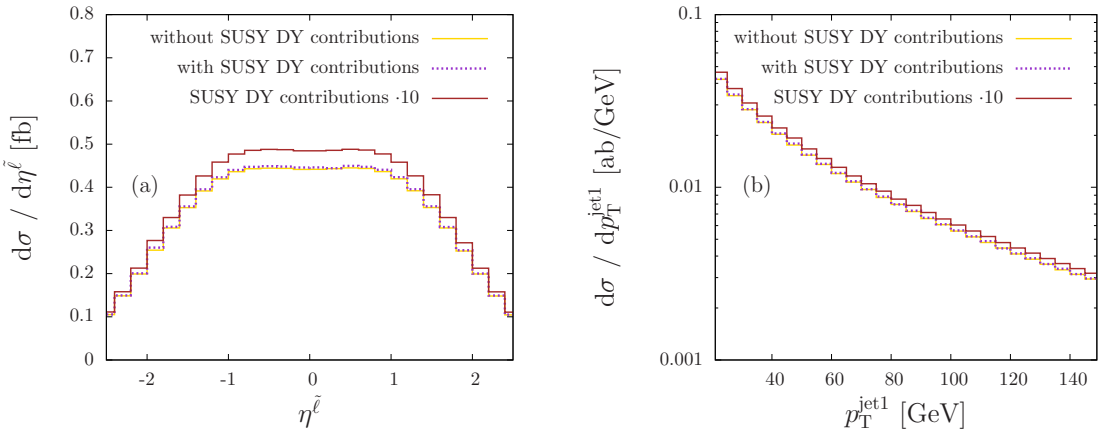

Figure 6.3: Pseudorapidity distribution of the negatively charged slepton (a) and transverse momentum distribution of the hardest jet (b) in $pp \to \tilde{\ell}^+\tilde{\ell}^- j + X$ with the cuts of Eq. (6.3) at NLO in the heavy slepton setup with virtual SUSY Drell-Yan like corrections neglected (yellow), included (purple), or scaled by the factor 10 (brown).

For monojet searches in almost mass-degenerate scenarios, we require a hard jet and missing transverse energy $E_{\mathrm{T}}^{\mathrm{miss}}$, that is defined as the magnitude of the vectorial sum of all missing transverse momenta, with

$$p_{\mathrm{T}}^{\mathrm{jet1}} > 120 \text{ GeV}, \quad \left|\eta^{\mathrm{jet1}}\right| < 4.5, \quad E_{\mathrm{T}}^{\mathrm{miss}} > 150 \text{ GeV}. \tag{6.5}$$

These requirements respect the efficiency thresholds of missing energy triggers and suppress a large part of the Standard Model backgrounds.

Using our codes for $pp \to \tilde{\ell}^+\tilde{\ell}^- + X$ and $pp \to \tilde{\ell}^+\tilde{\ell}^- j + X$, we provide theoretical predictions for the cross section and distributions of sleptons, jets and leptons in different setups. First, we examine the magnitudes of different contributions and find that squarks and gluinos decouple from our calculations. Even for the squark and gluino masses in our setup, which are small compared to current experimental limits, the contribution of diagrams with virtual supersymmetric particles is small. We illustrate this finding with results for the cross section and differential distributions in $pp \to \tilde{\ell}^+\tilde{\ell}^- j + X$ when only specific parts of the virtual corrections are selected.

If we include only the QCD part of the virtual corrections, we obtain a cross section of 1.826 fb in the heavy slepton setup with the cuts of Eq. (6.3). When supersymmetric virtual corrections with a Drell-Yan like structure are added, the cross section is only slightly enhanced to the value 1.842 fb. The effect of supersymmetric Drell-Yan like virtual corrections on differential distributions is illustrated in Fig. 6.3 for the pseudorapidity distribution of the negatively charged slepton (a) and the transverse momentum distribution of the hardest jet (b). In both cases, there is only a small difference between the distributions without supersymmetric Drell-Yan like corrections (yellow) and the distributions which include these corrections (purple). We also include a modified distribution (brown), where the contribution of supersymmetric Drell-Yan like diagrams is scaled by the factor 10, in both histograms to demonstrate that this contribution does not lead to a strong modification of the respective shapes.

The contribution of supersymmetric virtual correction diagrams which do not exhibit a Drell-Yan like structure is even smaller than for the SUSY Drell-Yan corrections. If

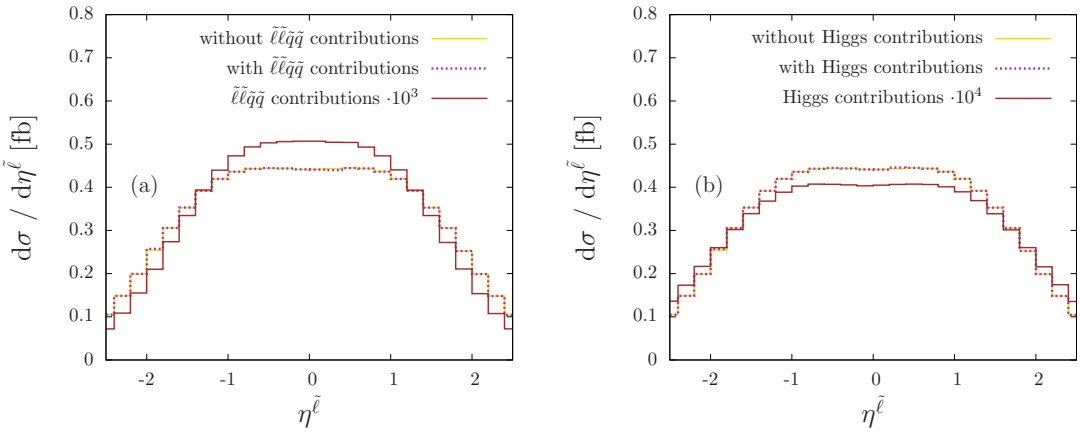

Figure 6.4: Pseudorapidity distribution of the negatively charged slepton in the process $pp \to \tilde{\ell}^+\tilde{\ell}^- j + X$ with the cuts of Eq. (6.3) at NLO in the heavy slepton setup where corrections by diagrams with a squark-squark-slepton-slepton vertex (a) or a Higgs boson (b) are either neglected (yellow), included (purple), or scaled (brown) by the respective factors 10^3 (a) or 10^4 (b).

all of these diagrams are included, we obtain a cross section of 1.841 fb in the heavy slepton setup for the cuts of Eq. (6.3). Also differential distributions are hardly affected by these corrections. We show the effect of not Drell-Yan like virtual corrections on the pseudorapidity distribution of the negatively charged slepton in Fig. 6.4. Both for diagrams with a squark-squark-slepton-slepton vertex (a) and for diagrams with a Higgs boson (b), the distribution is effectively identical when these diagrams are excluded (yellow) or when they are included (purple). If these contributions had a larger magnitude, the slepton distributions would be modified significantly. We provide an illustration of this hypothetical effect by rescaling the amplitude of all diagrams with slepton pairs emerging from a four-particle vertex by the factor 10^3 and the amplitude of all diagrams which involve Higgs bosons by the factor 10^4 (brown). While the 4-sparticle vertex diagrams enhance the production of central sleptons, diagrams with a Higgs boson have the opposite effect.

Due to the small contribution of all virtual correction diagrams in $pp \to \tilde{\ell}^+\tilde{\ell}^- j + X$ apart from the QCD Drell-Yan corrections, we exclude the corresponding parts of the virtual corrections in our phenomenological studies. This simplification allows us to reduce both the number of free parameters in our setup and the execution time of our code.

The total cross section for inclusive slepton pair production at LO and NLO in the heavy slepton setup with $m_{\tilde{\ell}} = 350$ GeV is given in Tab. 6.2 for different choices of renormalization scale μ_R and factorization scale μ_F. Note that there is no renormalization scale dependence in $pp \to \tilde{\ell}^+\tilde{\ell}^- + X$ at Born level, since it is a purely electroweak process. Despite the fact that only the NLO cross section depends on μ_R, the overall scale dependence in the examined range is reduced from 8.9% at LO to 3.9% at NLO. Corresponding results for the cross section in $pp \to \tilde{\ell}^+\tilde{\ell}^- j + X$ with the cuts of Eq. (6.3) are given in Tab. 6.3. In this case, a strong reduction of the scale dependence from 28.6% at LO to 4.8% at NLO can be observed. Already this basic result demonstrates that NLO accuracy for the hardest jet is indispensable in precision predictions, if the presence of one hard jet is required and jet related cuts are applied.

(ξ_R,ξ_F)	(0.5,0.5)	(0.5,1)	(1,0.5)	(1,1)	(1,2)	(2,1)	(2,2)
$\sigma_{\rm LO}^{\tilde{\ell}\tilde{\ell}}$ [fb]			2.477	2.368	2.266		
deviation [%]			4.6	0.0	-4.3		
$\sigma_{\rm NLO}^{\tilde{\ell}\tilde{\ell}}$ [fb]	2.856	2.838	2.826	2.800	2.785	2.768	2.746
deviation [%]	2.0	1.4	0.9	0.0	-0.5	-1.1	-1.9

Table 6.2: Total cross section for $pp \to \tilde{\ell}^+\tilde{\ell}^- + X$ at LO and at NLO in the heavy slepton setup for different choices of (ξ_R,ξ_F) and deviation relative to the cross section at the central scale choice $\xi_R = \xi_F = 1$ respectively.

(ξ_R,ξ_F)	(0.5,0.5)	(0.5,1)	(1,0.5)	(1,1)	(1,2)	(2,1)	(2,2)
$\sigma_{\rm LO}^{\tilde{\ell}\tilde{\ell}j}$ [fb]	1.881	1.766	1.730	1.624	1.530	1.503	1.416
deviation [%]	15.8	8.7	6.5	0.0	-5.8	-7.5	-12.8
$\sigma_{\rm NLO}^{\tilde{\ell}\tilde{\ell}j}$ [fb]	1,845	1,856	1,834	1,825	1,823	1,784	1,768
deviation [%]	1,1	1,7	0,5	0,0	-0,1	-2,2	-3,1

Table 6.3: Cross section for $pp \to \tilde{\ell}^+\tilde{\ell}^- j + X$ at LO and at NLO in the heavy slepton setup with the cuts of Eq. (6.3) for different choices of (ξ_R,ξ_F) and deviation relative to the cross section at the central scale choice $\xi_R = \xi_F = 1$ respectively.

In the light slepton setup, the total cross section is significantly higher than for heavy sleptons. For $pp \to \tilde{\ell}^+\tilde{\ell}^- + X$, it has the value $\sigma_{\rm LO}^{\tilde{\ell}\tilde{\ell}} = 60.680$ fb at LO and $\sigma_{\rm NLO}^{\tilde{\ell}\tilde{\ell}} = 71.354$ fb at NLO. The cross section for $pp \to \tilde{\ell}^+\tilde{\ell}^- j + X$ with the cuts of Eq. (6.3) is $\sigma_{\rm LO}^{\tilde{\ell}\tilde{\ell}j} = 35.009$ fb at LO and $\sigma_{\rm NLO}^{\tilde{\ell}\tilde{\ell}j} = 39.076$ fb at NLO.

Slepton distributions illustrate the impact of next-to-leading order corrections and the matching to parton showers. We show in Fig. 6.5 the transverse momentum distribution of the negatively charged slepton, in Fig. 6.6 the pseudorapidity distribution of this slepton, and in Fig. 6.7 the invariant mass of the slepton pair as obtained with our codes for $pp \to \tilde{\ell}^+\tilde{\ell}^- + X$ and $pp \to \tilde{\ell}^+\tilde{\ell}^- j + X$ at LO, NLO and NLO matched to parton showers (PWG+PYT). The distributions for $pp \to \tilde{\ell}^+\tilde{\ell}^- + X$ are totally inclusive. For $pp \to \tilde{\ell}^+\tilde{\ell}^- j + X$, the jet cuts of Eq. (6.3) are imposed. In the lower panels of the plots, the ratio of the NLO to the LO distributions is given. While the next-to-leading order corrections are sizeable for $pp \to \tilde{\ell}^+\tilde{\ell}^- + X$, the parton shower does hardly affect the color neutral sleptons. In the case of $pp \to \tilde{\ell}^+\tilde{\ell}^- j + X$, the parton shower modifies the transverse momentum distribution of the hardest jet, changing the number of events that pass the jet cut.

A detailed comparison of jet distributions in the heavy slepton setup is given in Figs. 6.8 - 6.10. In all of these plots, the cuts of Eq. (6.3) are applied. The transverse momentum distribution of the hardest jet at fixed next-to-leading order and after the matching to parton showers is shown in Fig. 6.8 (a), both for $pp \to \tilde{\ell}^+\tilde{\ell}^- + X$ and for $pp \to \tilde{\ell}^+\tilde{\ell}^- j + X$. With the NLO corrections of the hardest jet included in $pp \to \tilde{\ell}^+\tilde{\ell}^- j + X$, the emission at low transverse momenta is enhanced, while the emission of very hard jets is reduced.

To provide an estimate of the scale dependence of the hardest jet, we look at its $p_{\rm T}$ distribution in Fig. 6.9 for different choices of the renormalization scale μ_R and the factorization scale μ_F. The spread of this distribution in an independent scale varia-

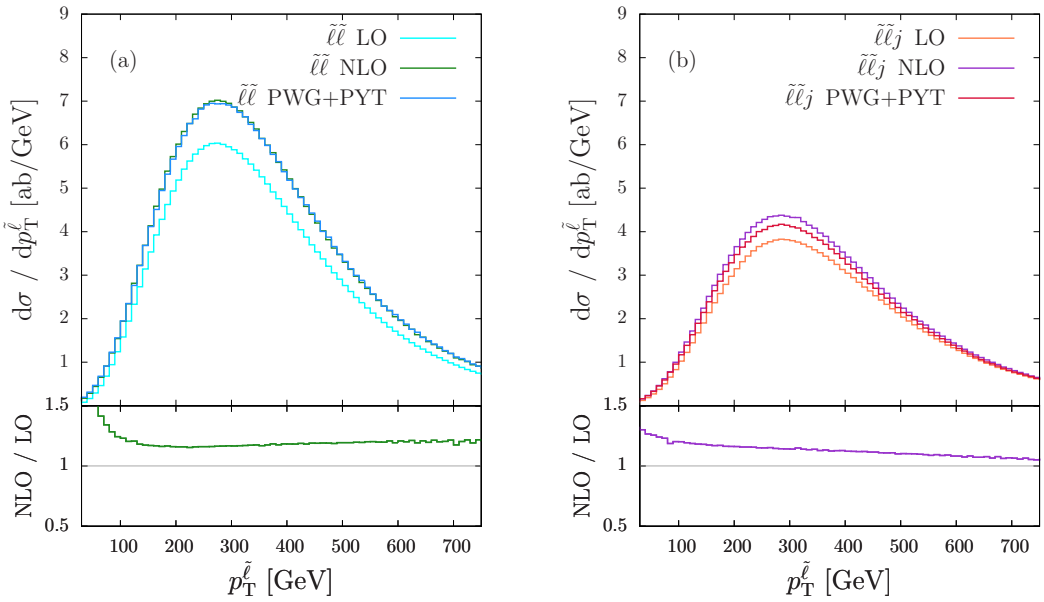

Figure 6.5: Transverse momentum distribution of the negatively charged slepton with $m_{\tilde{\ell}} = 350$ GeV in $pp \to \tilde{\ell}^+\tilde{\ell}^- + X$ without cuts (a) at LO (cyan), NLO (green), and matched to parton showers (blue) and in $pp \to \tilde{\ell}^+\tilde{\ell}^- j + X$ with the cuts of Eq. (6.3) (b) at LO (orange), NLO (purple), and matched to parton showers (red). The ratios of the NLO to the LO distributions are given in the lower panels.

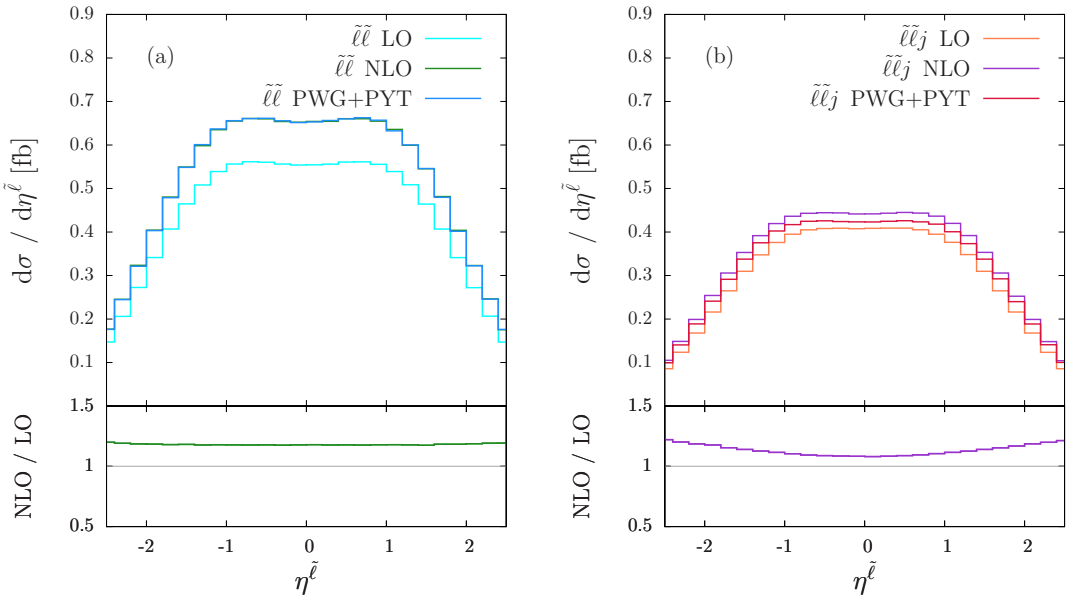

Figure 6.6: Pseudorapidity distribution of the negatively charged slepton with $m_{\tilde{\ell}} = 350$ GeV in $pp \to \tilde{\ell}^+\tilde{\ell}^- + X$ without cuts (a) at LO (cyan), NLO (green), and matched to parton showers (blue) and in $pp \to \tilde{\ell}^+\tilde{\ell}^- j + X$ with the cuts of Eq. (6.3) (b) at LO (orange), NLO (purple), and matched to parton showers (red). The ratios of the NLO to the LO distributions are given in the lower panels.

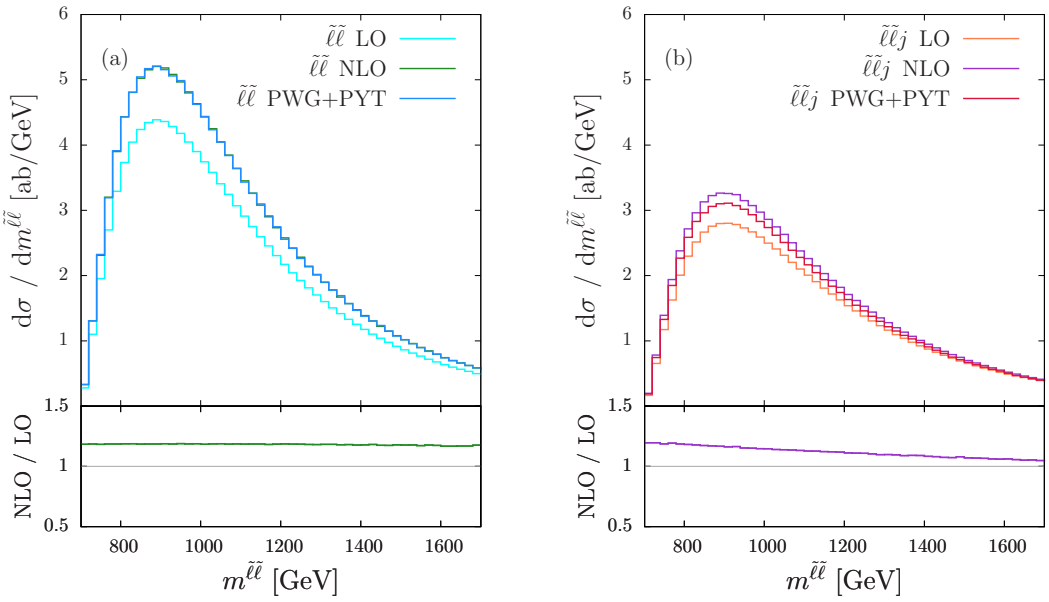

Figure 6.7: Invariant mass distribution of the slepton pair with $m_{\tilde{\ell}} = 350$ GeV in $pp \to \tilde{\ell}^+\tilde{\ell}^- + X$ without cuts (a) at LO (cyan), NLO (green), and matched to parton showers (blue) and in $pp \to \tilde{\ell}^+\tilde{\ell}^- j + X$ with the cuts of Eq. (6.3) (b) at LO (orange), NLO (purple), and matched to parton showers (red). The ratios of the NLO to the LO distributions are given in the lower panels.

tion according to $0.5 \leq \xi_R, \xi_F \leq 2$ is represented by bands for $pp \to \tilde{\ell}^+\tilde{\ell}^- + X$ and $pp \to \tilde{\ell}^+\tilde{\ell}^- j + X$ at NLO with the cuts of Eq. (6.3) respectively. While a large scale dependence in $pp \to \tilde{\ell}^+\tilde{\ell}^- + X$ is found, the inclusion of perturbative corrections for the hardest jet in $pp \to \tilde{\ell}^+\tilde{\ell}^- j + X$ leads to a notable reduction of the scale dependence for this observable.

The second hardest jet in $pp \to \tilde{\ell}^+\tilde{\ell}^- + X$ can only be produced via the parton shower. In Fig. 6.8 (b), we compare the transverse momentum distribution of this jet to the transverse momentum distribution of the second hardest jet in $pp \to \tilde{\ell}^+\tilde{\ell}^- j + X$ at NLO, which is generated by the real-emission corrections, and to the transverse momentum distribution of the second hardest jet in $pp \to \tilde{\ell}^+\tilde{\ell}^- j + X$ after the matching to parton showers. Significant differences between the matched distributions are found in the hard region, which lies beyond the range of validity of the parton shower approximation. The inclusion of fixed-order matrix elements for the second hardest jet leads to an increased production rate in the hard region. Comparing the fixed-order NLO prediction to the matched prediction from `POWHEG+PYTHIA` in $pp \to \tilde{\ell}^+\tilde{\ell}^- j + X$, the Sudakov suppression in the parton shower at low transverse momenta becomes evident.

Pseudorapidity distributions of the hardest jet are displayed in Fig. 6.10 (a) in the case of $pp \to \tilde{\ell}^+\tilde{\ell}^- + X$ and in Fig. 6.10 (b) for $pp \to \tilde{\ell}^+\tilde{\ell}^- j + X$. In $pp \to \tilde{\ell}^+\tilde{\ell}^- + X$, the parton shower increases the production of hard central jets compared to the fixed-order NLO result. While the overall cross section in $pp \to \tilde{\ell}^+\tilde{\ell}^- j + X$ decreases after the combination with parton showers, the production of central jets is again favored.

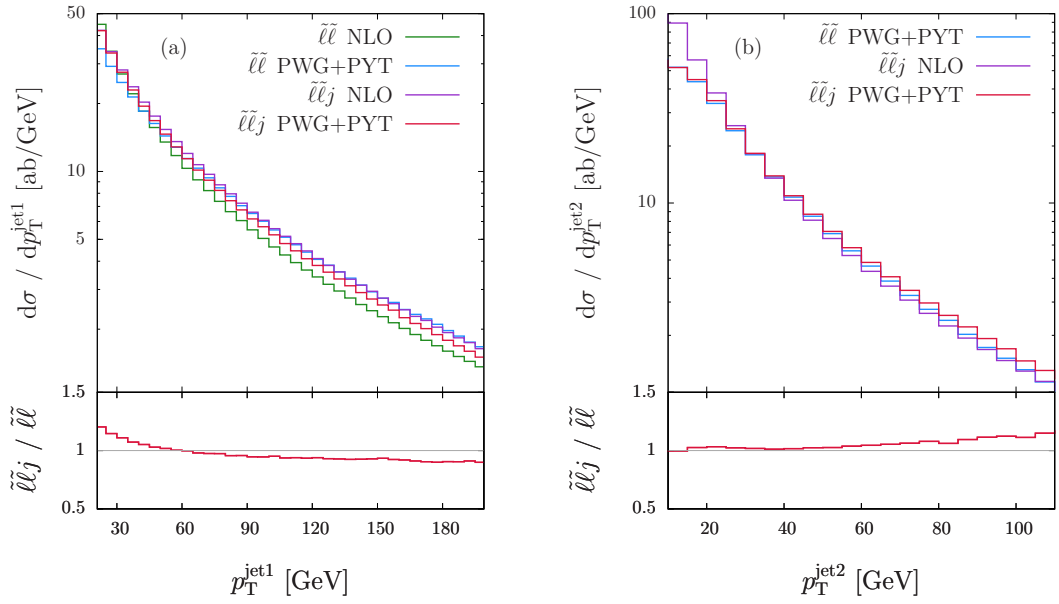

Figure 6.8: Transverse momentum distribution of the hardest jet (a) and the second hardest jet (b) in the heavy slepton setup with the cuts of Eq. (6.3) as obtained with $pp \to \tilde{\ell}^+\tilde{\ell}^- + X$ at NLO (green, a), $pp \to \tilde{\ell}^+\tilde{\ell}^- + X$ matched to parton showers (blue), $pp \to \tilde{\ell}^+\tilde{\ell}^- j + X$ at NLO (purple), and $pp \to \tilde{\ell}^+\tilde{\ell}^- j + X$ matched to parton showers (red). The ratios of the distributions for $pp \to \tilde{\ell}^+\tilde{\ell}^- j + X$ and $pp \to \tilde{\ell}^+\tilde{\ell}^- + X$ after the matching to parton showers are given in the lower panels.

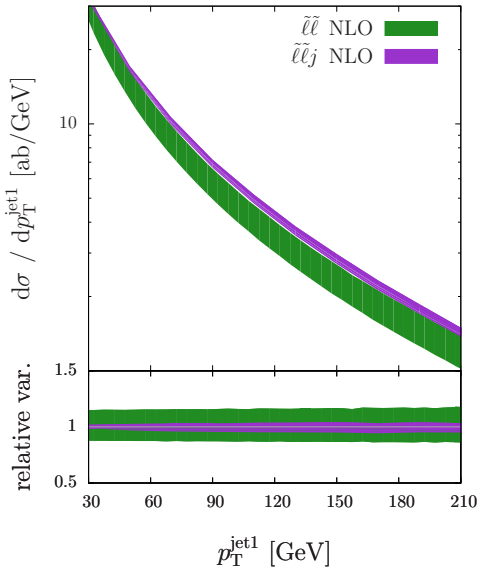

Figure 6.9: Transverse momentum distribution of the hardest jet at NLO with the cuts of Eq. (6.3) in $pp \to \tilde{\ell}^+\tilde{\ell}^- + X$ (green) and in $pp \to \tilde{\ell}^+\tilde{\ell}^- j + X$ (purple). The bands correspond to the independent variation of ξ_R and ξ_F in the range $0.5 \leq \xi_R, \xi_F \leq 2$. In the lower panel, the scale variation bands normalized to the central scale choice $\xi_R = \xi_F = 1$ are given.

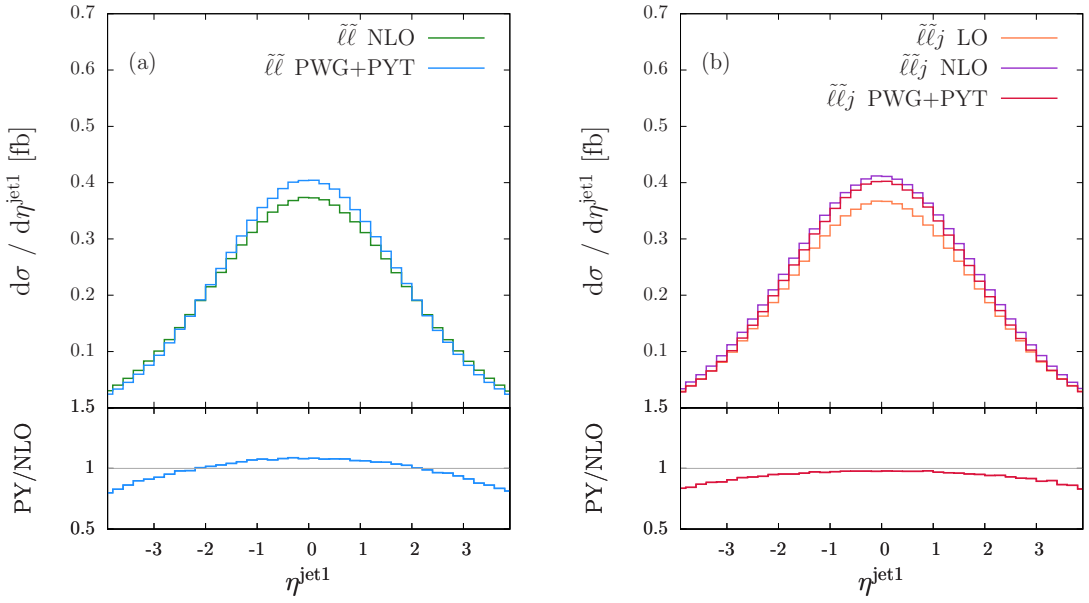

Figure 6.10: Pseudorapidity distribution of the hardest jet in the heavy slepton setup with the cuts of Eq. (6.3) in $pp \to \tilde{\ell}^+\tilde{\ell}^- + X$ (a) at NLO (green), matched to parton showers (blue) and in $pp \to \tilde{\ell}^+\tilde{\ell}^- j + X$ (b) at LO (orange), NLO (purple), and matched to parton showers (red). The ratios of the distributions after the matching with parton showers to the fixed-order NLO distributions are given in the lower panels.

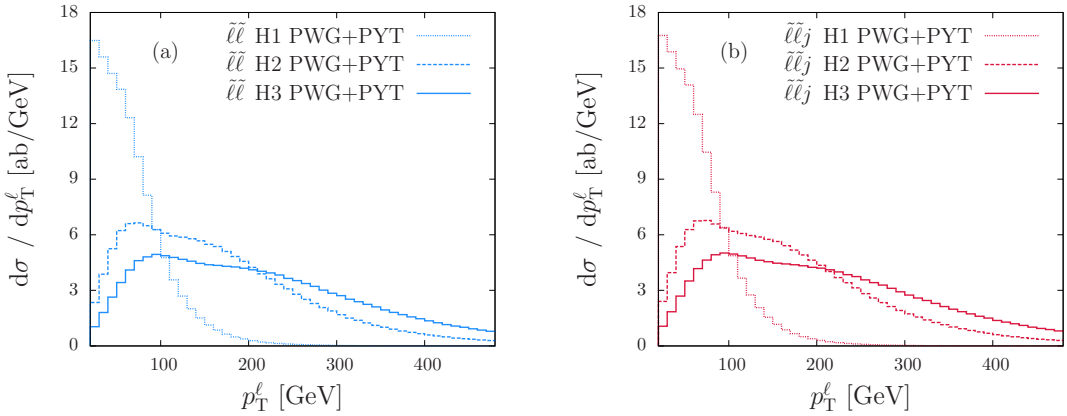

Figure 6.11: Transverse momentum distribution of the negatively charged lepton in $pp \to \tilde{\ell}^+\tilde{\ell}^- + X$ with the cuts of Eqs. (6.2) and (6.4) (a, blue) and in $pp \to \tilde{\ell}^+\tilde{\ell}^- j + X$ with the cuts of Eqs. (6.2) - (6.4) (b, red), both simulated with `POWHEG+PYTHIA`, for setups H1 (dotted), H2 (dashed), and H3 (solid).

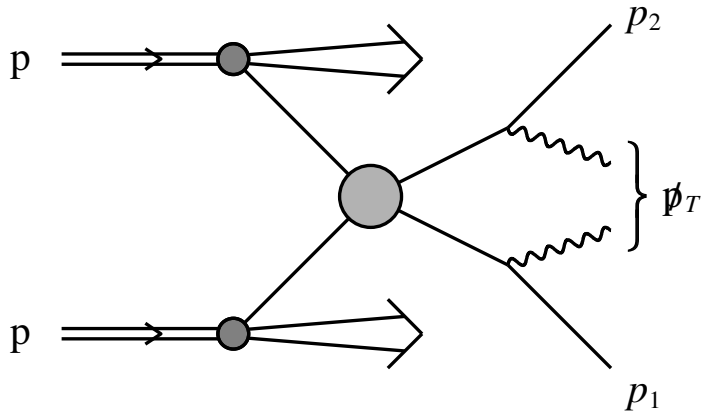

Figure 6.12: Pair production of heavy particles with identical semi-invisible decays in a hadronic collision. Figure taken from [166].

The supersymmetric mass spectrum in our setups is chosen so that a slepton $\tilde{\ell}$ decays only into the corresponding lepton ℓ and the lightest neutralino $\tilde{\chi}_1^0$, which is the stable LSP and escapes undetected. We present in Fig. 6.11 the transverse momentum distribution of the negatively charged lepton for the setups H1, H2, and H3 in $pp \to \tilde{\ell}^+\tilde{\ell}^- + X$ with the cuts of Eqs. (6.2) and (6.4) and in $pp \to \tilde{\ell}^+\tilde{\ell}^- j + X$ with the cuts of Eqs. (6.2) - (6.4). Different neutralino masses $m_{\tilde{\chi}_1^0}$ in these setups lead to pronounced modifications in the shape of this distribution. Especially almost degenerate setups like H1, where only relatively soft leptons are produced, are challenging due to large SM backgrounds.

6.3.1 Mass Extraction with m_{T2}

The kinematical variable m_{T2} [166], also known as 'stransverse' mass, is designed to extract the mass difference between particles that are produced in pairs in a hadronic collision, and their decay products in a semi-invisible decay. It has been used as a central tool for the separation of signal and background in the ATLAS slepton searches [8, 9].

The topological structure of the process for which m_{T2} was developed is shown in Fig. 6.12. It directly matches our setup for a slepton pair $\tilde{\ell}\tilde{\ell}$ that originates from a hadronic collision, where both sleptons decay into an effectively massless visible lepton ℓ and a massive invisible lightest neutralino $\tilde{\chi}_1^0$. If the neutralinos were observable, a lower bound on the slepton mass $m_{\tilde{\ell}}$ could be set for a given neutralino mass $m_{\tilde{\chi}_1^0}$ according to

$$m_{\tilde{\ell}}^2 \geq m_{\mathrm{T}}^2\left(p_{\mathrm{T}}^{\ell}, p_{\mathrm{T}}^{\tilde{\chi}_1^0}\right) \equiv m_{\tilde{\chi}_1^0}^2 + 2\left(E_{\mathrm{T}}^{\ell} E_{\mathrm{T}}^{\tilde{\chi}_1^0} - p_{\mathrm{T}}^{\ell} \cdot p_{\mathrm{T}}^{\tilde{\chi}_1^0}\right), \tag{6.6}$$

where p_{T}^{ℓ} and $p_{\mathrm{T}}^{\tilde{\chi}_1^0}$ are the transverse momenta of a lepton and a neutralino that emerge from the same slepton, and $E_{\mathrm{T}} = \sqrt{p_{\mathrm{T}}^2 + m^2}$. However, since only the sum $\not{p}_{\mathrm{T}}$ of all missing transverse momenta can be observed, it is necessary to take the minimum over all possibilities for the neutralino transverse momenta $\not{q}_{\mathrm{T}}^a, \not{q}_{\mathrm{T}}^b$ that add up to the observed

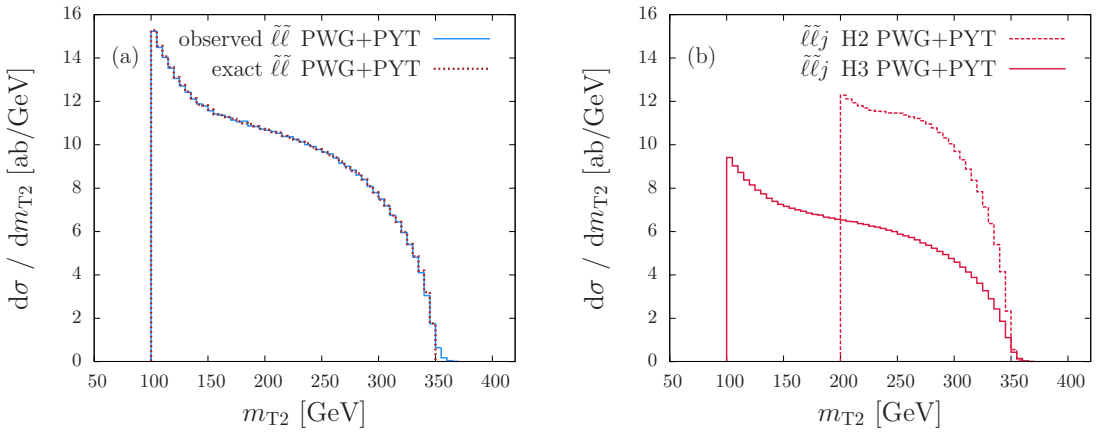

Figure 6.13: Distribution of m_{T2} for $pp \to \tilde{\ell}^+\tilde{\ell}^- + X$ in the setup H3 with the cuts of Eqs. (6.2) and (6.4) (a) based on the unobservable neutralino momenta (brown) or on the observable particles (blue). Distribution of m_{T2} for $pp \to \tilde{\ell}^+\tilde{\ell}^- j + X$ with the cuts of Eqs. (6.2) - (6.4) (b, red) in setup H2 (dashed) and setup H3 (solid).

value. This leads to the definition of m_{T2} as

$$m_{\mathrm{T2}}^2 \equiv \min_{\not{p}_{\mathrm{T}}^a + \not{p}_{\mathrm{T}}^b = \not{p}_{\mathrm{T}}} \left[\max \left[m_{\mathrm{T}}^2 \left(p_{\mathrm{T}}^{\ell^-}, \not{p}_{\mathrm{T}}^a \right), m_{\mathrm{T}}^2 \left(p_{\mathrm{T}}^{\ell^+}, \not{p}_{\mathrm{T}}^b \right) \right] \right]. \tag{6.7}$$

For a given neutralino mass, the distribution of m_{T2} has a lower edge at $m_{\tilde{\chi}_1^0}$ and an upper edge at $m_{\tilde{\ell}}$. If the unknown neutralino mass is removed from Eq. (6.6), the distribution of m_{T2} extends from zero up to $(m_{\tilde{\ell}}^2 - m_{\tilde{\chi}_1^0}^2)^{\frac{1}{2}}$. To determine m_{T2}, a minimization procedure is necessary due to the unknown momenta of the invisible particles from the decays. An efficient algorithm for this procedure was proposed in [72] together with a corresponding code, that we use in our analyses. Due to experimental limitations in the observation of soft radiation, the measured missing transverse momentum does not exactly match the sum of neutralino transverse momenta. We account for this limitation in our analysis by constructing the missing transverse momentum as the vector that balances the vectorial sum over the transverse momenta of all observed objects, which fulfill the requirements of Eq. (6.2) for leptons and of Eq. (6.3) for jets. This inaccuracy in the determination of the missing transverse momentum leads to a widening of the m_{T2} distribution around the slepton mass, so that there is no longer a sharp upper edge at $m_{\tilde{\ell}}$, as illustrated in Fig. 6.13 (a) by comparison to a distribution based on the exact sum of neutralino transverse momenta.

Even with this limitation, the width of the m_{T2} distribution provides a very good estimate for the mass splitting between slepton and neutralino. A comparison of the distributions for $pp \to \tilde{\ell}^+\tilde{\ell}^- j + X$ with the cuts of Eqs. (6.2) - (6.4) in the setups H2 and H3 demonstrates this distinctive power of m_{T2}, see Fig. 6.13 (b). However, for small mass splittings between the slepton and the neutralino, m_{T2} is not very effective in separating the signal from Standard Model backgrounds. For example, the features of $pp \to W^+W^- + X$ with leptonic decays $W^+W^- \to \ell^+\nu\ell^-\overline{\nu}$ closely resemble those of slepton pair production, but the total cross section is much larger. The m_{T2} distribution of this background process extends up to the mass of the W boson, so that every signal below this scale is hard to extract due to large background noise.

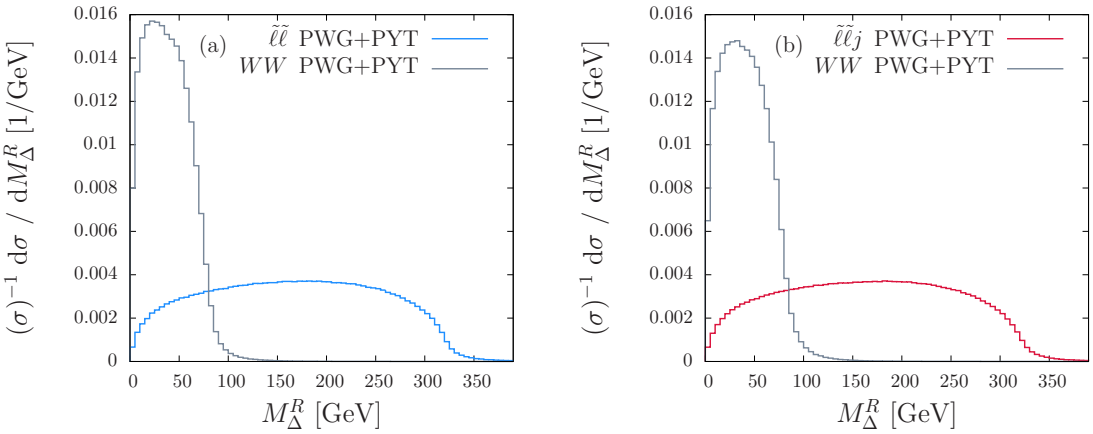

Figure 6.14: Normalized distribution of the super-razor variable M_Δ^R for $pp \to \tilde{\ell}^+\tilde{\ell}^- + X$ (blue) and the background $pp \to W^+W^- + X$ (gray) in the setup H3 with the cuts of Eqs. (6.2) and (6.4) (a) and the normalized distribution of M_Δ^R for $pp \to \tilde{\ell}^+\tilde{\ell}^- j + X$ (red) compared to $pp \to W^+W^- + X$ (gray) in the setup H3 with the cuts of Eqs. (6.2) - (6.4) (b).

6.3.2 Razor Variables

The razor approach uses approximate boosts to specific kinematic frames in the pair production process depicted in Fig. 6.12 to extract information that allows to separate signal and background. This method was suggested in [196], where the original razor variables were defined. Improved super-razor variables, which use more boosts for a better approximation of the reference frames, were introduced in [58]. In the definition of the super-razor variables, boosts to the center-of-mass frame of the pair-produced particles and to both particle decay frames are considered. CMS used the razor variables in searches [68, 71] for squarks and gluinos. In a comparison [168] of limits on squark pair-production cross sections from razor searches to limits obtained with different techniques, the razor approach turned out to be very competitive.

Two steps lead from the laboratory frame to the razor frame R, an approximation of the slepton pair center-of-mass frame. First, a boost $\vec{\beta}_L$ along the beam axis with magnitude

$$\beta_L = \frac{q_1^z + q_2^z}{E_1 + E_2}, \tag{6.8}$$

where E_i and $\vec{q}_i$ are the observed lepton energies and momenta, takes us to a frame with opposite longitudinal lepton momentum components of equal magnitude. Second, a transverse boost $\vec{\beta}_R$ corrects for the shift of the slepton pair center of mass due to QCD radiation with transverse momentum sum $\vec{J}_T$. The boost direction is opposite to $\vec{J}_T$ and the magnitude is fixed by the prefactor $(|\vec{J}_T|^2 + \hat{s}_R)^{-\frac{1}{2}}$, where $\hat{s}_R$ is the approximate partonic center-of-mass energy, that is obtained using two assumptions: the invariant mass of all visible particles is set equal to the invariant mass of all invisible particles and $\hat{s}_R$ is required to be extremal with respect to longitudinal boosts. All approximations used in the super-razor approach are expected to be valid not for each single event, but for the average over many kinematic configurations.

Using the lepton energies E_{Ri} and momenta $\vec{q}_{Ri}$ in the razor frame R, the super-razor approximations of the slepton decay frames and corresponding Lorentz γ factors are

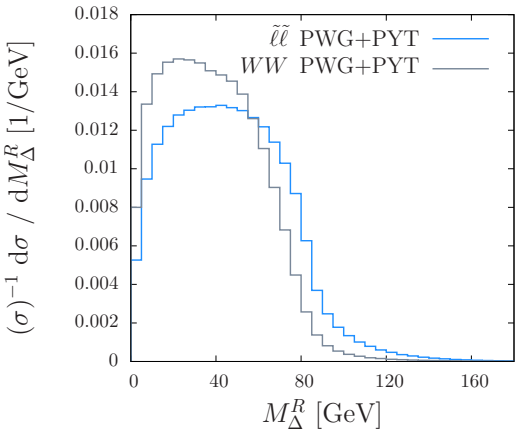

Figure 6.15: Normalized distribution of the super-razor variable M_Δ^R for $pp \to \tilde{\ell}^+\tilde{\ell}^- + X$ in setup H1 (blue) and the background $pp \to W^+W^- + X$ (gray) with the cuts of Eqs. (6.2) and (6.4).

obtained via two opposite boosts $\pm\vec{\beta}_{R+1}$ with

$$\vec{\beta}_{R+1} = \frac{\vec{q}_{R1} - \vec{q}_{R2}}{E_{R1} + E_{R2}} \quad \text{and} \quad \gamma_{R+1} = \frac{1}{\sqrt{1-\beta_{R+1}^2}}. \tag{6.9}$$

Energy and momentum conservation force the effectively massless leptons from the slepton decays to have the fixed energy $M_\Delta/2$ each in the rest frame of their mother slepton, with

$$M_\Delta = \frac{m_{\tilde{\ell}}^2 - m_{\tilde{\chi}_1^0}^2}{m_{\tilde{\ell}}}. \tag{6.10}$$

The super-razor variable

$$M_\Delta^R = \frac{\sqrt{\hat{s}_R}}{2\gamma_{R+1}} \tag{6.11}$$

is designed to extract this specific energy scale. Distributions of M_Δ^R exhibit a pronounced edge at M_Δ, which allows the suppression of backgrounds with the same topology but smaller mass differences. We show the normalized M_Δ^R distributions in the setup H3 compared to the dominant background $pp \to W^+W^- + X$ with leptonic decays of the W bosons for $pp \to \tilde{\ell}^+\tilde{\ell}^- + X$ with the cuts of Eqs. (6.2) and (6.4) in Fig. 6.14 (a) and for $pp \to \tilde{\ell}^+\tilde{\ell}^- j + X$ with the cuts of Eqs. (6.2) - (6.4) in Fig. 6.14 (b). The WW background simulation is based on the corresponding `POWHEG BOX` implementation [175].

Almost mass-degenerate sleptons and neutralinos are particularly challenging configurations in the search for sleptons, since they leave little energy to the leptons in the slepton decays. As long as these soft leptons still can be observed, they provide input for analysis techniques. However, variables like m_{T2} or M_Δ^R, which rely on large mass separations to extract the signal, are no longer useful. For example, the normalized M_Δ^R distribution in setup H1 closely resembles the WW background, as shown in Fig. 6.15. Instead, angular correlations between the leptons from slepton decays can help in the separation of the signal from backgrounds in this soft limit.

The super-razor variable $\Delta\phi_R^\beta$ is defined as the azimuthal difference between the direction of the approximate boost $\vec{\beta}_R$ to the slepton pair center-of-mass frame and the sum of

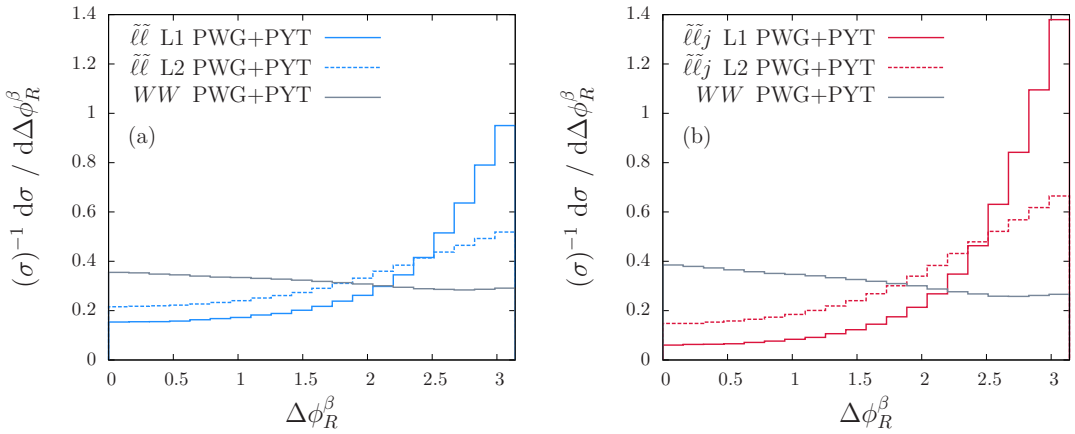

Figure 6.16: Normalized distribution of the super-razor variable $\Delta\phi_R^\beta$ for $pp \to \tilde{\ell}^+\tilde{\ell}^- + X$ (blue) in setups L1 (solid) and L2 (dashed) compared to the background $pp \to W^+W^- + X$ (gray) with the cuts of Eqs. (6.2) and (6.4) (a) and the normalized distribution of $\Delta\phi_R^\beta$ for $pp \to \tilde{\ell}^+\tilde{\ell}^- j + X$ (red) in setups L1 (solid) and L2 (dashed) compared to $pp \to W^+W^- + X$ (gray) with the cuts of Eqs. (6.2) - (6.4) (b).

lepton momenta boosted to this frame. For almost mass-degenerate sleptons and neutralinos, the super-razor boost $\vec{\beta}_R$ systematically exceeds the real boost due to assumptions on the energy splitting between the decay products in the super-razor approach. This feature of the approximate boost leads to an alignment of both leptons opposite to the boost direction, generating a peak in the $\Delta\phi_R^\beta$ distribution around π. In contrast, the background $pp \to W^+W^- + X$ exhibits a rather flat distribution, as shown in Fig. 6.16.

Although the super-razor distributions shown in Figs. 6.14 and 6.16 use different cuts for $pp \to \tilde{\ell}^+\tilde{\ell}^- + X$ and $pp \to \tilde{\ell}^+\tilde{\ell}^- j + X$ because of the presence of one hard jet in the latter, the close resemblance of the distributions in both cases is easy to spot. For a more direct comparison between the super-razor variables simulated in $pp \to \tilde{\ell}^+\tilde{\ell}^- + X$ and in $pp \to \tilde{\ell}^+\tilde{\ell}^- j + X$, we provide in Fig. 6.17 the distributions for M_Δ^R and $\Delta\phi_R^\beta$ with the cuts of Eqs. (6.2) - (6.4) applied to both codes. The stable shape of the super-razor variables in all these distributions confirms their applicability to slepton searches in the presence of hard QCD radiation.

6.3.3 Monojet Analysis

We consider monojet searches as a tool to access slepton pair production without observation of leptons from the slepton decays for almost degenerate masses of the slepton and the lightest neutralino. Monojet searches for electroweak sparticles at the Tevatron were suggested in [127]. The capability of this approach in gaugino searches at the LHC has been considered recently in [136, 203, 30].

We provide distributions for the hardest jet and the missing transverse energy in $pp \to \tilde{\ell}^+\tilde{\ell}^- j + X$ in the almost degenerate setup L1 and compare them to the electronic decay channel $Z \to e^+e^-$ of the dominant background $pp \to Zj + X$. Our background simulation is based on the `POWHEG BOX` implementation of the production of a Z boson in association with a jet [17]. Both electron and positron are considered to be unobservable in our analysis. The cuts of Eq. (6.5) are applied to the hardest jet and to the missing transverse energy, which is composed of the transverse momenta of electron, positron, and

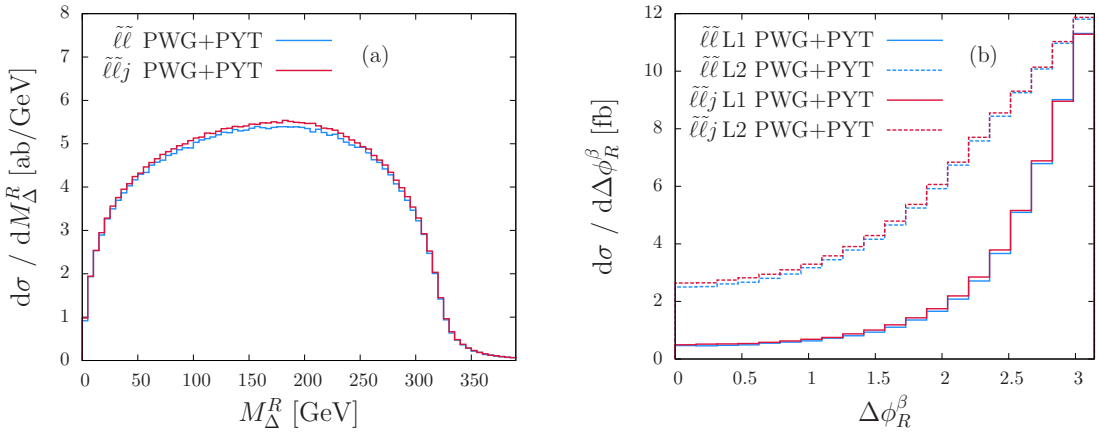

Figure 6.17: Distribution of the super-razor variable M_Δ^R (a) for $pp \to \tilde{\ell}^+\tilde{\ell}^- + X$ (blue) and $pp \to \tilde{\ell}^+\tilde{\ell}^- j + X$ (red) in setup H3 and distribution of the super-razor variable $\Delta\phi_R^\beta$ (b) for $pp \to \tilde{\ell}^+\tilde{\ell}^- + X$ (blue) and $pp \to \tilde{\ell}^+\tilde{\ell}^- j + X$ (red) in the setups L1 (solid) and L2 (dashed), both with the cuts of Eqs. (6.2) - (6.4).

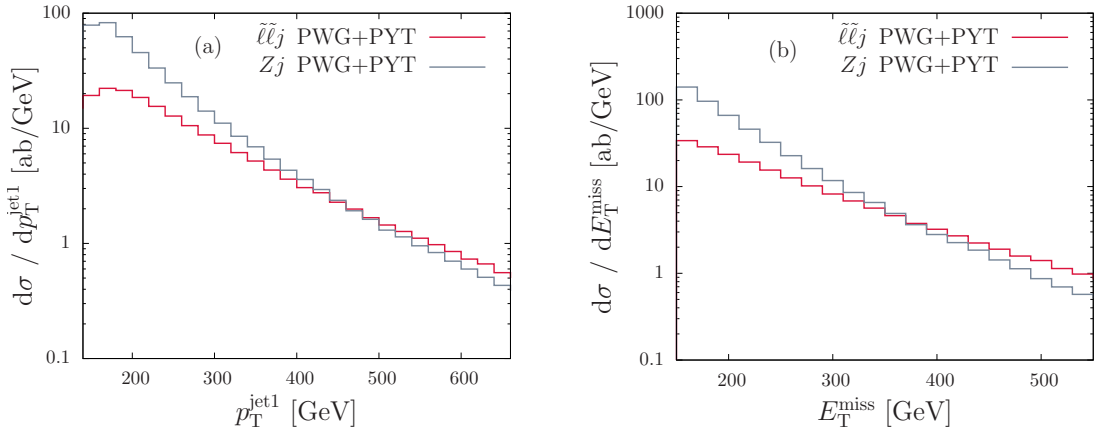

Figure 6.18: Transverse momentum distribution of the hardest jet (a) and missing transverse energy distribution (b) for $pp \to \tilde{\ell}^+\tilde{\ell}^- j + X$ in setup L1 (red) and for the background $pp \to Z(e^+e^-)j + X$ (gray), where the electron and the positron are treated as being invisible, both with the cuts of Eq. (6.5).

additional jets that fail the identification requirements. A complete background simulation would need to take into account all decay channels of the Z boson and other background processes, but our focus lies here on the illustration of the characteristic behavior of signal and background for hard configurations.

Standard Model backgrounds are typically large in soft regions, but in hard tails of suitable distributions, the signal from new heavy particles may exceed the background. In Fig. 6.18 (a), we demonstrate this feature for the transverse momentum distribution of the hardest jet. The same characteristic behavior of signal and background is visible in the missing transverse energy distribution, which is displayed in Fig. 6.18 (b). Therefore, monojet searches are a promising option for discovering sleptons if the splitting between slepton mass and lightest neutralino mass is small.

Chapter 7

Summary and Conclusions

We have implemented two new processes in the POWHEG BOX: slepton pair production and the production of a slepton pair in association with a jet. For both processes, we calculated the respective matrix element at NLO SQCD and provided appropriate phase space parameterizations. Our results were tested against a second independent calculation and against results from the literature.

Both of our programs were used for phenomenological studies at the LHC that respect current experimental exclusion limits. In both processes under consideration, NLO corrections significantly increase the production cross section. While parton showers have little direct impact on the color neutral sleptons, they modify jet distributions, which is particularly important when jet-related cuts are imposed.

In combination with the multi-purpose Monte-Carlo program PYTHIA, our codes can be used for the generation of fully exclusive events and for the simulation of slepton decays. The kinematic information that can be obtained from visible decay products of the sleptons has been used to determine advanced variables that allow to improve the signal significance in the presence of large backgrounds. We looked at the applicability of the stransverse mass m_{T2} and of super-razor variables to different supersymmetric mass scenarios. Mass-related variables were found to be particularly useful for high mass splittings between sleptons and their decay products. Variables that are based on angular correlations possess high discriminative power for small mass splittings.

In almost degenerate scenarios where the direct observation of slepton decay products is not possible, the monojet approach was found to be a promising tool in the search for sleptons. An accurate description of the hardest jet at next-to-leading order matched to parton showers affects soft and hard parts in the distributions of this jet differently. While very hard jet emissions are disfavored in the combination of NLO matrix elements with parton showers compared to LO matrix elements that are supplemented by parton showers, a comparison to one of the dominant Standard Model backgrounds demonstrates that hard tails of signal distributions stand out from rapidly falling background noise. The improved reliability of the jet description at NLO compared to LO results becomes evident in a significant reduction of uncertainties which are related to unphysical scales.

After the restart of the LHC in the next year, unprecedented collision energies will be accessible. Via the combination of experimental improvements with more refined theoretical tools, new regions in supersymmetric parameter space can be probed.

Acknowledgements

First of all, I want to thank my supervisor for offering me the chance to pursue scientific research in the field of particle physics phenomenology. From introductory explanations when I joined her research group until the recent assemblage of last remaining code fragments, she was always encouraging and supportive. Throughout the time that I spent working on this thesis, her guidance and advice have been invaluable to me.

Important contributions to the perturbative calculation of both slepton production processes, that were presented here, and to their implementation as computer programs for the matching to parton showers were made by the third team member of our slepton project. I want to thank him for great collaboration, amazing code work, thorough validations, and many patient explanations.

Experienced colleagues kindly supported our new `POWHEG BOX` implementations and provided important insights into details of this software framework. I am sincerely grateful to them and all authors of the software tools which I used for the work on this thesis.

During my time at Johannes-Gutenberg University (JGU) in Mainz, I had a very supportive environment, both in the group for Theoretical High Energy Physics (THEP) and as fellow of the graduate school 'Symmetry Breaking in Fundamental Interactions' (DFG/GRK 1581). Many colleagues helped me to solve physical and computational problems that arose during my work for this thesis and provided advice concerning possible applications of the new programs. Computing resources at the JGU cluster Mogon, which were granted to me for numerical simulations, and related support by the administrative staff at the Zentrum für Datenverarbeitung (ZDV) were crucial for the generation of several phenomenological results.

Appendix A

Conventions

We use a right-handed system for the laboratory frame coordinates that is centered at the interaction point, like the ATLAS collaboration [9]. The z-axis points along the beam line, the x-axis towards the center of the collider ring, and the y-axis upwards. In spherical coordinates, θ is the polar angle measured from the z-axis and ϕ the azimuth in the x-y plane. The pseudorapidity η is defined as $\eta = \log[\tan(\theta/2)]$.

In so-called natural units, where both $\hbar$, the Planck constant divided by 2π, and the speed of light c have the value one, all physical units can be related to powers of energy. A common energy unit in particle physics is the electronvolt (eV), which refers to the energy difference of an electron after traversing an electric field of one Volt. Recent experiments achieve collision energies in the range of giga electronvolts (GeV $= 10^9$ eV) or tera electronvolts (TeV $= 10^{12}$ eV). Particle production cross sections in these experiments are typically of the order of pico barn (pb $= 10^{-12}$ b) or femto barn (fb $= 10^{-15}$ b), where one barn stands for the area b $= 10^{-28}$ m^2.

We denote by p_1, p_2 the four-momenta of incoming partons and by $p_3, p_4, \ldots$ the four-momenta of outgoing particles. The partonic Mandelstam variables $\hat{s}, \hat{t}, \hat{u}$ stand for Lorentz invariant scalar products of partonic four-momenta:

$$\hat{s} = (p_1 + p_2)^2 \,, \tag{A.1}$$

$$\hat{t} = (p_1 - p_3)^2 \,, \tag{A.2}$$

$$\hat{u} = (p_2 - p_3)^2 \,. \tag{A.3}$$

For processes with more than two outgoing particles, additional generalized Mandelstam variables are defined as

$$\hat{s}_{ij} = (p_i + p_j)^2 \,, \tag{A.4}$$

$$\hat{t}_{ij} = (p_i - p_j)^2 \,. \tag{A.5}$$

Appendix B

Passarino-Veltman Decomposition

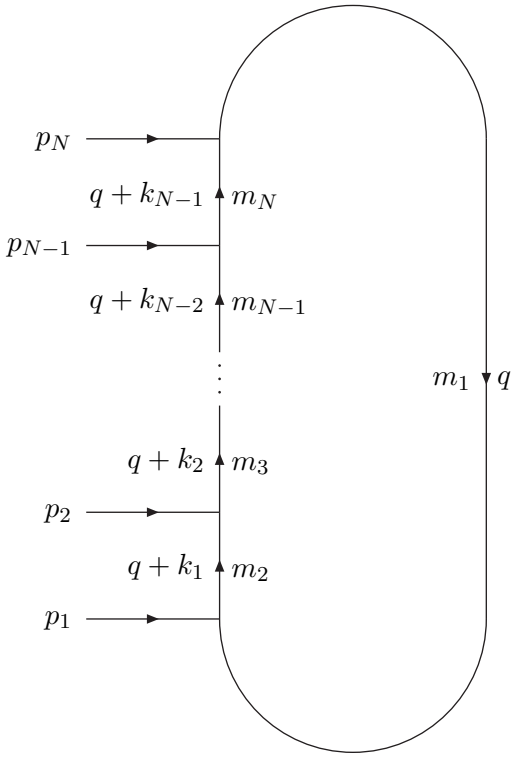

Figure B.1: Momenta and masses in a general one-loop integral.

The decomposition of tensorial integrals according to the Lorentz structures present in the specific case, as suggested by Passarino and Veltman [190], allows to extract all one-loop integrals from loops inside Feynman diagrams in the form of few basic functions, that depend on Lorentz-invariant products of momenta and particle masses. We follow the integral notation of `LoopTools 2.7` [216, 134], denoting a general one-loop integral

$T^N_{\mu_1\dots\mu_t}$ of tensor rank t with N external momenta $p_1,\dots,p_N$ in D dimensions by

$$\begin{aligned} &T^N_{\mu_1\dots\mu_t}(\arg) \\ &= \frac{(2\pi\mu_R)^{(4-D)}}{i\pi^2}\int \mathrm{d}^D q\ \frac{q_{\mu_1}\dots q_{\mu_t}}{\left[q^2-m_1^2\right]\left[(q+k_1)^2-m_2^2\right]\dots\left[(q+k_{N-1})^2-m_N^2\right]} \end{aligned} \tag{B.1}$$

with momenta $k_i = p_1+\dots+p_i$ and masses $m_1,\dots,m_N$ on the propagators in the loop as shown in Fig. B.1. The number of external momenta is usually encoded in alphabetical symbols A for T^1, B for T^2, etc. and scalar integrals are denoted by a subscript 0. All decompositions of tensor integrals according to their Lorentz structure with respect to the momenta k_i and the metric tensor $g^{\mu\nu}$ which are required for our calculations can be found in the following list:

$$B_\mu = k_{1\mu}B_1, \tag{B.2}$$

$$B_{\mu\nu} = g_{\mu\nu}B_{00} + k_{1\mu}k_{1\nu}B_{11}, \tag{B.3}$$

$$C_\mu = \sum_{i=1}^{2} k_{i\mu}C_i, \tag{B.4}$$

$$C_{\mu\nu} = g_{\mu\nu}C_{00} + \sum_{i,j=1}^{2} k_{i\mu}k_{j\nu}C_{ij}, \tag{B.5}$$

$$C_{\mu\nu\rho} = \sum_{i=1}^{2}\left(g_{\mu\nu}k_{i\rho}+g_{\nu\rho}k_{i\mu}+g_{\mu\rho}k_{i\nu}\right)C_{00i} + \sum_{i,j,l=1}^{2} k_{i\mu}k_{j\nu}k_{l\rho}C_{ijl}, \tag{B.6}$$

$$D_\mu = \sum_{i=1}^{3} k_{i\mu}D_i, \tag{B.7}$$

$$D_{\mu\nu} = g_{\mu\nu}D_{00} + \sum_{i,j=1}^{3} k_{i\mu}k_{j\nu}D_{ij}, \tag{B.8}$$

$$D_{\mu\nu\rho} = \sum_{i=1}^{3}\left(g_{\mu\nu}k_{i\rho}+g_{\nu\rho}k_{i\mu}+g_{\mu\rho}k_{i\nu}\right)D_{00i} + \sum_{i,j,l=1}^{3} k_{i\mu}k_{j\nu}k_{l\rho}D_{ijl}, \tag{B.9}$$

$$\begin{aligned} D_{\mu\nu\rho\sigma} = {}& \left(g_{\mu\nu}g_{\rho\sigma}+g_{\mu\rho}g_{\nu\sigma}+g_{\mu\sigma}g_{\nu\rho}\right)D_{0000} \\ &+ \sum_{i,j=1}^{3}\left(g_{\mu\nu}k_{i\rho}k_{j\sigma}+g_{\nu\rho}k_{i\mu}k_{j\sigma}+g_{\mu\rho}k_{i\nu}k_{j\sigma}\right. \\ &\qquad \left.+g_{\mu\sigma}k_{i\nu}k_{j\rho}+g_{\nu\sigma}k_{i\mu}k_{j\rho}+g_{\rho\sigma}k_{i\mu}k_{j\nu}\right)D_{00ij} \\ &+ \sum_{i,j,l,m=1}^{3} k_{i\mu}k_{j\nu}k_{l\rho}k_{m\sigma}D_{ijlm}. \end{aligned} \tag{B.10}$$

After the extraction of all Lorentz structures, the integral coefficients can only depend on scalar products of the momenta attached to the loop and on particle masses. For our

calculations, the arguments arg of the integral coefficients are chosen in the following way:

$$\begin{aligned}
\mathbf{B}: \quad \text{arg} &= \left(p_1^2, m_1^2, m_2^2\right) \\
&= \left(k_1^2, m_1^2, m_2^2\right), \qquad \text{(B.11)} \\
\mathbf{C}: \quad \text{arg} &= \left(p_1^2, p_2^2, (p_1+p_2)^2, m_1^2, m_2^2, m_3^2\right) \\
&= \left(k_1^2, (k_2-k_1)^2, k_2^2, m_1^2, m_2^2, m_3^2\right), \qquad \text{(B.12)} \\
\mathbf{D}: \quad \text{arg} &= \left(p_1^2, p_2^2, p_3^2, p_4^2, (p_1+p_2)^2, (p_2+p_3)^2, m_1^2, m_2^2, m_3^2, m_4^2\right) \\
&= \left(k_1^2, (k_2-k_1)^2, (k_3-k_2)^2, (k_4-k_3)^2, k_2^2, (k_3-k_1)^2, m_1^2, m_2^2, m_3^2, m_4^2\right). \qquad \text{(B.13)}
\end{aligned}$$

Bibliography

[1] http://lepewwg.web.cern.ch/lepewwg/plots/winter2012/.

[2] http://lepsusy.web.cern.ch/lepsusy/welcome.html.

[3] https://atlas.web.cern.ch/atlas/groups/physics/combinedsummaryplots/sm/.

[4] https://twiki.cern.ch/twiki/bin/view/atlaspublic/supersymmetrypublicresults.

[5] https://twiki.cern.ch/twiki/bin/view/cmspublic/physicsresultssus.

[6] ATLAS Collaboration, G. Aad *et al.*, *Observation of a new particle in the search for the Standard Model Higgs boson with the ATLAS detector at the LHC*, Phys.Lett. **B716** (2012) 1–29, [arXiv:1207.7214].

[7] ATLAS Collaboration, G. Aad *et al.*, *Measurements of Higgs boson production and couplings in diboson final states with the ATLAS detector at the LHC*, Phys.Lett. **B726** (2013) 88–119, [arXiv:1307.1427].

[8] ATLAS Collaboration, G. Aad *et al.*, *Search for direct slepton and gaugino production in final states with two leptons and missing transverse momentum with the ATLAS detector in pp collisions at* $\sqrt{s} = 7$ *TeV*, Phys.Lett. **B718** (2013) 879–901, [arXiv:1208.2884].

[9] ATLAS Collaboration, G. Aad *et al.*, *Search for direct production of charginos, neutralinos and sleptons in final states with two leptons and missing transverse momentum in pp collisions at* $\sqrt{s} = 8$ *TeV with the ATLAS detector*, JHEP **1405** (2014) 071, [arXiv:1403.5294].

[10] ALEPH Collaboration, DELPHI Collaboration, L3 Collaboration, OPAL Collaboration, SLD Heavy Flavor Group, Electroweak Group, LEP Electroweak Working Group, SLD Heavy Flavor and Electroweak Group, D. Abbaneo *et al.*, *A Combination of Preliminary Electroweak Measurements and Constraints on the Standard Model*, (2000).

[11] OPAL Collaboration, G. Abbiendi *et al.*, *Search for anomalous production of di-lepton events with missing transverse momentum in* e^+e^- *collisions at* $\sqrt{s} = 183 - 209$ *GeV*, Eur.Phys.J. **C32** (2004) 453–473, [hep-ex/0309014].

[12] DELPHI Collaboration, J. Abdallah *et al.*, *Searches for supersymmetric particles in* e^+e^- *collisions up to 208 GeV and interpretation of the results within the MSSM*, Eur.Phys.J. **C31** (2003) 421–479, [hep-ex/0311019].

[13] L3 Collaboration, P. Achard *et al.*, *Search for scalar leptons and scalar quarks at LEP*, Phys.Lett. **B580** (2004) 37–49, [hep-ex/0310007].

[14] S. Alioli *et al.*, *NLO vector-boson production matched with shower in POWHEG*, JHEP **0807** (2008) 060, [arXiv:0805.4802].

[15] S. Alioli *et al.*, *NLO Higgs boson production via gluon fusion matched with shower in POWHEG*, JHEP **0904** (2009) 002, [arXiv:0812.0578].

[16] S. Alioli *et al.*, *A general framework for implementing NLO calculations in shower Monte Carlo programs: the POWHEG BOX*, JHEP **1006** (2010) 043, [arXiv:1002.2581].

[17] S. Alioli *et al.*, *Vector boson plus one jet production in POWHEG*, JHEP **1101** (2011) 095, [arXiv:1009.5594].

[18] S. Alioli, S.-O. Moch, and P. Uwer, *Hadronic top-quark pair-production with one jet and parton showering*, JHEP **1201** (2012) 137, [arXiv:1110.5251].

[19] B. C. Allanach *et al.*, *SUSY Les Houches Accord 2*, Comput.Phys.Commun. **180** (2009) 8–25, [arXiv:0801.0045].

[20] B. C. Allanach, S. Grab, and H. E. Haber, *Supersymmetric monojets at the Large Hadron Collider*, JHEP **1101** (2011) 138, [arXiv:1010.4261].

[21] G. Altarelli, R. Kleiss, and C. Verzegnassi, *Z Physics at LEP-1. Workshop Proceedings, Vol. 1: Standard Physics*, September 4-5, 1989.

[22] G. Altarelli and G. Parisi, *Asymptotic Freedom in Parton Language*, Nucl.Phys. **B126** (1977) 298–318.

[23] J. Alwall *et al.*, *A standard format for Les Houches Event Files*, Comput.Phys.Commun. **176** (2007) 300–304, [hep-ph/0609017].

[24] J. Alwall *et al.*, *MadGraph/MadEvent v4: the new web generation*, JHEP **0709** (2007) 028, [arXiv:0706.2334].

[25] U. Amaldi, W. de Boer, and H. Fürstenau, *Comparison of grand unified theories with electroweak and strong coupling constants measured at LEP*, Phys.Lett. **B260** (1991) 447–455.

[26] D. Amati *et al.*, *A Treatment of Hard Processes Sensitive to the Infrared Structure of QCD*, Nucl.Phys. **B173** (1980) 429–455.

[27] T. Aoyama, M. Hayakawa, T. Kinoshita, and M. Nio, *Revised value of the eighth-order QED contribution to the anomalous magnetic moment of the electron*, Phys.Rev. **D77** (2008) 053012, [arXiv:0712.2607].

[28] H. Baer *et al.*, *Detecting sleptons at hadron colliders and supercolliders*, Phys.Rev. **D49** (1994) 3283–3290, [hep-ph/9311248].

[29] H. Baer, B. W. Harris, and M. H. Reno, *Next-to-leading order slepton pair production at hadron colliders*, Phys.Rev. **D57** (1998) 5871–5874, [hep-ph/9712315].

[30] H. Baer, A. Mustafayev, and X. Tata, *Monojets and monophotons from light Higgsino pair production at LHC14*, Phys.Rev. **D89** (2014) 055007, [arXiv:1401.1162].

[31] E. Bagnaschi *et al.*, *Higgs production via gluon fusion in the POWHEG approach in the SM and in the MSSM*, JHEP **1202** (2012) 088, [arXiv:1111.2854].

[32] M. Bähr *et al.*, *Herwig++ physics and manual*, Eur.Phys.J. **C58** (2008) 639–707, [arXiv:0803.0883].

[33] D. P. Barber *et al.*, *Experimental Study of Heavy Charged Leptons and Search for Scalar Partners of Muons at PETRA (12 GeV $\leq E_{\text{c.m.}} \leq$ 36.7 GeV)*, Phys.Rev.Lett. **45** (1980) 1904–1907.

[34] W. A. Bardeen *et al.*, *Deep-inelastic scattering beyond the leading order in asymptotically free gauge theories*, Phys.Rev. **D18** (1978) 3998–4017.

[35] JADE Collaboration, W. Bartel *et al.*, *Search for Scalar Muons*, Phys.Lett. **B152** (1985) 392–398.

[36] L. Barzè *et al.*, *Implementation of electroweak corrections in the POWHEG BOX: single W production*, JHEP **1204** (2012) 037, [arXiv:1202.0465].

[37] W. Beenakker *et al.*, *Production of Charginos, Neutralinos, and Sleptons at Hadron Colliders*, Phys.Rev.Lett. **83** (1999) 3780–3783, [hep-ph/9906298].

[38] W. Beenakker, R. Höpker, and M. Spira, *PROSPINO: A program for the production of supersymmetric particles in next-to-leading order QCD*, (1996), [hep-ph/9611232].

[39] CELLO Collaboration, H. J. Behrend *et al.*, *Scalar Lepton Search with the CELLO Detector at PETRA*, Phys.Lett. **B114** (1982) 287–290.

[40] J. Bellm *et al.*, *Herwig++ 2.7 Release Note*, (2013), [arXiv:1310.6877].

[41] M. Bengtsson and T. Sjöstrand, *A Comparative Study of Coherent and Non-coherent Parton Shower Evolution*, Nucl.Phys. **B289** (1987) 810–846.

[42] M. Bengtsson and T. Sjöstrand, *Coherent Parton Showers Versus Matrix Elements - Implications of PETRA/PEP Data*, Phys.Lett. **B185** (1987) 435–440.

[43] M. Bengtsson, T. Sjöstrand, and M. van Zijl, *Initial State Radiation Effects on W and Jet Production*, Z.Phys. **C32** (1986) 67–83.

[44] S. Berge *et al.*, *Supersymmetric QCD one-loop effects in (un)polarized top-pair production at hadron colliders*, Phys.Rev. **D76** (2007) 034016, [hep-ph/0703016].

[45] Particle Data Group, J. Beringer *et al.*, *Review of Particle Physics*, Phys.Rev. **D86** (2012) 010001.

[46] C. Bernaciak and D. Wackeroth, *Combining next-to-leading order QCD and electroweak radiative corrections to W-boson production at hadron colliders in the POWHEG framework*, Phys.Rev. **D85** (2012) 093003, [arXiv:1201.4804].

[47] S. A. Bludman, *On the universal Fermi interaction*, Nuovo Cim. **9** (1958) 433–445.

[48] M. Böhm, A. Denner, and H. Joos, *Gauge Theories of the Strong and Electroweak Interaction*, Teubner, (2001).

[49] C. G. Bollini and J. J. Giambiagi, *Lowest Order "Divergent" Graphs in ν-Dimensional Space*, Phys.Lett. **B40** (1972) 566–568.

[50] E. Boos *et al.*, *Generic User Process Interface for Event Generators*, (2001), [hep-ph/0109068].

[51] G. Bozzi, B. Fuks, and M. Klasen, *Slepton production in polarized hadron collisions*, Phys.Lett. **B609** (2005) 339–350, [hep-ph/0411318].

[52] G. Bozzi, B. Fuks, and M. Klasen, *Transverse-momentum resummation for slepton-pair production at the CERN Large Hadron Collider*, Phys.Rev. **D74** (2006) 015001, [hep-ph/0603074].

[53] G. Bozzi, B. Fuks, and M. Klasen, *Threshold resummation for slepton-pair production at hadron colliders*, Nucl.Phys. **B777** (2007) 157–181, [hep-ph/0701202].

[54] G. Bozzi, B. Fuks, and M. Klasen, *Joint resummation for slepton pair production at hadron colliders*, Nucl.Phys. **B794** (2008) 46–60, [arXiv:0709.3057].

[55] TASSO Collaboration, R. Brandelik *et al.*, *Electroweak Coupling Constants in the Leptonic Reactions $e^+e^- \to e^+e^-$ and $e^+e^- \to \mu^+\mu^-$ and Search for Scalar Leptons*, Phys.Lett. **B117** (1982) 365–371.

[56] A. Broggio, M. Neubert, and L. Vernazza, *Soft-gluon resummation for slepton-pair production at hadron colliders*, JHEP **1205** (2012) 151, [arXiv:1111.6624].

[57] A. Buckley *et al.*, *General-purpose event generators for LHC physics*, Phys.Rept. **504** (2011) 145–233, [arXiv:1101.2599].

[58] M. R. Buckley *et al.*, *Super-razor and searches for sleptons and charginos at the LHC*, Phys.Rev. **D89** (2014) 055020, [arXiv:1310.4827].

[59] M. Cacciari and G. P. Salam, *Dispelling the N^3 myth for the k_t jet-finder*, Phys.Lett. **B641** (2006) 57–61, [hep-ph/0512210].

[60] M. Cacciari, G. P. Salam, and G. Soyez, *The anti-k_t jet clustering algorithm*, JHEP **0804** (2008) 063, [arXiv:0802.1189].

[61] M. Cacciari, G. P. Salam, and G. Soyez, *FastJet user manual*, Eur.Phys.J. **C72** (2012) 1896, [arXiv:1111.6097].

[62] J. M. Campbell *et al.*, *NLO Higgs boson production plus one and two jets using the POWHEG BOX, MadGraph4 and MCFM*, JHEP **1207** (2012) 092, [arXiv:1202.5475].

[63] J. M. Campbell *et al.*, *W and Z bosons in association with two jets using the POWHEG method*, JHEP **1308** (2013) 005, [arXiv:1303.5447].

[64] S. Catani *et al.*, *New clustering algorithm for multijet cross sections in e^+e^- annihilation*, Phys.Lett. **B269** (1991) 432–438.

[65] S. Catani *et al.*, *Longitudinally-invariant $k_\perp$-clustering algorithms for hadron-hadron collisions*, Nucl.Phys. **B406** (1993) 187–224.

[66] S. Catani and M. H. Seymour, *The dipole formalism for the calculation of QCD jet cross sections at next-to-leading order*, Phys.Lett. **B378** (1996) 287–301, [hep-ph/9602277].

[67] S. Catani and M. H. Seymour, *A general algorithm for calculating jet cross sections in NLO QCD*, Nucl.Phys. **B485** (1997) 291–419, [hep-ph/9605323].

[68] CMS Collaboration, S. Chatrchyan *et al.*, *Inclusive search for squarks and gluinos in pp collisions at $\sqrt{s} = 7$ TeV*, Phys.Rev. **D85** (2012) 012004, [arXiv:1107.1279].

[69] CMS Collaboration, S. Chatrchyan *et al.*, *Observation of a new boson at a mass of 125 GeV with the CMS experiment at the LHC*, Phys.Lett. **B716** (2012) 30–61, [arXiv:1207.7235].

[70] CMS Collaboration, S. Chatrchyan *et al.*, *Measurement of the properties of a Higgs boson in the four-lepton final state*, Phys.Rev. **D89** (2014) 092007, [arXiv:1312.5353].

[71] CMS Collaboration, S. Chatrchyan *et al.*, *Search for supersymmetry with razor variables in pp collisions at $\sqrt{s} = 7$ TeV*, (2014), [arXiv:1405.3961].

[72] H.-C. Cheng and Z. Han, *Minimal kinematic constraints and m_{T2}*, JHEP **0812** (2008) 063, [arXiv:0810.5178].

[73] S. R. Coleman and J. Mandula, *All Possible Symmetries of the S Matrix*, Phys.Rev. **159** (1967) 1251–1256.

[74] J. C. Collins, *Renormalization: An Introduction to Renormalization, the Renormalization Group and the Operator-Product Expansion*, Cambridge University Press, (1984).

[75] J. C. Collins, *Foundations of Perturbative QCD*, Cambridge University Press, (2011).

[76] J. C. Collins, D. E. Soper, and G. F. Sterman, *Factorization of Hard Processes in QCD*, Adv.Ser.Direct.High En.Phys. **5** (1988) 1–91, [hep-ph/0409313].

[77] J. C. Collins, F. Wilczek, and A. Zee, *Low-energy manifestations of heavy particles: Application to the neutral current*, Phys.Rev. **D18** (1978) 242–247.

[78] G. Corcella *et al.*, *HERWIG 6: an event generator for hadron emission reactions with interfering gluons (including supersymmetric processes)*, JHEP **0101** (2001) 010, [hep-ph/0011363].

[79] G. Corcella *et al.*, *HERWIG 6.5 Release Note*, (2002), [hep-ph/0210213].

[80] G. Curci, W. Furmanski, and R. Petronzio, *Evolution of parton densities beyond leading order: The non-singlet case*, Nucl.Phys. **B175** (1980) 27–92.

[81] P. Cvitanović, *Group theory for Feynman diagrams in non-Abelian gauge theories*, Phys.Rev. **D14** (1976) 1536–1553.

[82] S. Dawson, E. Eichten, and C. Quigg, *Search for supersymmetric particles in hadron-hadron collisions*, Phys.Rev. **D31** (1985) 1581–1637.

[83] F. del Aguila and L. Ametller, *On the detectability of sleptons at large hadron colliders*, Phys.Lett. **B261** (1991) 326–333.

[84] A. Denner, *Techniques for the Calculation of Electroweak Radiative Corrections at the One-Loop Level and Results for W-physics at LEP200*, Fortschr.Phys. **41** (1993) 307–420, [arXiv:0709.1075].

[85] A. Denner and S. Dittmaier, *Reduction of one-loop tensor 5-point integrals*, Nucl.Phys. **B658** (2003) 175–202, [hep-ph/0212259].

[86] MSSM Working Group, A. Djouadi *et al.*, *The Minimal Supersymmetric Standard Model: Group Summary Report*, (1998), [hep-ph/9901246].

[87] Y. L. Dokshitzer, *Calculation of the Structure Functions for Deep Inelastic Scattering and e^+e^- Annihilation by Perturbation Theory in Quantum Chromodynamics.*, Sov.Phys.JETP **46** (1977) 641–653.

[88] Y. L. Dokshitzer *et al.*, *Better Jet Clustering Algorithms*, JHEP **9708** (1997) 001, [hep-ph/9707323].

[89] S. D. Drell and T.-M. Yan, *Massive Lepton-Pair Production in Hadron-Hadron Collisions at High Energies*, Phys.Rev.Lett. **25** (1970) 316–320.

[90] E. Eichten *et al.*, *Supercollider physics*, Rev.Mod.Phys. **56** (1984) 579–707.

[91] J. R. Ellis, S. Kelley, and D. V. Nanopoulos, *Probing the desert using gauge coupling unification*, Phys.Lett. **B260** (1991) 131–137.

[92] R. K. Ellis and G. Zanderighi, *Scalar one-loop integrals for QCD*, JHEP **0802** (2008) 002, [arXiv:0712.1851].

[93] S. D. Ellis and D. E. Soper, *Successive combination jet algorithm for hadron collisions*, Phys.Rev. **D48** (1993) 3160–3166, [hep-ph/9305266].

[94] F. Englert and R. Brout, *Broken Symmetry and the Mass of Gauge Vector Mesons*, Phys.Rev.Lett. **13** (1964) 321–323.

[95] L. D. Faddeev and V. N. Popov, *Feynman Diagrams for the Yang-Mills Field*, Phys.Lett. **B25** (1967) 29–30.

[96] G. R. Farrar and P. Fayet, *Bounds on R-Hadron Production from Calorimetry Experiments*, Phys.Lett. **B79** (1978) 442–446.

[97] G. R. Farrar and P. Fayet, *Phenomenology of the Production, Decay, and Detection of New Hadronic States Associated with Supersymmetry*, Phys.Lett. **B76** (1978) 575–579.

[98] P. Fayet, *Supersymmetry and Weak, Electromagnetic and Strong Interactions*, Phys.Lett. **B64** (1976) 159–162.

[99] P. Fayet, *Mixing Between Gravitational and Weak Interactions Through the Massive Gravitino*, Phys.Lett. **B70** (1977) 461–464.

[100] P. Fayet, *Spontaneously Broken Supersymmetric Theories of Weak, Electromagnetic and Strong Interactions*, Phys.Lett. **B69** (1977) 489–494.

[101] R. Flume, *From $N = 1$ to $N = 4$ Extended Supersymmetric Yang-Mills Fields in a Covariant Wess-Zumino Gauge*, Nucl.Phys. **B217** (1983) 531–543.

[102] S. Frixione, *A general approach to jet cross sections in QCD*, Nucl.Phys. **B507** (1997) 295–314, [hep-ph/9706545].

[103] S. Frixione, Z. Kunszt, and A. Signer, *Three-jet cross sections to next-to-leading order*, Nucl.Phys. **B467** (1996) 399–442, [hep-ph/9512328].

[104] S. Frixione, P. Nason, and C. Oleari, *Matching NLO QCD computations with parton shower simulations: the POWHEG method*, JHEP **0711** (2007) 070, [arXiv:0709.2092].

[105] S. Frixione, P. Nason, and G. Ridolfi, *A positive-weight next-to-leading-order Monte Carlo for heavy flavour hadroproduction*, JHEP **0709** (2007) 126, [arXiv:0707.3088].

[106] S. Frixione, P. Nason, and B. R. Webber, *Matching NLO QCD and parton showers in heavy flavour production*, JHEP **0308** (2003) 007, [hep-ph/0305252].

[107] S. Frixione and B. R. Webber, *Matching NLO QCD computations and parton shower simulations*, JHEP **0206** (2002) 029, [hep-ph/0204244].

[108] B. Fuks *et al.*, *Precision predictions for electroweak superpartner production at hadron colliders with RESUMMINO*, Eur.Phys.J. **C73** (2013) 2480, [arXiv:1304.0790].

[109] B. Fuks *et al.*, *Revisiting slepton pair production at the Large Hadron Collider*, JHEP **1401** (2014) 168, [arXiv:1310.2621].

[110] R. Gavin *et al.*, *Matching squark pair production at NLO with parton showers*, JHEP **1310** (2013) 187, [arXiv:1305.4061].

[111] R. Gavin *et al.*, *Squark Production and Decay matched with Parton Showers at NLO*, (2014), [arXiv:1407.7971].

[112] L. Girardello and M. T. Grisaru, *Soft Breaking of Supersymmetry*, Nucl.Phys. **B194** (1982) 65–76.

[113] C. Giunti, C. W. Kim, and U. W. Lee, *Running Coupling Constants and Grand Unification Models*, Mod.Phys.Lett. **A6** (1991) 1745–1755.

[114] L. D. Gladney *et al.*, *Search for Supersymmetric Electrons*, Phys.Rev.Lett. **51** (1983) 2253–2256.

[115] S. L. Glashow, *Partial-Symmetries of Weak Interactions*, Nucl.Phys. **22** (1961) 579–588.

[116] S. L. Glashow, J. Iliopoulos, and L. Maiani, *Weak Interactions with Lepton-Hadron Symmetry*, Phys.Rev. **D2** (1970) 1285–1292.

[117] T. Gleisberg *et al.*, *Event generation with SHERPA 1.1*, JHEP **0902** (2009) 007, [arXiv:0811.4622].

[118] H. Goldberg, *Constraint on the Photino Mass from Cosmology*, Phys.Rev.Lett. **50** (1983) 1419–1422.

[119] Y. A. Golfand and E. P. Likhtman, *Extension of the Algebra of Poincare Group Generators and Violation of P Invariance*, JETP Lett. **13** (1971) 323–326.

[120] E. Gramstad, *Searches for Supersymmetry in di-Lepton Final States with the ATLAS Detector at $\sqrt{s} = 7$ TeV*, Dissertation, Oslo, 2013.

[121] V. N. Gribov and L. N. Lipatov, *Deep inelastic e p scattering in perturbation theory*, Sov.J.Nucl.Phys. **15** (1972) 438–450.

[122] V. N. Gribov and L. N. Lipatov, *e^+e^- pair annihilation and deep inelastic e p scattering in perturbation theory*, Sov.J.Nucl.Phys. **15** (1972) 675–684.

[123] D. J. Gross and F. Wilczek, *Asymptotically Free Gauge Theories. 1*, Phys.Rev. **D8** (1973) 3633–3652.

[124] D. J. Gross and F. Wilczek, *Ultraviolet Behavior of Non-Abelian Gauge Theories*, Phys.Rev.Lett. **30** (1973) 1343–1346.

[125] J. F. Gunion and H. E. Haber, *Higgs Bosons in Supersymmetric Models. 1.*, Nucl.Phys. **B272** (1986) 1–76.

[126] J. F. Gunion, M. Herrero, and A. Mendez, *Role of longitudinally polarized W's in slepton production and decay*, Phys.Rev. **D37** (1988) 2533–2536.

[127] J. F. Gunion and S. Mrenna, *Study of SUSY signatures at the Fermilab Tevatron in models with near mass degeneracy of the lightest chargino and neutralino*, Phys.Rev. **D62** (2000) 015002, [hep-ph/9906270].

[128] R. Haag, J. T. Łopuszański, and M. Sohnius, *All Possible Generators of Supersymmetries of the S-Matrix*, Nucl.Phys. **B88** (1975) 257–274.

[129] H. E. Haber, *The Status of the Minimal Supersymmetric Standard Model and Beyond*, Nucl.Phys.Proc.Suppl. **62** (1998) 469–484, [hep-ph/9709450].

[130] H. E. Haber and G. L. Kane, *The Search for Supersymmetry: Probing Physics Beyond the Standard Model*, Phys.Rept. **117** (1985) 75–263.

[131] T. Hahn, *Generating Feynman diagrams and amplitudes with FeynArts 3*, Comput.Phys.Commun. **140** (2001) 418–431, [hep-ph/0012260].

[132] T. Hahn, *A Mathematica interface for FormCalc-generated code*, Comput.Phys.Commun. **178** (2008) 217–221, [hep-ph/0611273].

[133] T. Hahn, *SUSY Les Houches Accord 2 I/O made easy*, Comput.Phys.Commun. **180** (2009) 1681–1693, [hep-ph/0605049].

[134] T. Hahn and M. Pérez-Victoria, *Automated one-loop calculations in four and D dimensions*, Comput.Phys.Commun. **118** (1999) 153–165, [hep-ph/9807565].

[135] T. Hahn and C. Schappacher, *The implementation of the Minimal Supersymmetric Standard Model in FeynArts and FormCalc*, Comput.Phys.Commun. **143** (2002) 54–68, [hep-ph/0105349].

[136] C. Han *et al.*, *Probing light higgsinos in natural SUSY from monojet signals at the LHC*, JHEP **1402** (2014) 049, [arXiv:1310.4274].

[137] D. Hanneke, S. Fogwell, and G. Gabrielse, *New Measurement of the Electron Magnetic Moment and the Fine Structure Constant*, Phys.Rev.Lett. **100** (2008) 120801, [arXiv:0801.1134].

[138] ALEPH Collaboration, A. Heister *et al.*, *Search for scalar leptons in e^+e^- collisions at centre-of-mass energies up to 209 GeV*, Phys.Lett. **B526** (2002) 206–220, [hep-ex/0112011].

[139] P. W. Higgs, *Broken Symmetries and the Masses of Gauge Bosons*, Phys.Rev.Lett. **13** (1964) 508–509.

[140] P. W. Higgs, *Broken Symmetries, Massless Particles and Gauge Fields*, Phys.Lett. **12** (1964) 132–133.

[141] P. W. Higgs, *Spontaneous Symmetry Breakdown without Massless Bosons*, Phys.Rev. **145** (1966) 1156–1163.

[142] K. Inoue *et al.*, *Aspects of Grand Unified Models with Softly Broken Supersymmetry*, Prog.Theor.Phys. **68** (1982) 927–946.

[143] K. Inoue *et al.*, *Renormalization of Supersymmetry Breaking Parameters Revisited*, Prog.Theor.Phys. **71** (1984) 413–416.

[144] B. Jäger, private communication.

[145] B. Jäger, A. Karlberg, and G. Zanderighi, *Electroweak $ZZjj$ production in the Standard Model and beyond in the POWHEG-BOX V2*, JHEP **1403** (2014) 141, [arXiv:1312.3252].

[146] B. Jäger, S. Schneider, and G. Zanderighi, *Next-to-leading order QCD corrections to electroweak Zjj production in the POWHEG BOX*, JHEP **1209** (2012) 083, [arXiv:1207.2626].

[147] B. Jäger, A. von Manteuffel, and S. Thier, *Slepton pair production in the POWHEG BOX*, JHEP **1210** (2012) 130, [arXiv:1208.2953].

[148] B. Jäger, A. von Manteuffel, and S. Thier, *Slepton pair production in association with a jet: NLO-QCD corrections and parton-shower effects*, (2014), [arXiv:1410.3802].

[149] B. Jäger and G. Zanderighi, *NLO corrections to electroweak and QCD production of W^+W^+ plus two jets in the POWHEG BOX*, JHEP **1111** (2011) 055, [arXiv:1108.0864].

[150] B. Jäger and G. Zanderighi, *Electroweak W^+W^-jj prodution at NLO in QCD matched with parton shower in the POWHEG-BOX*, JHEP **1304** (2013) 024, [arXiv:1301.1695].

[151] G. L. Kane *et al.*, *Study of constrained minimal supersymmetry*, Phys.Rev. **D49** (1994) 6173–6210, [hep-ph/9312272].

[152] A. Kardos, P. Nason, and C. Oleari, *Three-jet production in POWHEG*, JHEP **1404** (2014) 043, [arXiv:1402.4001].

[153] S. Kawabata, *A new version of the multi-dimensional integration and event generation package BASES/SPRING*, Comput.Phys.Commun. **88** (1995) 309–326.

[154] CMS Collaboration, V. Khachatryan *et al.*, *Searches for electroweak production of charginos, neutralinos, and sleptons decaying to leptons and W, Z, and Higgs bosons in pp collisions at 8 TeV*, (2014), [arXiv:1405.7570].

[155] W. B. Kilgore, *Regularization schemes and higher order corrections*, Phys.Rev. **D83** (2011) 114005, [arXiv:1102.5353].

[156] T. Kinoshita, *Mass Singularities of Feynman Amplitudes*, J.Math.Phys. **3** (1962) 650–677.

[157] M. Kobayashi and T. Maskawa, *CP-Violation in the Renormalizable Theory of Weak Interaction*, Prog.Theor.Phys. **49** (1973) 652–657.

[158] J. G. Körner, D. Kreimer, and K. Schilcher, *A Practicable γ_5-scheme in dimensional regularization*, Z.Phys. **C54** (1992) 503–512.

[159] A. Kraft, *Produktion geladener Higgs-Bosonen in Erweiterungen des Standardmodells*, Dissertation, Karlsruhe, 1999.

[160] D. Kreimer, *The γ_5-Problem and Anomalies - A Clifford Algebra Approach*, Phys.Lett. **B237** (1990) 59–62.

[161] D. Kreimer, *Dimensionale Regularisierung im Standard Modell*, Dissertation, Mainz, 1992.

[162] A. S. Kronfeld, *Twenty-First Century Lattice Gauge Theory: Results from the Quantum Chromodynamics Lagrangian*, Annu.Rev.Nucl.Part.Sci. **62** (2012) 265–284, [arXiv:1203.1204].

[163] P. Langacker and M. Luo, *Implications of precision electroweak experiments for m_t, ρ_0, $\sin^2\theta_W$ and grand unification*, Phys.Rev. **D44** (1991) 817–822.

[164] S. A. Larin, *The renormalization of the axial anomaly in dimensional regularization*, Phys.Lett. **B303** (1993) 113–118, [hep-ph/9302240].

[165] T. D. Lee and M. Nauenberg, *Degenerate Systems and Mass Singularities*, Phys.Rev. **133** (1964) B1549–B1562.

[166] C. G. Lester and D. J. Summers, *Measuring masses of semi-invisibly decaying particle pairs produced at hadron colliders*, Phys.Lett. **B463** (1999) 99–103, [hep-ph/9906349].

[167] L. N. Lipatov, *The parton model and perturbation theory*, Sov.J.Nucl.Phys. **20** (1975) 94–102.

[168] R. Mahbubani *et al.*, *Light Nondegenerate Squarks at the LHC*, Phys.Rev.Lett. **110** (2013) 151804, [arXiv:1212.3328].

[169] S. Mandelstam, *Light-Cone Superspace and the Ultraviolet Finiteness of the $N = 4$ Model*, Nucl.Phys. **B213** (1983) 149–168.

[170] G. Marchesini *et al.*, *HERWIG 5.1 - a Monte Carlo event generator for simulating hadron emission reactions with interfering gluons*, Comput.Phys.Commun. **67** (1992) 465–508.

[171] A. D. Martin *et al.*, *Parton distributions for the LHC*, Eur.Phys.J. **C63** (2009) 189–285, [arXiv:0901.0002].

[172] S. P. Martin, *A Supersymmetry Primer*, Adv.Ser.Direct.High En.Phys. **21** (2010) 1–153, [hep-ph/9709356].

[173] S. P. Martin and M. T. Vaughn, *Regularization dependence of running couplings in softly broken supersymmetry*, Phys.Lett. **B318** (1993) 331–337, [hep-ph/9308222].

[174] K. T. Matchev and M. Park, *General Method for Determining the Masses of Semi-Invisibly Decaying Particles at Hadron Colliders*, Phys.Rev.Lett. **107** (2011) 061801, [arXiv:0910.1584].

[175] T. Melia *et al.*, *W^+W^-, WZ and ZZ production in the POWHEG BOX*, JHEP **1111** (2011) 078, [arXiv:1107.5051].

[176] T. Melia *et al.*, *W^+W^+ plus dijet production in the POWHEG BOX*, Eur.Phys.J. **C71** (2011) 1670, [arXiv:1102.4846].

[177] G. Miu and T. Sjöstrand, *W production in an improved parton-shower approach*, Phys.Lett. **B449** (1999) 313–320, [hep-ph/9812455].

[178] S. Moch, J. A. M. Vermaseren, and A. Vogt, *The three-loop splitting functions in QCD: the non-singlet case*, Nucl.Phys. **B688** (2004) 101–134, [hep-ph/0403192].

[179] H. J. W. Müller-Kirsten and A. Wiedemann, *Introduction to Supersymmetry*, World Scientific, (2010).

[180] P. Nason, *A new method for combining NLO QCD with shower Monte Carlo algorithms*, JHEP **0411** (2004) 040, [hep-ph/0409146].

[181] P. Nason, *MINT: a Computer Program for Adaptive Monte Carlo Integration and Generation of Unweighted Distributions*, (2007), [arXiv:0709.2085].

[182] P. Nason and C. Oleari, *NLO Higgs boson production via vector-boson fusion matched with shower in POWHEG*, JHEP **1002** (2010) 037, [arXiv:0911.5299].

[183] P. Nason and B. Webber, *Next-to-Leading-Order Event Generators*, Annu.Rev.Nucl.Part.Sci. **62** (2012) 187–213, [arXiv:1202.1251].

[184] P. Nason and G. Zanderighi, *W^+W^-, WZ and ZZ production in the POWHEG-BOX-V2*, Eur.Phys.J. **C74** (2014) 2702, [arXiv:1311.1365].

[185] H. P. Nilles, *Supersymmetry, Supergravity and Particle Physics*, Phys.Rept. **110** (1984) 1–162.

[186] E. Norrbin and T. Sjöstrand, *QCD radiation off heavy particles*, Nucl.Phys. **B603** (2001) 297–342, [hep-ph/0010012].

[187] H. Pagels and J. R. Primack, *Supersymmetry, Cosmology, and New Physics at Teraelectronvolt Energies*, Phys.Rev.Lett. **48** (1982) 223–226.

[188] F. E. Paige *et al.*, *ISAJET 7.69: A Monte Carlo Event Generator for pp, $\bar{p}p$, and e^+e^- Reactions*, (2003), [hep-ph/0312045].

[189] P. Pascual and R. Tarrach, *QCD: Renormalization for the Practitioner*, Springer, (1984).

[190] G. Passarino and M. J. G. Veltman, *One-Loop Corrections for e^+e^- Annihilation Into $\mu^+\mu^-$ in the Weinberg Model*, Nucl.Phys. **B160** (1979) 151–207.

[191] M. E. Peskin, *Compositeness of Quarks and Leptons*, eConf **C810824** (1981) 880–907.

[192] M. E. Peskin and D. V. Schroeder, *An Introduction to Quantum Field Theory*, Westview Press, (1995).

[193] H. D. Politzer, *Reliable Perturbative Results for Strong Interactions?*, Phys.Rev.Lett. **30** (1973) 1346–1349.

[194] H. D. Politzer, *Asymptotic Freedom: An Approach to Strong Interactions*, Phys.Rept. **14** (1974) 129–180.

[195] E. Re, *NLO corrections merged with parton showers for Z +2 jets production using the POWHEG method*, JHEP **1210** (2012) 031, [arXiv:1204.5433].

[196] C. Rogan, *Kinematical variables towards new dynamics at the LHC*, (2010), [arXiv:1006.2727].

[197] D. A. Ross and J. C. Taylor, *Renormalization of a Unified Theory of Weak and Electromagnetic Interactions*, Nucl.Phys. **B51** (1973) 125–144.

[198] A. Salam, *Weak and Electromagnetic Interactions*, Conf.Proc. **C680519** (1968) 367–377.

[199] A. Salam and J. C. Ward, *Electromagnetic and Weak Interactions*, Phys.Lett. **13** (1964) 168–171.

[200] G. P. Salam, *Elements of QCD for hadron colliders*, CERN Yellow Report **CERN-2010-002** (2010) 45–100, [arXiv:1011.5131].

[201] G. P. Salam, *Towards jetography*, Eur.Phys.J. **C67** (2010) 637–686, [arXiv:0906.1833].

[202] F. Schissler and D. Zeppenfeld, *Parton shower effects on W and Z production via vector boson fusion at NLO QCD*, JHEP **1304** (2013) 057, [arXiv:1302.2884].

[203] P. Schwaller and J. Zurita, *Compressed electroweakino spectra at the LHC*, JHEP **1403** (2014) 060, [arXiv:1312.7350].

[204] T. Sjöstrand, *A Model for Initial State Parton Showers*, Phys.Lett. **B157** (1985) 321–325.

[205] T. Sjöstrand, S. Mrenna, and P. Z. Skands, *PYTHIA 6.4 physics and manual*, JHEP **0605** (2006) 026, [hep-ph/0603175].

[206] T. Sjöstrand, S. Mrenna, and P. Z. Skands, *A brief introduction to PYTHIA 8.1*, Comput.Phys.Commun. **178** (2008) 852–867, [arXiv:0710.3820].

[207] T. Sjöstrand and P. Z. Skands, *Transverse-momentum-ordered showers and interleaved multiple interactions*, Eur.Phys.J. **C39** (2005) 129–154, [hep-ph/0408302].

[208] P. Z. Skands, *QCD for Collider Physics*, MCnet publications **MCNET-11-13** (2011) 1–48, [arXiv:1104.2863].

[209] P. Z. Skands *et al.*, *SUSY Les Houches accord: interfacing SUSY spectrum calculators, decay packages, and event generators*, JHEP **0407** (2004) 036, [hep-ph/0311123].

[210] T. Stelzer and W. F. Long, *Automatic generation of tree level helicity amplitudes*, Comput.Phys.Commun. **81** (1994) 357–371, [hep-ph/9401258].

[211] C. Studerus, *Reduze - Feynman integral reduction in C++*, Comput.Phys.Commun. **181** (2010) 1293–1300, [arXiv:0912.2546].

[212] V. V. Sudakov, *Vertex parts at very high energies in quantum electrodynamics*, Sov.Phys.JETP **3** (1956) 65–71.

[213] L. Susskind, *Dynamics of spontaneous symmetry breaking in the Weinberg-Salam theory*, Phys.Rev. **D20** (1979) 2619–2625.

[214] G. 't Hooft, *Symmetry Breaking through Bell-Jackiw Anomalies*, Phys.Rev.Lett. **37** (1976) 8–11.

[215] G. 't Hooft and M. J. G. Veltman, *Regularization and Renormalization of Gauge Fields*, Nucl.Phys. **B44** (1972) 189–213.

[216] G. J. van Oldenborgh, *FF - a package to evaluate one-loop Feynman diagrams*, Comput.Phys.Commun. **66** (1991) 1–15.

[217] J. A. M. Vermaseren, *New features of FORM*, (2000), [math-ph/0010025].

[218] A. Vogt, S. Moch, and J. A. M. Vermaseren, *The three-loop splitting functions in QCD: the singlet case*, Nucl.Phys. **B691** (2004) 129–181, [hep-ph/0404111].

[219] D. V. Volkov and V. P. Akulov, *Possible Universal Neutrino Interaction*, JETP Lett. **16** (1972) 438–440.

[220] A. von Manteuffel, private communication.

[221] A. von Manteuffel and C. Studerus, *Reduze 2 - Distributed Feynman Integral Reduction*, (2012), [arXiv:1201.4330].

[222] S. Weinberg, *A Model of Leptons*, Phys.Rev.Lett. **19** (1967) 1264–1266.

[223] S. Weinberg, *Implications of dynamical symmetry breaking: An addendum*, Phys.Rev. **D19** (1979) 1277–1280.

[224] J. Wess and B. Zumino, *Supergauge Transformations in Four Dimensions*, Nucl.Phys. **B70** (1974) 39–50.

[225] M. R. Whalley, D. Bourilkov, and R. C. Group, *The Les Houches Accord PDFs (LHAPDF) and LHAGLUE*, (2005), [hep-ph/0508110].

[226] G. C. Wick, *Properties of Bethe-Salpeter Wave Functions*, Phys.Rev. **96** (1954) 1124–1134.

[227] K. G. Wilson, *Quantum Field-Theory Models in Less Than 4 Dimensions*, Phys.Rev. **D7** (1973) 2911–2926.

[228] M. Wobisch and T. Wengler, *Hadronization Corrections to Jet Cross Sections in Deep-Inelastic Scattering*, (1998), [hep-ph/9907280].

[229] Wolfram Research, *Mathematica, Version 8.0*, 2010.